EnergyChem 8 (2026) 100201

Contents lists available at ScienceDirect

EnergyChem

journal homepage: www.sciencedirect.com/journal/energychem

Phase-tunable exsolution approaches to energy-functional nanostructured metal-based hybrid materials: synthesis, application, and perspective

Taehoon Kim [a,1], Yeon Hu Park [a,1], Jinyoung Lee [b], Ajayan Vinu [c,*], Seong-Ju Hwang [a,d,*]

[a] Department of Materials Science and Engineering, College of Engineering, Yonsei University, Seoul 03722, Republic of Korea
[b] Department of Battery Conflation Engineering, Yonsei University, Seoul 03722, Republic of Korea
[c] Global Innovative Center for Advanced Nanomaterials (GICAN), School of Engineering, College of Engineering, Science and Environment, The University of Newcastle, Callaghan NSW 2308 Australia
[d] Department of Battery Engineering, Yonsei University, Seoul, 03722 Republic of Korea

ARTICLE INFO

Keywords:
Phase-tuning
Exsolution
Energy Functionality
Nanocatalysts
Nanohybrids

ABSTRACT

Low-dimensional metal nanostructures have sparked tremendous research activity owing to their valuable applications for energy conversion and storage technologies. The energy-related functionalities and stabilities of metal nanostructures are strongly dependent on their surface properties, chemical bonding nature, and electronic and geometric characteristics. Consequently, the regulation of these features can play a pivotal role in enhancing the electrochemical and catalytic performances of metal nanostructures. As an emerging approach for developing highly efficient and robust metal nanostructured materials, exsolution has garnered increasing attention because it enables effective control and stabilization of metal nanoparticles within solid matrices. Moreover, tuning the exsolution conditions can induce phase transitions in the solid substrates, allowing for the expansion of application area from conventional solid oxide fuel cells to other energy-related fields, such as catalysis and batteries. This review highlights the unique merits of phase-tunable exsolution for exploring high-performance energy-functional materials, with an in-depth discussion of the key design factors that optimize their energy performance. A comprehensive survey of a wide range of exsolved hybrid materials was conducted depending on the synthesis methods, characterization tools, and application fields. Future research perspectives for designing and synthesizing high-performance exsolution materials are provided to offer inspiring insights for improving their functionalities, which is pivotal for diverse energy technologies.

1. Introduction

Metal nanostructures, including nanoparticles, nanoclusters, and single atoms, have garnered significant interest owing to their versatile functionalities for energy conversion, energy storage, and photonics [1–6]. Because the dimension of metal nanostructures has a profound impact on their many functionalities, robust anchoring of metal nanostructures on a solid substrate has been widely applied to prevent the enlargement of particle size during repeated operation. As an emerging approach for stabilizing metal nanostructures on an inorganic matrix, exsolution has evoked intense research activity because of its high efficacy in enhancing the stability of these nanomaterials [7,8]. This exsolution implies the migration of highly reducible metal ions from their original lattice positions to the surface of the solid substrate, that is, an opposite process to the formation of a solid solution. Typically, the exsolution process can be achieved by the heat treatment of multimetallic oxides under a reductive atmosphere, resulting in the migration of reducible metal component ions onto the surface of the material and simultaneous reduction into zero-valent metal and/or lower-valent metal species [9]. While some parts of the exsolved metal nanoparticles were surface-exposed, the opposite part was strongly embedded inside the solid substrate, leading to an unusually robust immobilization of metal nanostructures [10,11]. Owing to such unique geometric configurations, the exsolved metal species have an unusually strong adhesion to solid substrates, which prevents particle agglomeration and significantly enhances their structural and electrochemical stability [12,13]. Additionally, the chemical bonding of the exsolved metal species with a solid matrix induces efficient interfacial electronic

* Corresponding authors.
E-mail addresses: Ajayan.Vinu@newcastle.edu.au (A. Vinu), hwangsju@yonsei.ac.kr (S.-J. Hwang).
[1] These authors contributed equally to this work.

https://doi.org/10.1016/j.enchem.2026.100201

Available online 22 May 2026
2589-7780/© 2026 Elsevier Ltd. All rights are reserved, including those for text and data mining, AI training, and similar technologies.

coupling and thus maximizes the metal−substrate interaction [14–16]. Because metal nanostructures have versatile functionalities in various application fields, exsolved metal−substrate hybrid materials can be widely used as electrocatalysts, photocatalysts, electrodes for secondary batteries, fuel cells, electrolyzers, and sensors [17–22]. Various synthesis methods for the exsolution of metal nanostructures have been developed, such as thermal reduction, electrochemical reduction, hydrothermal reduction, and plasma treatment [23–25]. The fine control of exsolution conditions allows control of the crystal phase and chemical composition of solid matrices [26,27], which seriously affect the properties and functionalities of the exsolved metal species. In electrochemistry-related applications, the immobilization of exsolved metal species onto conductive inorganic substrates is presumed to be useful for boosting these functionalities by enhancing charge transport kinetics [28,29]. Tailoring the electronic conduction of the exsolution matrix is pivotal for further improving the energy-related performance of exsolved nanohybrids [30,31]. However, as most metal oxide substrates employed for the exsolution reaction exhibit relatively low electrical conductivity, it is necessary to improve the charge-transport properties of the exsolution matrix. For this purpose, the phase transition from metal oxides to metal pnictogenides or chalcogenides can offer valuable opportunities to improve the electrochemical performance of exsolved metal species because metal−pnictogen/chalcogen bonds show a higher covalency than metal−oxygen bonds, which reduces the bandgap energy [32].

As simulated in Scheme 1, the concept of metal nanoparticle exsolution from perovskite oxides originated from the "self-regeneration" phenomenon discovered by Nishihata et al. in 2002, where Pd ions reversibly migrated in and out of the $LaFe_{0.57}Co_{0.38}Pd_{0.05}O_3$ lattice depending on the oxidizing/reducing atmosphere [33]. Following this discovery, Madsen et al. (2007) demonstrated that Ru nanoclusters can be nucleated in situ on solid oxide fuel cell (SOFC) anodes, establishing a foundation for practical applications [34]. Neagu and Irvine (2010) further revealed that A-site deficiency promotes oxygen removal, providing the defect-chemical basis for exsolution [35], and formally introduced the “exsolution” concept in 2013 by demonstrating that A-site non-stoichiometry in $La_{0.4}Sr_{0.4}Ni_{0.03}Ti_{0.97}O_{3-\gamma}$ enables controlled Ni nanoparticle growth [36]. Subsequent studies discovered the "socketed" nanoparticle structure providing strong metal−oxide anchoring (2015) [37], and electrochemical switching enabling voltage-triggered fast exsolution (2016) [38], and extended the concept to layered perovskite with density functional theory (DFT)-guided design of co-segregation energy (2017) [39].

Building on these mechanistic insights, recent innovations have expanded beyond the traditional thermal reduction. Plasma-driven exsolution achieved >10x higher particle density at 650 °C (2021) [40], while room-temperature direct plasma exsolution (2022) demonstrated that charged species alone can trigger nucleation without thermal activation [41]. Simultaneously, phase-transition exsolution strategies have emerged, including carbon-coating exsolution (2022), creating Ru−MnO@C nanowires with enhanced interfacial bonding [42], nitridation-induced exsolution to form Ru−TiN nanotubes (2024) [43], and phosphidation-driven exsolution of Ru single atoms on Ni_2P/Fe_3P heterostructures (2024) [44]. As discussed above, exsolved metal nanostructures in phase-tuned substrates can serve as efficient catalysts, electrodes, and sensors [45–53]. Thus, the development of phase-tunable exsolution methods opens new avenues for developing highly efficient functional materials. However, at the time of this submission, we were not aware of any prior review focusing on phase-controllable exsolution approaches for diverse metal nanospecies and their impact on the performance of the resulting nanohybrids.

In this review, we provide a comprehensive survey of phase-tunable exsolution strategies for nanostructured metal−substrate nanohybrids, including their synthesis methods, characterization tools, and various applications. Additionally, we present an in-depth discussion of the advantages of the exsolution approach in developing highly efficient functional hybrid materials, with the establishment of key design factors affecting their performance. This review offers insights into the rational design and synthesis of exsolved metal-based functional materials.

2. Fundamentals and synthesis methods for exsolution-based energy functional materials

2.1. Exsolution mechanism

Exsolution is a powerful strategy for synthesizing nanosized metal catalysts anchored on a host matrix. In general, specific guest metal ions substituted into the host oxide lattice are reduced under reductive conditions, forming metal nanoparticles on the surface of the supporting matrix. The reduction process of guest metal cation is shown in Eq. (1) and (2), where O_O^X and V''_O represent oxygen ion and oxygen vacancy in the host oxide lattice, respectively, and M_M^{n+} and M^0 represent guest

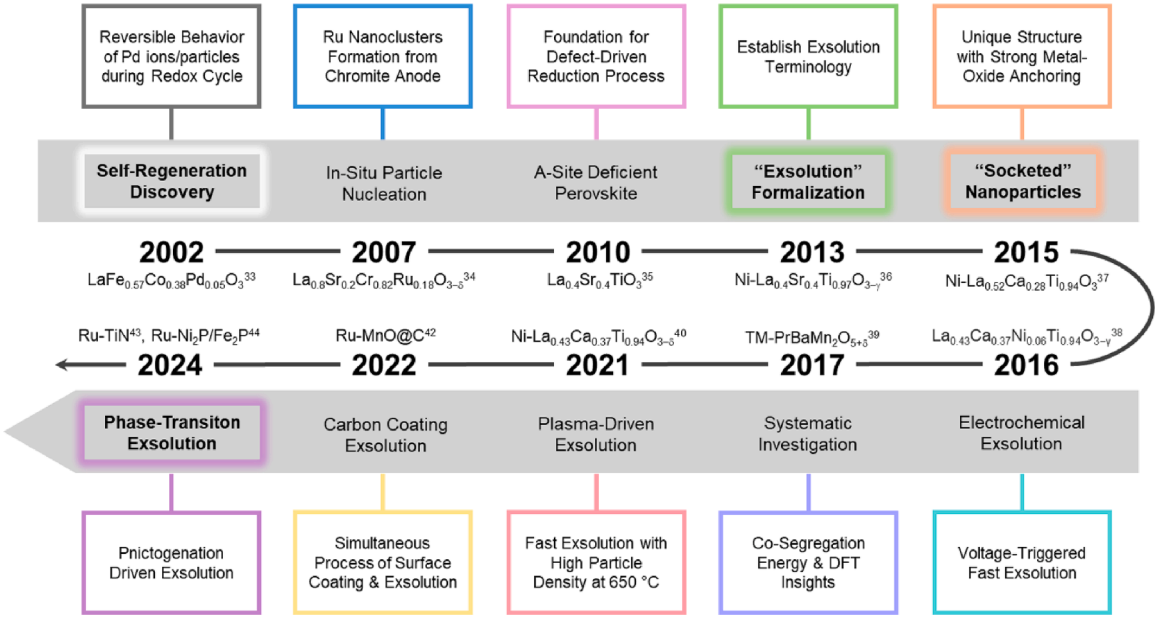

Scheme 1. Timeline of the development of exsolution-based materials for energy-related applications.

metal cation and exsolved zero-valent metal, respectively [54,55].

$$O_O^X \rightarrow V''_O + 2e^- + 1/2O_2 \quad (1)$$

$$M^{n+}{}_M + ne^- \rightarrow M^0 \quad (2)$$

In the early stages of exsolution, surface oxygen ions near exsolvable guest metal cations are removed under a reducing atmosphere, releasing gaseous oxygen (or H_2O/CO_2) and leaving oxygen vacancies and electrons [54,55]. These electrons are directly consumed by nearby metal cations, leading to a partial or complete reduction to the zero-valent metallic state. The reduced metal atoms (M^0) lose their affinity for oxygen coordination and prefer metallic bonding, forming small metallic nuclei at or near the surface [56]. These nuclei serve as seeds for the subsequent growth of nanoparticles. Following this initial reduction and nucleation stage, the formation of oxygen vacancies at the surface establishes a strong concentration gradient between the surface and the bulk [55]. To restore the stoichiometric balance, lattice oxygen ions (O^{2-}) diffuse toward the surface, whereas oxygen vacancies move inward. This vacancy-mediated mass exchange allows the reduction front to propagate gradually into the bulk, continuously supplying reducible species and sustaining the overall exsolution process. As diffusion progresses, reduced metal species migrate toward the surface through the vacancy network, aggregate around the pre-existing nuclei, and grow into larger nanoparticles that gradually protrude from the surface while remaining partially embedded in the oxide matrix [56]. This embedded geometry is thermodynamically favorable because it minimizes the interfacial energy and strain [57–59]. The detailed reaction sequence of the exsolution, including surface reduction, nucleation, ion diffusion, and particle growth, is illustrated in Fig. 1.

In addition to the general reduction and diffusion sequences illustrated in Fig. 1, the microscopic kinetics of exsolution are also affected by the crystallographic orientation and defect chemistry of the host lattice [60]. The surface energy and local coordination environment of different crystal planes (e.g., (100) and (110)) influence the formation energy of oxygen vacancies and thus the preferred nucleation sites, with high-energy facets facilitating oxygen release and cation migration [61,62]. Similarly, the reducibility of the host lattice strongly depends on the ionic radius and oxidation state of the guest cations: larger or lower-valent dopants weaken the metal–oxygen bonds and promote early stage vacancy formation, whereas smaller or higher-valent cations stabilize the lattice and delay the reduction process [63–65]. These defect-driven and orientation-dependent effects modulate the nucleation rate and particle distribution without altering the fundamental thermodynamic nature of exsolution. Consequently, while the overall driving force of the process is governed by the Gibbs free energy terms discussed below, the kinetics and spatial selectivity of the particle formation are dictated by the crystallographic and chemical environments of the host matrix.

From a thermodynamic perspective, these sequential processes are driven by the overall Gibbs free energy changes in the system. Thermodynamically, the driving force of the exsolution process can be expressed as the change in the total Gibbs free energy, see Eq. (3).

$$\Delta G_{exsolution} = \Delta G_{reduction} + \Delta G_{diffusion} + \Delta G_{surface} + \Delta G_{strain} \quad (3)$$

Each energetic contribution corresponds to a distinct physical process involved in the exsolution, and their combined effects determine the overall tendency and pathways of the exsolution reaction. $\Delta G_{reduction}$ represents the change in the chemical free energy associated with the reduction of metal cations to metallic species [66]. The $\Delta G_{diffusion}$ reflects the mass transport of oxygen and guest metal ions under a chemical potential gradient [67]. $\Delta G_{surface}$ describes the energetic cost of forming new metal–oxide interfaces during nucleation and growth [68], whereas ΔG_{strain} describes the elastic energy change resulting from lattice distortion and subsequent relaxation upon particle formation [66]. Among these components, $\Delta G_{reduction}$ is the primary driving force because it directly determines the thermodynamic feasibility of exsolution. When the $\Delta G_{reduction}$ becomes negative under reductive conditions, the guest metal cations are energetically driven to accept electrons

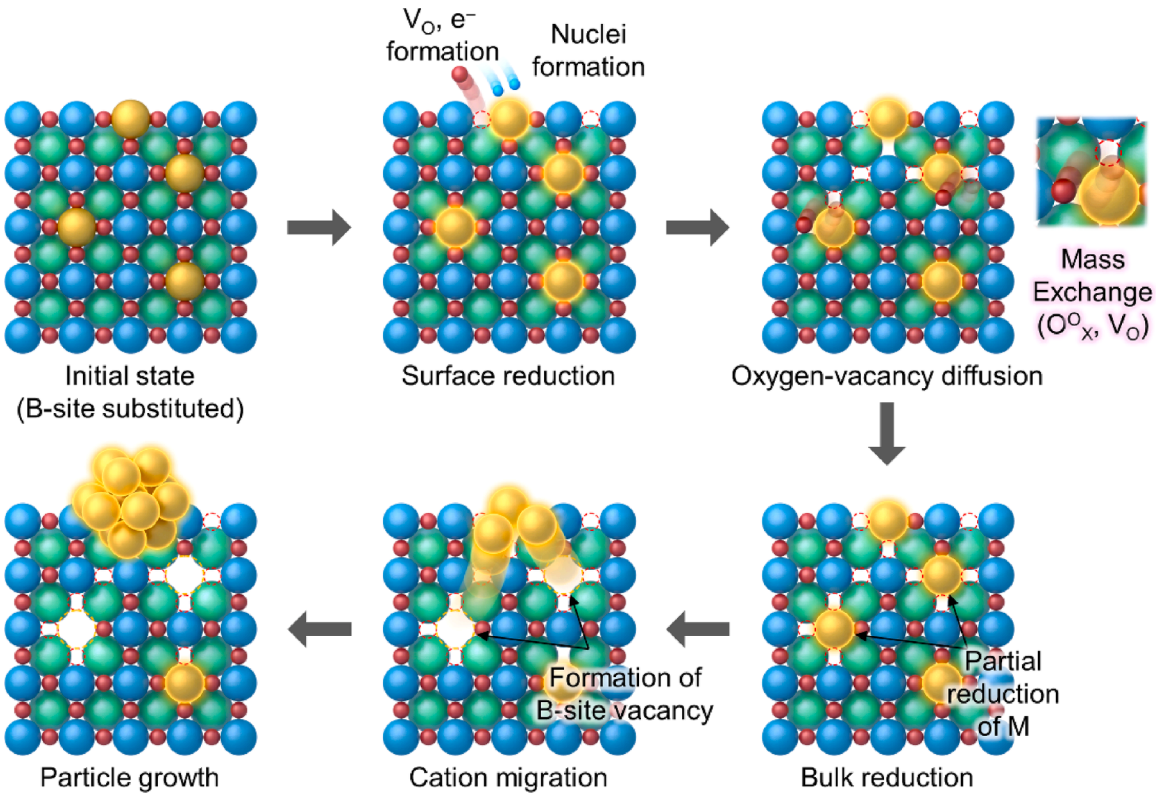

Fig. 1. Schematic illustration of the exsolution process and the underlying mechanisms.

and transform into metallic species [66]. This reduction reaction simultaneously generates oxygen vacancies at the surface, thereby providing chemical potential gradients of oxygen and metal ions that define the $\Delta G_{diffusion}$ [68]. Therefore, the $\Delta G_{reduction}$ acts as the fundamental energetic origin that governs both the initiation and subsequent evolution of the total exsolution process, from diffusional transport to interfacial formation and strain relaxation. Once reduction-driven nucleation is initiated, the subsequent evolution is governed mainly by diffusion processes, as the chemical potential gradients established by vacancy formation promote the outward migration of guest cations and the inward diffusion of vacancies [67]. As metallic particles grow and become partially embedded, $\Delta G_{surface}$ and ΔG_{strain} progressively decrease because coherent metal−oxide interfaces form and lattice strain is progressively relaxed [69]. Consequently, the overall system evolves toward a steady-state configuration, in which the interfacial and elastic energies are minimized. These self-regulating thermodynamic and kinetic processes not only stabilize the exsolved structure but also provide numerous advantages such as enhanced durability and strong metal−support coupling. In many oxide hosts, these self-regulating processes allow exsolution to proceed in a largely topotactic manner, preserving the long-range crystal symmetry while accommodating local distortions and vacancy formation [70,71]. This lattice integrity provides a structural basis for the reversible formation and stabilization of the anchored nanoparticles, ensuring reliable performance under electrochemical operating conditions [72]. Overall, these thermodynamic and kinetic mechanisms collectively govern the structural stability and catalytic performance of the exsolved systems. They not only determine the nucleation behavior and interfacial evolution of metallic nanoparticles but also ensure robust metal−support coupling, reversible lattice integrity, and long-term durability under redox and thermal cycling conditions, as further discussed in the following section.

2.2. Advantages of exsolution methods

Exsolution is a powerful route for constructing highly stable and active metal−oxide hybrid catalysts. During the reduction process, the guest metal cations incorporated within the host oxide lattice migrated to the surface and were partially reduced, forming metallic nanoparticles that remained partially embedded in the oxide matrix [8]. Unlike conventional impregnation or deposition methods in which metal particles are externally attached to the support, exsolution drives the in situ growth of metallic particles from the host bulk lattice, resulting in partially embedded nanoparticles. This unique growth mechanism originates from the topotactic reduction and lattice continuity of the host oxide, which prevents the detachment of the newly formed metallic species. For instance, in perovskite-type $La_{0.8}Sr_{0.2}Fe_{0.9}Ni_{0.1}O_{3-\delta}$ and related transition-metal-doped perovskites, exsolved Ni nanoparticles remain partially embedded within the perovskite lattice, forming coherent metal−oxide interfaces that ensure high structural and electrochemical stability during redox cycling [59,73,74]. Consequently, the exsolved nanoparticles were strongly anchored and maintained intimate atomic contact with the host oxide matrix, forming strongly coupled metal−oxide interfaces. This partially embedded structure suppressed particle migration and agglomeration, maintaining nanoscale dispersion even under harsh redox or thermal cycling conditions [60,75,76]. The intimate contact and electronic coupling between the exsolved metal and oxide matrix induce robust metal−support interactions, which facilitate efficient charge transport across the interface [77]. This interfacial coupling enhances the catalytic activity, electrical conductivity, and reaction kinetics of the composite systems.

In addition, the overall crystal structure of the host lattice is largely preserved during the exsolution process, providing excellent structural reversibility and mechanical stability [78,79]. The retention of the original phase minimizes the internal stress and defect accumulation, allowing the hybrid to sustain its functionality over prolonged operation. In addition to these structural and electronic advantages, the semi-embedded geometry of exsolved nanoparticles imparts remarkable redox reversibility. Because the exsolved metals remain coherently integrated with the parent lattice, they can undergo reversible redox transformations without detachment or sintering. Under alternating oxidizing and reducing atmospheres, the nanoparticles maintained their dispersion and crystallographic integrity, leading to enhanced structural endurance and consistent activity during long-term operation. This inherent redox adaptability provides additional stability that distinguishes exsolved catalysts from those prepared by conventional deposition methods. The anchored particle geometry, coherent metal−oxide interface, and structurally stable host lattice endow the exsolved materials with outstanding durability and reliable performance across a wide range of electrochemical and catalytic applications [72]. The typical morphologies and structural evolution of the exsolved nanoparticles are shown in Fig. 2, strongly underscoring the intrinsic advantages of exsolved materials, such as strong particle anchoring, high dispersion, and structural robustness under the operating conditions.

These characteristics define the baseline advantages of conventional oxide-based exsolution, where metal nanoparticles are exsolved from a structurally robust host while preserving strong metal−matrix coupling and long-term stability. On this foundation, exsolution strategies have been widely applied in various energy-related systems and, more recently, extended toward phase-tunable architectures, in which the host matrix itself is transformed to further tailor the metal−matrix interface, conductivity, and defect structure.

2.3. Synthetic methods

Exsolution can be triggered through various synthetic routes that differ in how they supply the fundamental driving forces for oxygen removal, defect formation, and metal ion reduction. These thermodynamic and kinetic processes are common to all exsolution systems. However, the manner in which each synthesis method delivers the necessary driving forces varies significantly. Consequently, the defect formation rate, depth of reduction, and final morphology of the exsolved nanoparticles differ depending on the chosen approach [80–82]. Electrochemical methods induce the formation of oxygen vacancies through anodic or cathodic polarization. This process allows exsolution to occur at relatively low temperatures because the applied potential directly extracts surface oxygen and reduces the guest metal ions [83]. By contrast, thermal annealing relies on gas−solid redox reactions that remove lattice oxygen throughout the bulk, allowing long range cation diffusion and the formation of well-anchored metallic nanoparticles under high temperature reducing atmospheres [84,85]. Plasma-assisted strategies promote the rapid and localized removal of surface oxygen through energetic ions, electrons, and reactive radicals, which enables the formation of ultrafine nanoparticles even under mild thermal conditions while largely preserving the bulk structure [86,87] In addition, several exsolution methods are available, including chemical etching, carbonate decomposition, surface modification, and photoinduced pathways [88–91].

2.3.1. Electrochemical exsolution

Electrochemical exsolution activates metal emergence through direct injection of electrons into the host lattice, as illustrated in Fig. 3a. In this approach, the applied potential reduces the number of metal cations incorporated into the oxide lattice and simultaneously generates surface oxygen vacancies that serve as diffusion pathways for metal cation migration [83]. In addition to supplying electrons, the external bias continuously withdraws lattice oxygen through electrochemical oxygen pumping, further strengthening the local reducing environment at the electrode−electrolyte interface [83]. Because the driving force of the reduction is directly controlled by the applied electrode potential, electrochemical activation enables exsolution to occur selectively in targeted regions and at temperatures lower than those required for

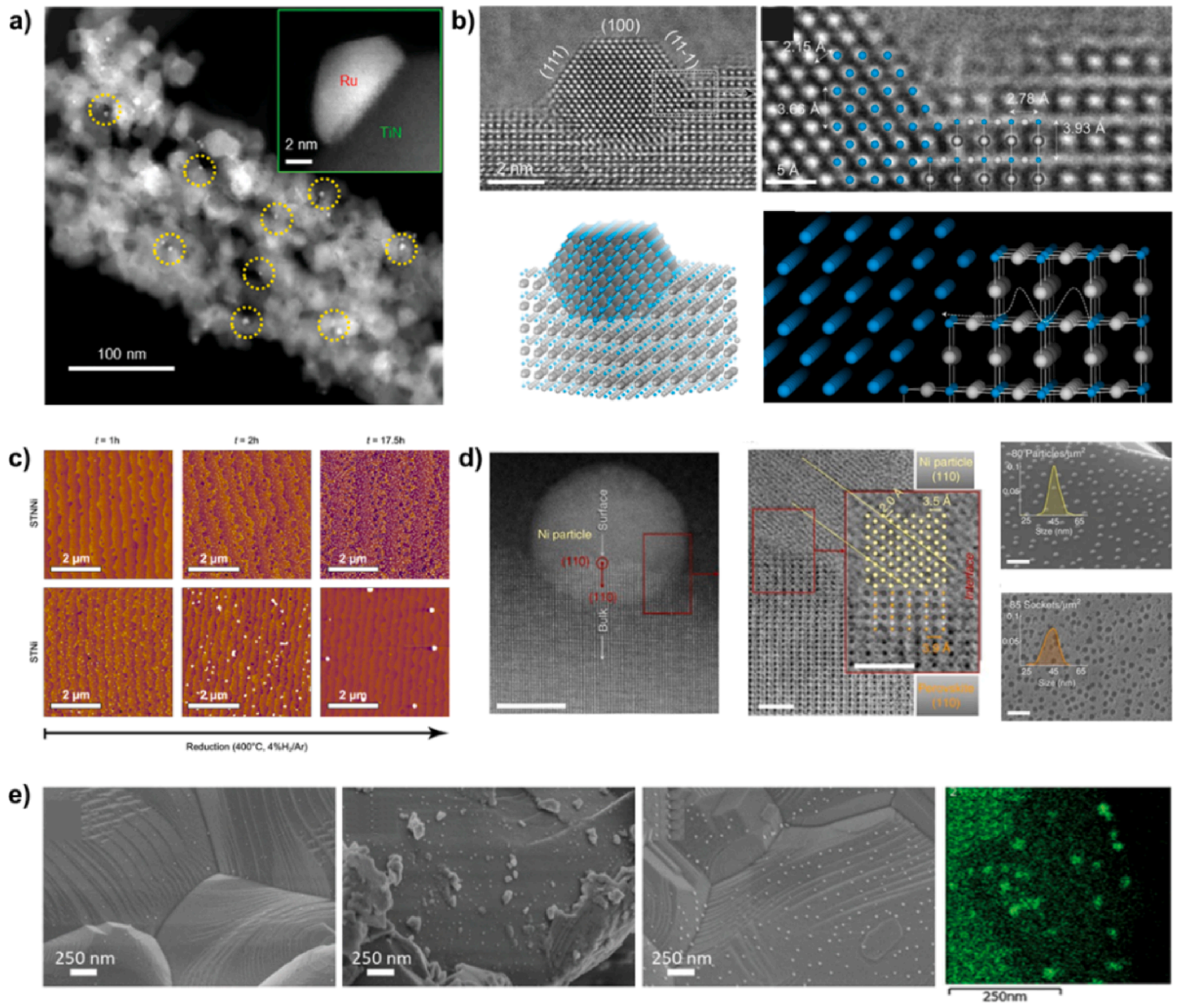

Fig. 2. Morphological images of various exsolved nanostructures: a) Scanning transmission electron microscopy (STEM) image of holey Ru−TiN nanotubes with uniformly distributed, partially embedded Ru nanoparticles (yellow circles) and a high-resolution inset of the coherent Ru/TiN interface, illustrating strongly socketed metal sites. Reproduced with permission [43]. Copyright 2024, Wiley-VCH. b) High-resolution TEM images of semi-spherical Ni nanoparticles grown at the $La_{0.43}Ca_{0.37}Ti_{0.94}Ni_{0.06}O_3$, along with structural models, revealing lattice continuity across the Ni−perovskite junction that underpins strong metal−support interaction. Reproduced with permission [99]. Copyright 2019, American Chemical Society. c) Atomic force microscopy (AFM) images of $SrTi_{0.9}Nb_{0.05}Ni_{0.05}O_{3-\delta}$ (STNNi) and $SrTi_{0.95}Ni_{0.05}O_{3-\delta}$ (STNi) after thermal exsolution for 1, 2, and 17.5 h, showing progressive particle nucleation and surface roughening for Nb-containing compositions compared with the Nb-free control. Reproduced with permission [98]. Copyright 2024, Springer Nature. d) TEM and SEM analyses of exsolved Ni nanoparticles, including particle and socket size distributions, demonstrating a narrow size dispersion and one-to-one particle−socket correlation characteristic of socketed exsolution. Reproduced with permission [37]. Copyright 2015, Springer Nature. e) Scanning electron microscopy (SEM) images and elemental mapping of Ni exsolved from Sr-doped $LaTiO_3$ at 700, 800, and 900 °C, indicating that higher exsolution temperatures increase the areal density of Ni nanoparticles while preserving their anchored configuration. Reproduced with permission [12]. Copyright 2023, Wiley-VCH.

conventional thermal conditions. Because the localized reducing environment is confined to the electrochemically active region, the nucleation density can change quickly, and the surface composition can be locally adjusted. Thus, electrochemical methods are particularly useful for tuning catalytic surfaces during operation.

Wang et al. reported an electrochemically driven exsolution process using Cu introduced γ-NiOOH layered hydroxides [92]. Under cathodic electrochemical activation in a CO_2-saturated electrolyte, the applied potential reduces the number of lattice Cu centers and creates oxygen-vacancy-rich environments that facilitate Cu migration toward the surface. Consequently, ultrasmall Cu nanoparticles (~4 nm) were exsolved in a semi-embedded configuration on the NiOOH layers. This electrochemical exsolution, achieved near ambient temperature without high-temperature annealing, produced highly dispersed Cu nanoparticles and markedly enhanced the CO_2 reduction performance, demonstrating that potential-driven exsolution can efficiently convert guest Cu ions into catalytically active and strongly anchored metal nanoparticles. The activation energy for this electrochemical exsolution was extremely low, enabling fast nucleation and demonstrating that electrochemistry-driven pathways can dramatically accelerate cation reduction compared to classical gas-phase annealing. Overall, this study illustrated how electrochemical exsolution can activate metal exsolution in materials without a thermal driving force, thereby enabling the formation of highly localized and energy-efficient catalysts. Kim et al.

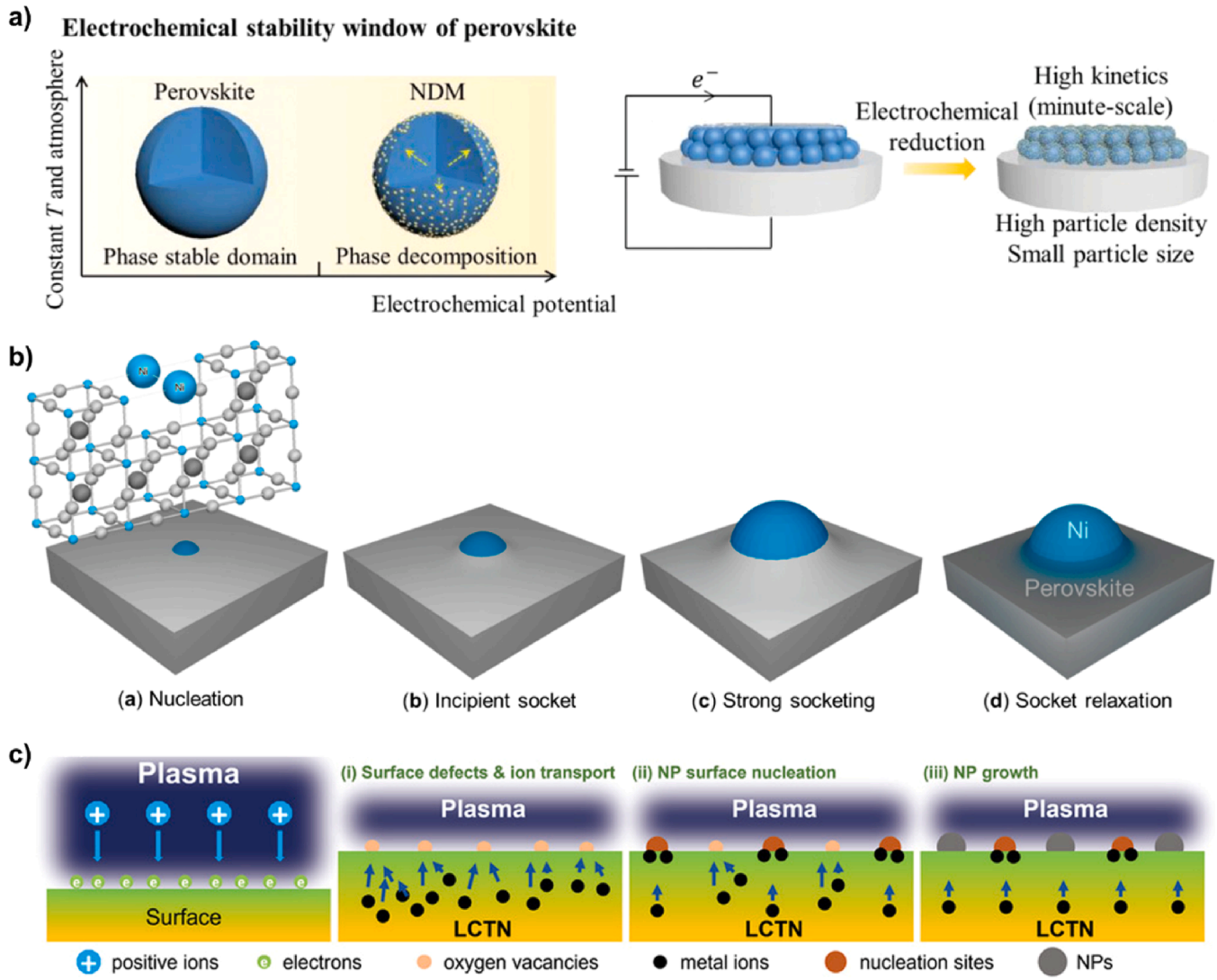

Fig. 3. a) Schematic illustrations of electrochemical exsolution, highlighting the electrochemical stability window of perovskites and showing how driving the potential into the non-stoichiometric decomposition regime enables rapid, minute-scale exsolution with high particle density and small particle size. Reproduced with permission [83]. Copyright 2022, Wiley-VCH. b) Schemes of thermally induced exsolution, depicting the evolution from initial nucleation to incipient socket formation, strong socketing, and subsequent socket relaxation, which collectively define the anchoring strength and reversibility of exsolved nanoparticles at the oxide surface. Reproduced with permission [99]. Copyright 2019, American Chemical Society. c) Schematic representation of the plasma-assisted exsolution of Ni nanoparticles from $La_{0.43}Ca_{0.37}Ti_{0.94}Ni_{0.06}O_{2.955}$ (LCTN), where energetic ions generate surface oxygen vacancies, accelerate metal ion migration, and promote rapid nucleation and growth of Ni nanoparticles at the near-surface region. Reproduced with permission [41]. Copyright 2022, Wiley-VCH.

synthesized $La_{0.7}Sr_{0.2}Co_{0.2}Fe_{0.8}O_{3-\delta}$ perovskite electrodes and investigated their exsolution under cathodic polarization conditions [93]. The applied potential selectively reduced Co cations, whereas Fe cations remained oxidized. This selective exsolution reflects the difference in the reduction potentials of Co and Fe, as well as the sensitivity of Co to electrochemical oxygen removal [94]. Upon polarization, the Co ions were exsolved uniformly over the entire electrode surface as nanoparticles, excluding direct electronic contact with the current collector. This observation indicated that the exsolution process was not confined to the electrode surface. Instead, the driving force of the reduction propagates through bulk and lattice oxygen exchange, enabling exsolution over large areas. This work demonstrates that electrochemical activation can drive spatially extended, metal-specific exsolution, offering a powerful means of tuning the catalytic activity of perovskites. Similarly, Fan et al. synthesized Fe−Ni-doped titanates with a composition of $La_{0.4}Ca_{0.4}Ti_{0.88}Fe_{0.06}Ni_{0.06}O_{3-\delta}$ and explored their electrochemical exsolution under anodic shock conditions [95]. The applied bias induced a strong reduction in the number of B-site cations and generated a high concentration of oxygen vacancies, which provided diffusion pathways for transition-metal migration toward the surface. Under voltage shock, numerous metallic nanoparticles were exsolved both on the surface and inside the grains, and transmission electron microscopy (TEM)-energy dispersive spectrometry (EDS) analysis revealed Ni^0-rich compositions and Fe−Ni alloy formation depending on the local environment. The exsolved particles exhibited a semi-embedded geometry and were distributed uniformly from the electrode surface into the bulk, indicating that the electrochemical driving force penetrated deeply into the perovskite and activated both surface and bulk exsolution. These results demonstrate that electrochemical shock can rapidly trigger the dense exsolution of multicomponent alloy nanoparticles in Fe−Ni co-doped titanates while preserving the perovskite framework and ensuring strong metal−support coupling. Recently, Zhang et al. demonstrated a potential-reduction-induced exsolution strategy on $Sr_{1.95}Fe_{1.3}Ni_{0.2}Mo_{0.5}O_{3-\delta}$ perovskite, achieving hyperfine $FeNi_3$ alloy nanoparticles at 800 °C under 1.8 V applied potential within 2 h [96]. This potential reduction approach leverages a

much lower oxygen partial pressure than conventional gas-phase reduction, enabling ultrafast nucleation and superior CO_2 electrolysis performance. These results highlight how precisely controlled cathodic potentials can accelerate multicomponent exsolution and complement earlier electrochemical exsolution studies on Cu- and Co/Fe-based systems.

2.3.2. Thermal annealing

Thermal annealing in a reducing atmosphere is the most established and widely applied approach for inducing the exsolution of oxide materials, as shown in Fig. 3b. In this method, gaseous reductants extract lattice oxygen and generate oxygen vacancies throughout the host framework [39,59,94,97–99]. These vacancies lower the reduction barrier for the guest metal cations and establish a chemical potential gradient that drives outward migration [39]. As the reduction force progresses from the bulk toward the surface, the metallic species nucleate and grow in a partially embedded configuration, which is a characteristic of classical exsolution. As thermal annealing activates long-range lattice diffusion under high-temperature and steady redox conditions, it enables the emergence of uniformly anchored nanoparticles across extended surfaces [8]. The particle size, distribution, and chemical composition can be tuned by adjusting the reduction temperature, gas composition, and reaction time, allowing for the controlled evolution of the exsolved phase. Jung et al. reported the thermal exsolution behavior of $La_{0.6}Sr_{0.4}CoO_{3-\delta}$ perovskites [97]. Because the Co−O bonds in this system are comparatively weak and surface oxygen is readily removed, reduction and vacancy formation occur efficiently, even at a relatively low temperature [100]. Once surface vacancies are generated, the Co ions are rapidly reduced and migrate through the near-surface vacancy network, nucleating as semi-embedded metallic nanoparticles. These Co nanoparticles remained strongly anchored during redox cycling, and their size and density were tunable by changing the reducing atmosphere and temperature. This study shows that titanate hosts containing highly reducible B-site cations can support thermally driven exsolution under mild conditions while preserving the characteristic anchored morphology of conventional thermal treatments. Similarly, Zhang et al. reported an exsolution process for $Sr_2Fe_{1.3}Ni_{0.2}Mo_{0.5}O_{6-\delta}$ perovskites containing Ni ions substituted in the B-site framework [59]. Under hydrogen annealing, the gradual removal of lattice oxygen generates a population of oxygen vacancies that lowers the reduction barrier for Ni and provides a diffusion pathway toward the surface. The reduced Ni species nucleated as metallic nanoparticles that were uniformly distributed across the perovskite surface. They found that the density of the Ni nanoparticles increased substantially in samples with deliberate A-site deficiencies. These A-site vacancies increase the local reducibility of the perovskite structure and strengthen the driving force for Ni migration, resulting in higher nucleation densities and smaller particle sizes [55]. Overall, the results indicate that thermal annealing reliably generates anchored Ni nanoparticles and that the exsolution tendency can be further tuned through A-site defect chemistry. To understand how electronic carriers influence the reduction and nanoparticle formation, Weber et al. compared the Ni exsolution behavior of $SrTiO_3$ perovskites with and without Nb doping [97]. In the Nb-free material ($SrTi_{0.95}Ni_{0.05}O_{3-\delta}$), a dense population of very small surface particles appeared after a short annealing and rapidly coarsened into a few large agglomerates as the annealing time increased, indicating fast growth and a strong tendency to form clusters. By contrast, in $SrTi_{0.9}Nb_{0.05}Ni_{0.05}O_{3-\delta}$, nanoparticles develop more gradually, remain more uniformly distributed on the surface, and show only moderate and steady growth in their average size over the same annealing window. These observations indicate that in the Nb-free material, the exsolved nanoparticles are highly mobile and easily coalesce into larger aggregates, whereas Nb doping stabilizes the finely dispersed and thermally robust nanoparticle population. When Nb is added, the electronic structure and defect distribution near the surface are modified, the lattice oxygen is removed more gradually during hydrogen annealing, and Ni migrates toward the surface in a more controlled manner. The exsolved nanoparticles remained finely dispersed and strongly anchored even after long annealing times, suggesting that tuning the carrier concentration and defect chemistry is an effective strategy for controlling the reduction depth, nanoparticle density, and long-term stability during thermal annealing. Overall, thermal annealing provides a deeply penetrating and robust reduction environment that drives long-range metal-ion migration and produces strongly anchored exsolved nanoparticles across various oxide hosts. Because this method relies on gas−solid redox reactions rather than electrochemical driving forces, it is highly effective for achieving large area exsolution, promoting alloy formation, and generating robust nanoparticle populations that remain stable under harsh reaction conditions.

2.3.3. Plasma treatment

Plasma-assisted exsolution provides an alternative low-temperature pathway for activating metal exsolution using energetic ions, electrons, and reactive radicals to extract surface oxygen without requiring bulk heating (Fig. 3c) [40,41]. When an oxide surface is exposed to plasma, high-energy species rapidly remove oxygen from the near-surface region, generating a high concentration of oxygen vacancies at very shallow depths [40]. These vacancies strengthen the local reducing environment and promote the reduction and migration of the guest metal cations toward the surface [39]. Because plasma induces a highly localized and nonequilibrium reduction, exsolution can occur even under ambient conditions, where conventional thermal annealing is ineffective. This surface-confined activation resulted in fast nucleation, high particle density, and minimal disturbance of the bulk crystal structure. For example, Tao et al. reported plasma-induced exsolution of Ca species in $La_{0.8}Ca_{0.2}MnO_3$ perovskites [25]. Plasma irradiation rapidly removes the surface oxygen within seconds, generating a highly defective and strongly reduced surface layer. Under these conditions, the substituted metal ions migrate toward the surface and nucleate as metallic nanoparticles without requiring high-temperature thermal activation. The resulting nanoparticles were significantly smaller and more densely distributed than those produced by conventional hydrogen annealing, demonstrating accelerated nucleation kinetics enabled by the plasma. Structural analyses confirmed that the perovskite bulk lattice remained unchanged, indicating that the plasma reduction was confined to the near-surface region. This study showed that plasma treatment can activate exsolution in systems that respond slowly or weakly to thermal reduction, providing a pathway for rapid catalyst generation while preserving bulk crystallinity. Khalid et al. investigated the plasma-induced exsolution in Ni-doped titanates ($La_{0.43}Ca_{0.37}Ti_{0.94}Ni_{0.06}O_{2.955}$), where Ni ions were incorporated into a Ti-centered lattice [41]. Plasma exposure rapidly removed surface oxygen, producing a highly reduced near-surface region that enabled the fast reduction and outward migration of Ni. Metallic Ni nanoparticles (3−10 nm of particle size) were formed within seconds and were much smaller and faster than those produced by thermal annealing. Because plasma reduction was confined to a shallow depth, the titanate lattice retained its bulk structure without a phase change [40]. This study demonstrates that plasma treatment can activate ultrafast surface-localized exsolution and produce uniformly anchored Ni nanoparticles under significantly milder conditions than conventional thermal processing. In a related study, Kyriakou et al. demonstrated that the reduction depth and oxygen vacancy density of Ni-containing titanates can be tuned by adjusting the plasma duration and power [40]. By adjusting the plasma duration and power, the extent of oxygen removal and vacancy density could be modulated, directly influencing Ni reduction and nucleation. Particle statistics comparing plasma-treated and H_2-reduced samples showed that suitable N_2 plasma conditions generate a much higher population of smaller Ni nanoparticles. Mild plasma treatments produced dense ultrafine nanoparticles restricted to the outermost layers, whereas stronger conditions enabled a slightly deeper reduction and larger particles,

while the bulk titanate structure remained intact. This work highlights that plasma-assisted exsolution provides a tunable and structurally gentle pathway for controlling the particle size, density, and anchoring depth. Overall, plasma-assisted strategies expand the design window for exsolution by decoupling the reduction process from bulk thermal requirements. The ability to trigger rapid, surface-confined exsolution with minimal structural perturbation enables precise control over the particle size and density, offering opportunities for thin-film catalysts, membranes, electronic devices, and systems where localized activation is desired.

2.3.4. Other methods

In addition to electrochemical, thermal, and plasma-based routes, a range of chemically assisted methods can also induce exsolution by modifying the surface defect chemistry or adjusting the local redox environment of the host oxide [88-91]. These approaches promote metal ion migration and reduction through selective cation removal, surface reconstruction, or reactive promoters, often under milder conditions than conventional reduction. Consequently, they expand the design space of exsolution and enable activation in systems that respond weakly to gas-phase or electrochemical treatments. Xie et al. demonstrated that alkali etching can promote exsolution by selectively removing the surface A-site species and creating a defect-rich surface layer [88]. The etched surface contains abundant oxygen vacancies and cation deficiencies, which significantly increase the reducibility of the oxide lattice. Under mildly reducing conditions, the metal ions migrate outward and form smaller and denser nanoparticles than those produced by thermal annealing alone. As the etched layer confined the reduction near the surface, the exsolved nanoparticles remained uniformly distributed and strongly anchored. This study shows that alkali treatment can effectively modulate the surface and lower the energy barrier for exsolution. Park et al. reported a novel water-mediated exsolution strategy for Ba-containing perovskite oxides under humid oxidizing atmospheres [89]. By doping alkali metals (Li^+, Na^+, and K^+) with high basicity and low electronegativity into the A-site of $BaCo_{0.4}Fe_{0.4}Zr_{0.18}Y_{0.02}O_{3-\delta}$, they achieved spontaneous exsolution of BaO_x nanoparticles when exposed to wet air (3 vol% H_2O) at 600 °C. Among the tested compositions, $K_{0.05}Ba_{0.95}Co_{0.4}Fe_{0.4}Zr_{0.18}Y_{0.02}O_{3-\delta}$ (KBCFZY) exhibited the most uniform exsolution of BaO_4 nanoparticles (~84 nm). Unlike conventional exsolution methods that require a reducing atmosphere to precipitate B-site transition metals, this approach utilizes the high reactivity of alkali metal dopants with water vapor to trigger A-site cation (Ba) exsolution under practical operating conditions. Alkali metal doping lowered both Ba and oxygen vacancy formation energies, creating preferential nucleation sites for BaO_x precipitation. This strategy demonstrates that exsolution can be rationally engineered not only for electron-mediated redox catalysis but also for ion transport enhancement in humid oxidizing environments. In addition, Zhang et al. reported an in situ electrochemical reconstruction strategy to create dynamically stable $Cu^{\circ}Cu^{\delta+}$ pair sites at the interface between exsolved Cu nanoclusters and $CaCO_3$ nanospheres [91]. The $CaCu_3(OH)_6Cl_2$ kagome precursor undergoes electrochemical transformation under CO_2 reduction conditions, where Cl^- ions are replaced by OH^- due to higher Cu−Cl ionicity, followed by Cu^{2+} reduction to metallic Cu at controlled potentials, while CO_2 triggers $CaCO_3$ formation by suppressing Ca leaching ($Ca(OH)_2$ solubility product ≫ $CaCO_3$). This process generates highly dispersed Cu nanoclusters anchored on $CaCO_3$ nanospheres without causing bulk structural damage. DFT calculations reveal that the nanocluster size results from the balance between the Cu and Cu cohesive energy and the Cu−O(CO_3) metal−support interactions. The high anion vacancy formation energy of $CaCO_3$ (6.285 eV for carbonate removal) stabilizes interfacial $Cu^{\delta+}$ with low electron affinity (3.01 eV), maintaining the $Cu^{\circ}Cu^{\delta+}$ pair stability even at cathodic potentials. This strategy demonstrates that carbonate chemistry offers an alternative exsolution pathway that is complementary to traditional metal exsolutions from reducing atmospheres. As an alternative method, Chattopadhyay et al. explored the exsolution of CdS via the room-temperature sulfidation of $La_{0.4}Sr_{0.4}Cd_{0.05}Ti_{0.95}O_{3-\delta}$ perovskites [90]. Because Cd-containing phases are difficult to process using conventional high-temperature routes because of the low melting points of CdO and CdS, they designed an exsolution pathway that avoids thermal reduction-based exsolution and couples hydrothermal host formation with chemical sulfidation. This simple exsolution method was achieved by the vapor-phase reaction of $La_{0.4}Sr_{0.4}Cd_{0.05}Ti_{0.95}O_{3-\delta}$ with in situ-generated H_2S by adding concentrated HCl to the Na_2S powder. The strong affinity of Cd^{2+} with S^{2-} chemically promotes diffusion of Cd^{2+} toward the surface and nanoscale grain size with high porosity of the host perovskite could lower free energy required for diffusion and exsolution. The size of the exsolved CdS nanoparticle was estimated to be approximately 3.5 nm, supporting the formation of CdS nanodots rather than larger crystallites. This exsolution-derived CdS is strongly anchored to the perovskite support, which helps protect the CdS and thereby suppresses photocorrosion and leaching, while offering a practical platform for the low-temperature exsolution of other catalytically active nanoparticles. Collectively, these chemically assisted and interface-mediated routes offer a versatile means to adjust surface defect chemistry, local reducibility, and cation mobility without relying solely on high-temperature or electrochemical driving forces. By exploiting alkali etching, water-mediated oxidation, and other driving forces, they broadened the applicability of exsolution to systems requiring gentle activation or finely tailored interfacial environments.

Exsolution methods offer distinct advantages and disadvantages depending on how the reduction driving force is delivered to the host lattice. Electrochemical exsolution enables low temperature, rapid, and spatially selective nanoparticle formation under applied bias, making it useful for in situ catalyst activation. However, it is generally limited to electrochemically accessible regions and may be less suitable for large scale bulk activation. Thermal annealing remains the most established and scalable route, providing deep reduction, long-range cation diffusion, and strongly anchored nanoparticles across extended surfaces. But this method typically requires high temperatures and may lead to particle coarsening if not carefully controlled. Plasma-assisted exsolution allows ultrafast, surface-confined nanoparticle formation under relatively mild conditions with minimal disturbance to the bulk structure. However, its shallow reduction depth and limited uniformity over large areas can restrict practical implementation. Chemically assisted routes, including etching-, water-mediated-, and sulfidation-based methods, expand the exsolution toolbox by enabling activation under gentler or more specialized conditions. Nevertheless, these approaches often show lower generality and more complex control over phase selectivity and compositional homogeneity. Overall, although each method differs in activation mode, depth of reduction, and controllability, they can provide commonly versatile pathways for tailoring nanoparticle size, dispersion, and metal−support interactions according to the desired catalytic and functional requirements.

3. Diverse application of exsolved materials

Exsolution-derived materials leverage the synergistic properties of both the host lattice and exsolved nanoparticles, offering a distinctive advantage over conventional catalysts. The partially-embedded nanoparticles (“socketed” structure) impart exceptional structural and chemical stability, preventing particle agglomeration and preserving uniform dispersion under demanding operating conditions. This dual functionality, combined with their robustness, has enabled their application in diverse fields, including electrocatalysis, photocatalysis, fuel cells, and batteries, where both catalytic activity and operational durability are essential [55]. This section reviews the key applications of exsolution-based materials and highlights how this strategy has continued to expand the catalytic landscape.

3.1. Electrocatalysis

Electrocatalysis plays a pivotal role in realizing a sustainable society because it enables the production of valuable chemicals, such as hydrogen, ammonia, and carbon-based compounds, without relying on fossil fuels. Various catalysts based on noble and non-noble transition metals have been extensively investigated to improve the efficiency of electrochemical energy conversion [101,102]. However, industrial-scale hydrogen evolution reaction (HER) and oxygen evolution reaction (OER) remain predominantly reliant on noble metal-based catalysts such as Pt/C, RuO_2/C, and IrO_2/C. For emerging electrocatalytic reactions, including CO_2 reduction (CO_2RR), oxygen reduction reaction (ORR), nitrogen reduction (NRR), and nitrate reduction (NO_3RR), achieving both high yield rate and Faradaic efficiency remains a critical challenge for practical applications. The exsolution strategy has emerged as a promising route for overcoming these limitations by generating strongly anchored and size-tunable metallic nanoparticles within robust oxide matrices. The intimate metal−matrix interface plays a dual role: stabilizing the exsolved nanoparticles against agglomeration, while simultaneously enhancing the electronic coupling between the metal and support. This synergistic interaction accelerates charge transfer kinetics and enhances catalytic durability, making exsolution-derived catalysts promising alternatives to conventional approaches for diverse electrocatalytic applications.

Electrocatalysis operates at the electrode−electrolyte interface, where reaction rates are governed by interfacial charge transfer and the adsorption energetics of key intermediates. According to the Sabatier principle, an ideal electrocatalyst should bind reaction intermediates neither too strongly nor too weakly, giving rise to volcano-type activity trends. In water splitting, HER is controlled by the adsorption and desorption balance of H*, whereas OER requires the stepwise stabilization of HO*, O*, and HOO* intermediates. For ORR, the catalyst must promote the selective $4e^-$ pathway over the $2e^-$ pathway. In CO_2RR, efficient CO_2 activation and stabilization of COOH/CO-type intermediates are essential, while NRR and NO_3RR rely on stepwise proton-coupled electron transfer to activate the strong N≡N or N−O bonds and produce NH_3. From this perspective, exsolution-derived catalysts are particularly attractive because the metal−oxide interface can simultaneously tune intermediate binding, accelerate charge transfer, and stabilize nanoscale active sites, thereby improving both activity and durability across diverse electrocatalytic reactions.

3.1.1. Water splitting

Among the various electrocatalytic processes, water splitting, including both the HER and OER, has been most intensively explored using exsolution-based catalysts [48,103,104]. Robust oxide scaffolds and embedded metallic sites provide remarkable durability and bifunctional activity, making exsolved systems attractive alternatives to conventional noble-metal catalysts. Electrocatalysis is one of the most important areas for achieving a sustainable society because it can produce useful products such as ammonia, hydrogen, and carbon compounds without fossil fuels. Owing to their advantageous characteristics, numerous types of materials, including noble metals, nonnoble metals, and metal-free compounds, have been investigated. However, to date, only noble metal catalysts (Pt/C, RuO_2/C, and IrO_2/C) have achieved industrial efficiency in hydrogen production (HER and OER); for other electrocatalytic reactions, the yield rate and efficiency are still insufficient for industrialization (CO_2RR, NRR, and NO_3RR).

The exsolution strategy is a promising candidate for overcoming these limitations owing to its unique characteristics. In particular, the robust features of the matrix and the strong interactions between the exsolved species and the matrix provide size tunability and stability. For example, Bai et al. reported a triphenylphosphine-assisted exsolution strategy for the Ruddlesden−Popper (RP)-type perovskite $PrSrCo_{0.2}Fe_{0.8}O_4$ (PSCFO), where phosphorus doping and in situ Co/Fe exsolution produced a highly active OER catalyst (PSCFO-T), as illustrated by the TEM image in Fig. 4a [105]. The initially inert perovskite became catalytically active after reductive treatment, reducing the overpotential from > 500 to ~480 mV at 10 mA cm^{-2}; after additional IrO_2 nanocluster loading, the optimized catalyst reached 305 mV at 10 mA cm^{-2} under alkaline conditions (Fig. 4b and c). Similarly, Zuo et al. developed a 'double E' strategy combining exsolution and electrodeposition to design bifunctional perovskite electrocatalysts [106]. In this approach, Fe nanoparticles were exsolved from $La_{0.25}Ca_{0.65}Ti_{0.95}Fe_{0.05}O_3$ (R-LCTFe) and trace amounts of Ni were subsequently electrodeposited to yield a composite R-LCTFe/Ni catalyst. The optimized sample exhibited low overpotentials of 349 mV (OER) and 309 mV (HER) at 10 mA cm^{-2} under alkaline conditions. It also achieved overall water splitting at 1.58 V with excellent durability over 24 h, which was attributed to the synergistic interaction between the exsolved Fe nanoparticles and electrodeposited Ni species, which markedly reduced the charge transfer resistance, as shown in Fig. 4d and 4e. In addition, Buchauer et al. reported a highly durable Ni−Fe-exsolved perovskite catalyst that maintained outstanding OER activity under industrial conditions (25−150 °C, 50 bar, 10 M KOH) [107]. Their team synthesized $Sr_{0.98}Ti_{0.7}Fe_{0.25}Ni_{0.05}O_3$ (STFNO) perovskite precursors and thermally reduced them under 4% H_2/Ar at 800 °C, yielding NiFe alloy nanoparticles exsolved from the oxide matrix. High resolution-transmission electron microscopy (HR-TEM) revealed a core-shell-like morphology with a metallic core and a thin oxide shell. However, in situ TEM confirmed that the shell layer formed only after air exposure, indicating spontaneous surface oxidation (Fig. 4f). The resulting NiFe@oxide interface provided enhanced charge transfer and surface stability, enabling continuous OER operation at high current densities and under elevated temperature-pressure conditions (Fig. 4g). Chen et al. demonstrated low-temperature exsolution of CoFeNi ternary alloy nanoparticles from A-site-deficient $Sr_{0.9}Co_{0.5}Fe_{0.35}Ni_{0.15}O_{3-\delta}$ (SCFN) perovskite via the thermal reduction at 350 °C in 10% H_2/Ar [108]. The socketed nanoparticles created strong metal−support interactions, generating abundant oxygen vacancies and electrochemically active O_2^{2-} species that delivered exceptional OER performance with low overpotential of 282 mV at 10 mA cm^{-2} in 1 M KOH. This ternary alloy−perovskite system highlights versatility of exsolution in engineering multicomponent nanoparticles with synergistic electronic coupling for superior OER catalysts.

3.1.2. Others

In addition to water splitting (HER and OER), there are various electrocatalytic processes with useful products, such as the NRR, NO_3RR, ORR, CO_2RR, etc. [45,46,109]. Owing to the thermal and chemical stabilities of perovskite oxide structures, conventional exsolution catalysts can achieve higher conversion efficiencies because they can operate at high temperatures, which helps to overcome the activation energy of the rate determining step. For instance, Xia et al. synthesized a RP-phase perovskite, $Pr_4Ni_{1.8}Co_{1.2}O_{10-\delta}$ (PNCO), and demonstrated its high activity for electrochemical ammonia synthesis at 350 °C [110]. The catalyst exhibited a remarkable NH_3 yield rate of 27.84 μg h^{-1} cm^{-2} with a Faradaic efficiency of 62.6%. Further incorporation of trace Ru ions into the PNCO matrix ($PNCRu_{0.01}O$) followed by reductive treatment under 5% H_2/Ar at 400 °C ($PNCRu_{0.01}O$−Re) resulted in the exsolution of NiCo alloy nanoparticles, as confirmed by TEM imaging. The synergistic effect of Ru doping and NiCo exsolution significantly improved both NH_3 yield and Faradaic efficiency. In addition to the NRR, the electrochemical NO_3RR has emerged as an efficient route for sustainable ammonia production [111]. Zuo et al. developed an exsolution-based NO_3RR catalyst that achieved a yield rate of 4.1 mg h^{-1} mg_{cat}^{-1} and a Faradaic efficiency of 76% at −0.7 V [112]. They prepared $La_{0.9}Fe_{0.3}Cu_{0.7}O_3$ perovskites and annealed them under a H_2/Ar atmosphere, resulting in the surface exsolution of Cu nanoparticles (LFC−E). The exsolved Cu sites exhibited outstanding NH_3 productivity with a Faradaic efficiency approaching 80%, demonstrating the great promise of exsolution-based catalysts for multistep

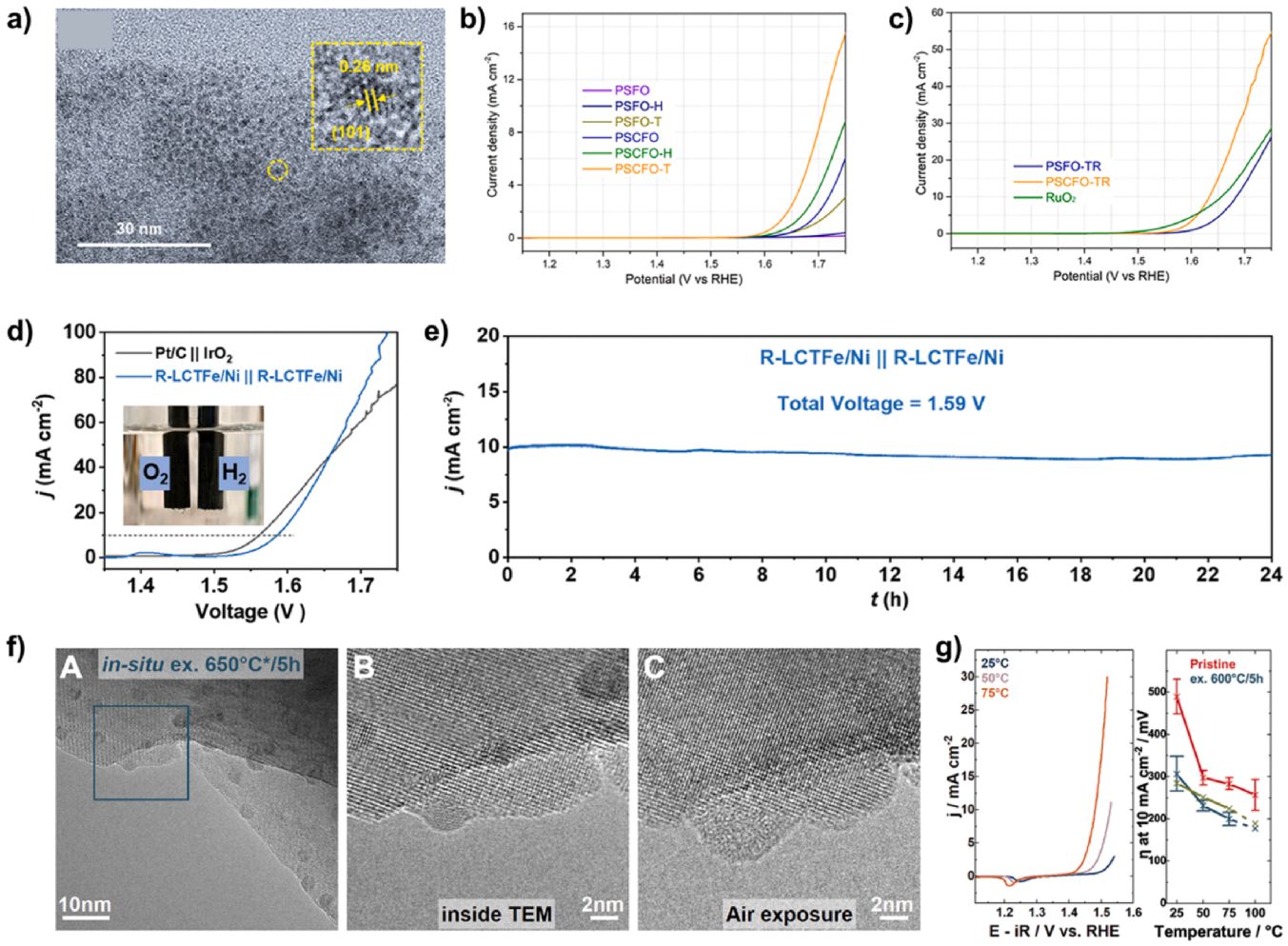

Fig. 4. a) TEM image of $PrSrCo_{0.2}Fe_{0.8}O_4$ (PSCFO) after exsolution, showing finely dispersed surface nanoparticles anchored on the layered perovskite matrix. b, c) Linear sweep voltammetry (LSV) curves of pristine and exsolved PSCFO under different treatment conditions, demonstrating that nanoparticle exsolution markedly enhances OER activity. Reproduced with permission [105]. Copyright 2024, Wiley-VCH. d) Overall water splitting polarization curves of R-$La_{0.25}Ca_{0.65}Ti_{0.98}Fe_{0.05}O_3$/Ni (R-LCTFe/Ni) paired electrodes and commercial Pt/C||IrO_2, and e) long-term stability at 1.59 V, indicating efficient and durable overall water splitting enabled by exsolution. Reproduced with permission [106]. Copyright 2025, Wiley-VCH. f) In situ and ex situ TEM images of NiFe-$Sr_{0.98}Ti_{0.7}Fe_{0.25}Ni_{0.05}O_3$ (NiFe-STFNO), revealing the evolution of nanoparticle−oxide interfaces under operating and air-exposed conditions, and g) temperature-dependent OER performance, showing improved activity at elevated temperatures owing to well-coupled NiFe nanoparticles on the STFNO matrix. Reproduced with permission [107]. Copyright 2025, American Chemical Society.

nitrogen-cycle reactions.

3.2. Photocatalysis

Although exsolution strategies have primarily been applied to electrochemical systems, they also exhibit great potential for photocatalytic applications. Because metal nanoparticles, nanoclusters, and single atoms can function as photosensitizers, electron mediators, and charge reservoirs [113], exsolved metals anchored within semiconducting matrices with suitable band structures can effectively promote photo-induced charge separation and interfacial reactions. The strong electronic coupling between the exsolved species and semiconductor matrix facilitates the efficient transfer of photogenerated carriers, thereby enhancing the overall photocatalytic efficiency. Among the various semiconducting hosts, $LaFeO_3$ has been considered a representative candidate for photocatalytic CO_2RR owing to its favorable band alignment and chemical stability. For example, Zhang et al. synthesized Cu nanoparticle-anchored $LaFeO_3$ via an exsolution approach, yielding a composite Cu−$LaFeO_3$ (LCFO) as an efficient photocatalyst for the CO_2RR [114]. TEM analysis confirmed the uniform distribution of Cu nanoparticles on the $LaFeO_3$ surface (Fig. 5a and 5b). The LCFO catalyst exhibited enhanced CO_2 reduction selectivity, and the reaction proceeded toward CH_4 formation with an improved Faradaic efficiency (Fig. 5c). These results highlight that the exsolved Cu nanoparticles act as active photosensitizers that promote CO_2 adsorption and electron transfer, thereby accelerating the reduction pathway toward multi-electron products. In another study, Li et al. reported an exsolution-based Ru−$SrTiO_3$ photocatalyst capable of visible-light-driven hydrogen evolution [115]. $Sr_{0.9}Ti_{0.9}Ru_{0.1}O_{3-\delta}$ (STRO) nanofibers were first synthesized by electrospinning and calcination in ambient atmosphere, followed by in situ exsolution of Ru nanoparticles through reductive annealing at 900 °C under 5% H_2 (R−STRO). The resulting R−STRO catalyst exhibited a markedly increased hydrogen production rate of 86.0 μmol h^{-1} g^{-1} compared with 58.0 μmol h^{-1} g^{-1} for the pristine STRO (Fig. 5d–f). The enhanced activity was attributed to the efficient separation of photoexcited carriers at the Ru−oxide interface and improved light absorption induced by the metallic Ru species.

3.3. Solid oxide fuel cells

SOFC directly converts the chemical energy of a fuel and an oxidant

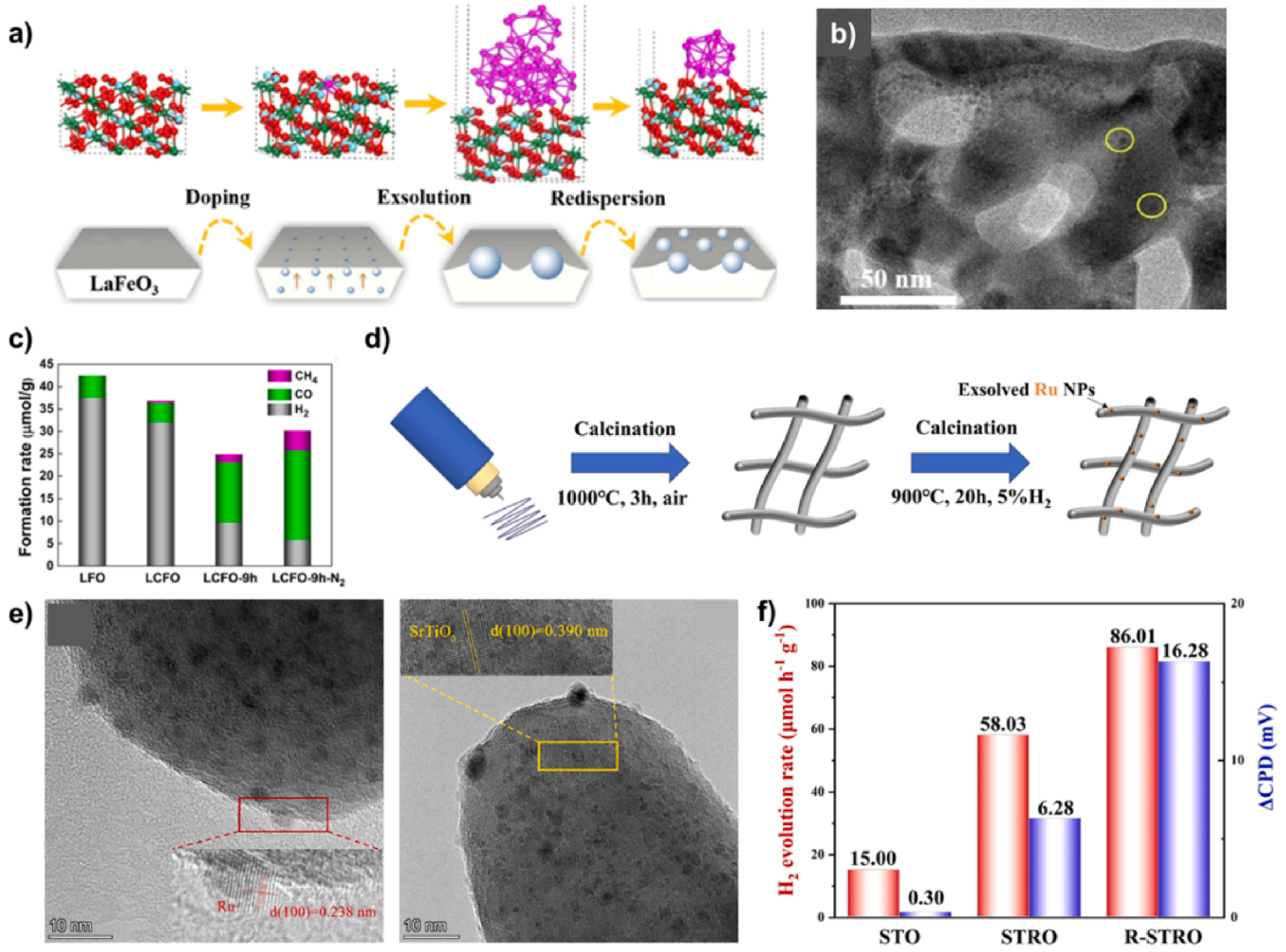

Fig. 5. a) Synthetic routes for Cu-exsolved $LaFeO_3$ (LCFO), illustrating Cu doping, exsolution of Cu nanoparticles, and their subsequent redispersion on the perovskite surface. b) TEM image of LCFO showing uniformly distributed Cu nanoparticles anchored on the $LaFeO_3$ matrix, and c) CO_2 conversion rate of the $LaFeO_3$ and LCFO under visible-light irradiation, where LCFO exhibits enhanced CH_4/CO formation rates compared with pristine $LaFeO_3$, indicating that exsolved Cu nanoparticles promote multi-electron CO_2RR pathways. Reproduced with permission [114]. Copyright 2023, Elsevier. d) Synthetic method of Ru-exsolved $SrTiO_3$ (R-STRO) nanofibers via electrospinning, calcination, and reductive annealing. e) TEM images of R-STRO showing Ru nanoparticles at the $SrTiO_3$ surface with clear lattice fringes for both phases, confirming the formation of well-coupled Ru−$SrTiO_3$ heterointerfaces. f) photocatalytic H_2 evolution rates and contact potential difference values for $SrTiO_3$, $Sr_{0.9}Ti_{0.9}Ru_{0.1}O_{3-\delta}$ (STRO), and R-STRO, demonstrating that in situ exsolved Ru nanoparticles significantly enhance H_2 production and improve charge-separation efficiency relative to Ru-free $SrTiO_3$. Reproduced with permission [115]. Copyright 2022, Elsevier.

into electricity, typically using H_2 as the fuel and O_2 as the oxidant, and operate at elevated temperatures with oxide-ion-conducting electrolytes. Under these conditions, fuel cell electrodes must maintain high activity and durability under severe redox and thermal conditions. Metal/oxide fuel electrodes are widely employed in many practical SOFC systems because of their high electronic conductivity and excellent hydrogen oxidation activities [116,117]. However, they suffer from particle agglomeration, electrochemical instability, and carbon deposition in case of carbon-based fuels, leading to performance degradation and limited long-term stability [118]. These challenges have motivated an increasing interest in exsolution-derived oxide fuel cell electrodes. In such electrodes, catalytically active metal cations are exsolved from the perovskite lattice under reducing conditions and form nanoparticles embedded in the oxide backbone (socketed structure). Compared to conventional fuel cell catalysts, this socketed structure ensures strong electronic coupling between the nanoparticles and the host matrix and preserves the nanoscale dispersion of the active phase under harsh redox and thermal conditions. In addition, the oxide backbone provides continuous pathways for charge and mass transport, allowing the exsolved nanoparticles to participate in reactions over a larger effective electrode area, leading to improved electrochemical activity and durability during SOFC operation. For example, Hu et al. prepared an A-site-deficient $(Ba_{0.9}La_{0.1})_{0.95}Co_{0.7}Fe_{0.2}Nb_{0.1}O_{3-\delta}$ (BL95CFN) perovskite via a conventional solid-state route and induced Co−Fe nanoparticle exsolution under reducing conditions (Fig. 6a) [119]. The A-site deficiency increases the driving force for B-site reduction [8] leading to a high density of semi-embedded Co−Fe alloy particles that enlarge the active surface for the hydrogen oxidation reaction (HOR) while remaining strongly anchored to the host oxide matrix. Consequently, the BL95CFN anode exhibits very low polarization resistance, down to 0.05 Ω cm^2 at 800 °C, and an electrolyte-supported single cell reaches a maximum power density of about 513.2 mW cm^{-2} at 750 °C. In addition, when operated with wet CH_4 fuel, the cell maintains a stable voltage for 200 h at 200 mA cm^{-2} and shows no detectable carbon peaks in Raman spectra (Fig. 6b and 6c), indicating excellent coking tolerance compared with a conventional Ni-based anode [120]. This design results in a low polarization resistance and stable operation, even under methane operation, because the socketed nanoparticles resist agglomeration and suppress carbon accumulation at the fuel electrode surface [37].

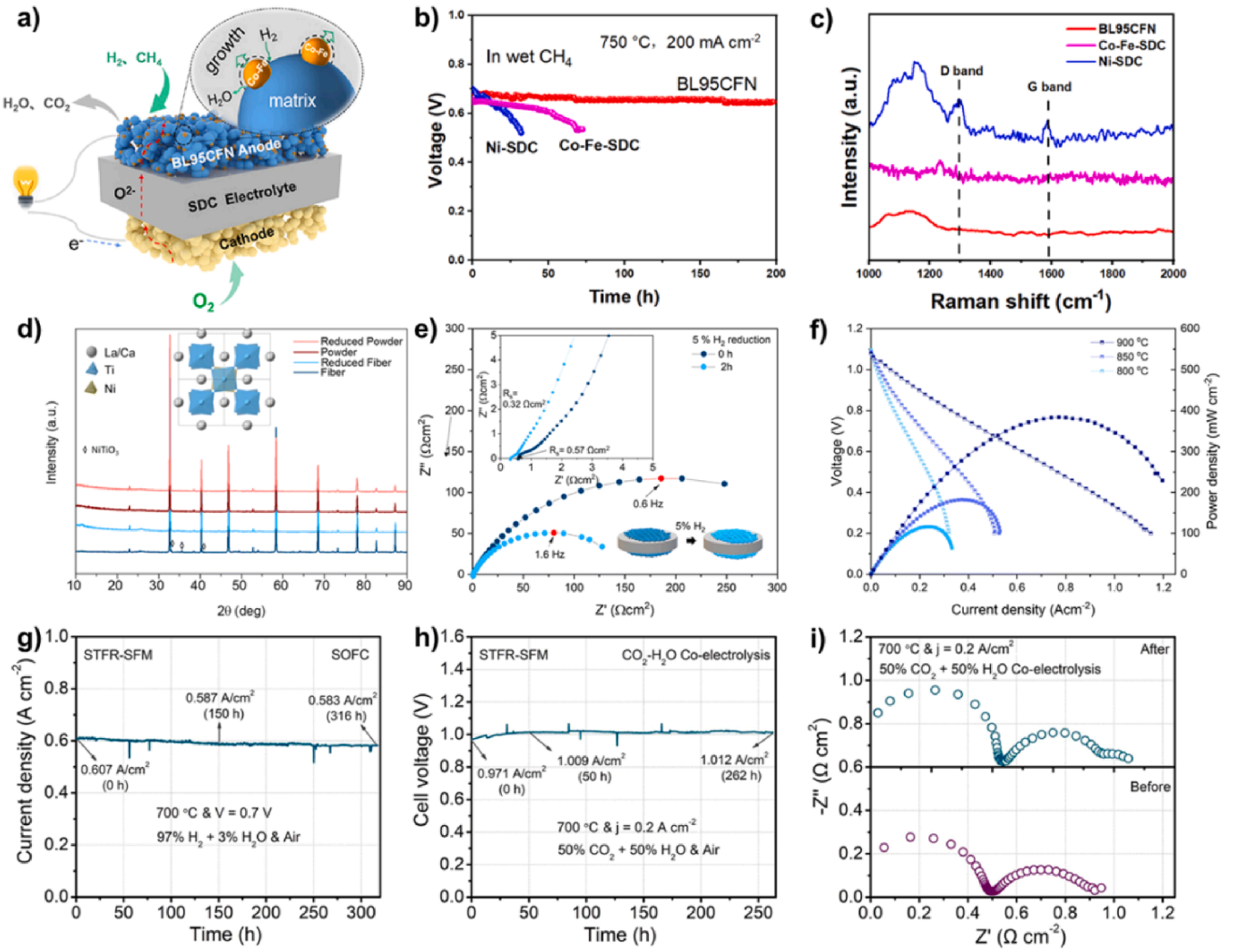

Fig. 6. a) Schematic of solid oxide fuel cell (SOFC) consist of $(Ba_{0.9}La_{0.1})_{0.95}Co_{0.7}Fe_{0.2}Nb_{0.1}O_{3-\delta}$ (BL95CFN) anode, $Sm_{0.2}Ce_{0.8}O_{2-\delta}$ (SDC) electrolyte, and $(Ba_{0.9}La_{0.1})_{0.95}Co_{0.7}Fe_{0.2}Nb_{0.1}O_{3-\delta}$−40 wt% SDC (BSCF-40SDC) cathode. b) long-term stability of BL95CFN|SDC|BSCF-40SDC, NiO-SDC|SDC|BSCF-40SDC, and Co−Fe-SDC|SDC|BSCF-40SDC cells under wet CH_4 at 750 °C and 200 mA cm^{-2}, showing BL95CFN maintains nearly constant voltage while conventional Ni-based and Co−Fe anodes degrade. c) Raman spectra after operation under CH_4 fuel, with the absence of D and G bands for BL95CFN indicating efficient suppression of carbon deposition. Reproduced with permission [119]. Copyright 2022, American Chemical Society. d) X-ray diffraction (XRD) patterns of powder and fiber $La_{0.52}Ca_{0.28}Ni_{0.06}Ti_{0.94}O_3$ (LCNT) before and after exsolution under 5% H_2/N_2 at 800 °C for 4 h, showing retention of the perovskite framework and metallic Ni reflections only in reduced fibers, e) Electrochemical impedance spectroscopy (EIS) data of the fiber-based LCNT symmetric cells reduced at 800 °C for 0 and 2 h, revealing a drastic decrease in polarization resistance as densely and uniformly dispersed Ni nanoparticles are exsolved on the fiber backbone, and f) corresponding I−V−P curves , demonstrating significantly enhanced electrode performance after Ni exsolution. Reproduced with permission [122]. Copyright 2023, The Royal Society of Chemistry. g) Current density vs. time for $Sr_{0.95}Ti_{0.3}(Fe_{0.9}Ru_{0.1})_{0.7}O_{3-\delta}$−$Sr_2Fe_{1.5}Mo_{0.5}O_{6-\delta}$ (STFR–SFM) at 700 °C and 0.7 V in SOFC mode, showing nearly constant current over 300 h, h) Cell voltage vs. time at 700 °C and 0.2 A cm^{-2} in CO_2−H_2O co-electrolysis mode, showing stable operation over 250 h, and i) Nyquist plots before and after the co-electrolysis, indicating unchanged total ad interfacial resistances. Reproduced with permission [123]. Copyright 2025, Elsevier.

Similarly, Amaya-Dueñas et al. also developed an A-site-deficient $La_{0.65}Sr_{0.3}Cr_{0.85}Ni_{0.15}O_{3-\delta}$ (L65SCrN), as a fuel cell electrode capable of in situ Ni exsolution under reducing conditions [121]. After reduction, the metallic Ni nanoparticles were well dispersed on the chromite grain surfaces without decomposition of the bulk perovskite phase. An electrolyte-supported solid oxide fuel cell using L65SCrN as the fuel electrode and $La_{0.58}Sr_{0.4}Fe_{0.8}Co_{0.2}O_{3-\delta}$ (LSCF) as the air electrode delivers overall cell resistances and operating voltages comparable to state-of-the-art Ni−$Ce_{1-x}Gd_xO_{2-\delta}$ (Ni-CGO) anodes at 860 °C, and maintains stable co-electrolysis operation for 950 h with a voltage degradation rate below ~3.5 mV/1000 h, demonstrating that chromite-based exsolved Ni electrodes can combine phase stability with competitive cell-level performance. Xu et al. investigated $La_{0.52}Ca_{0.28}Ni_{0.06}Ti_{0.94}O_3$ (LCNT) with deliberate A-site deficiency as a host for Ni exsolution in fiber-based SOFC electrodes under electrochemical switching. They first compared powder and electrospun fiber architectures under pure thermal reduction and then evaluated electrochemically driven exsolution in working SOFC electrodes [122]. For the powder/fiber comparison, LCNT samples were thermally reduced under 5% H_2/N_2 at 800 °C. X-ray diffraction (XRD) analysis revealed that the original crystal structure of the host layer was preserved after annealing, whereas additional diffraction peaks attributable to metallic Ni appeared in the LCNT fiber (Fig. 6d). Under the same thermal reduction conditions, the Ni nanoparticles were exsolved more densely and uniformly on the LCNT fibers than on the powder, forming finely dispersed, strongly anchored particles on the fiber backbone. To apply the LCNT fibers as SOFC electrodes, the fibers were first fabricated into LCNT fiber/yttria stabilized zirconia (YSZ)/LCNT fiber cells and thermally pre-reduced to activate Ni exsolution. After this activation step, they applied an anodic bias to LCNT fiber/YSZ/LCNT fiber cells operated

under wet H_2 flow, which generated extremely low local oxygen partial pressures at the electrode and markedly accelerated the nucleation and growth of finely dispersed Ni nanoparticles [95]. This configuration provides a high density of strongly anchored active sites and short diffusion paths for reactants and charge carriers, resulting in a drastic decrease in polarization resistance from 6.02 to 0.69 Ω cm^2 and a maximum power density of ~380 mW cm^{-2} at 900 °C (Fig. 6e and 6f). These results demonstrate that electrochemically driven exsolution can be exploited as an efficient strategy to rapidly activate and periodically regenerate fuel-cell electrode catalysts during SOFC operation. Alternatively, Han et al. synthesized an A-site-deficient $Sr_{0.95}Ti_{0.3}(Fe_{0.9}Ru_{0.1})_{0.7}O_{3-\delta}$ (STFR) perovskite as an Fe−Ru exsolution host and mixed it with the highly conducting double perovskite $Sr_2Fe_{1.5}Mo_{0.5}O_{6-\delta}$ (SFM) to form a composite fuel cell electrode [123]. In this architecture, in situ exsolved Fe−Ru nanoparticles on the STFR provide highly active sites for fuel oxidation and CO_2/H_2O electrolysis, whereas the SFM network enhances electronic conduction and reduces ohmic losses. The STFR−SFM fuel cell electrodes achieved peak power densities above 1.5 W cm^{-2} in fuel-cell mode and current densities above 1.75 A cm^{-2} at 1.3 V in steam electrolysis and 2.15 A cm^{-2} at 1.3 V in direct CO_2 electrolysis at 800 °C, with excellent durability and preferential selectivity toward CO_2 electrolysis (Fig. 6g and h). In addition, the electrochemical impedance spectroscopy (EIS) results before and after the reaction exhibit negligible changes, indicating that the interfacial resistance remains essentially unchanged (Fig. 6i). The synergy between the catalytically active exsolved alloys and the conductive backbone enables high power density and current output in both fuel cell and electrolysis modes, together with good stability in CO_2-containing feeds. Recently, multicomponent exsolution has further expanded these capabilities for solid oxide electrolysis cells (SOECs). Zhang et al. reported a high-entropy perovskite symmetric electrode, $Pr_{0.5}Ba_{0.5}Mn_{0.2}Fe_{0.2}Co_{0.2}Ni_{0.2}Cu_{0.2}O_{3-\delta}$ (HE-PBM), where B-site multi-transition metal doping (Mn/Fe/Co/Ni/Cu) drove in situ exsolved FeCoNiCu quaternary alloy nanoparticles from cathode and enhanced $Mn^{4+} \rightarrow Mn^{3+}$ redox at anode, generating abundant oxygen vacancies for bifunctional OER/CO_2RR (Rp = 0.289 cm^2, 1.21 A cm^{-2} at 2.0 V, 800 °C) with superior coking tolerance in symmetrical SOEC [124]. This high-entropy design exploits multi-element synergy across both electrodes, leveraging quaternary alloy nanoparticles for CO_2 reduction and transition metal redox couple for oxygen evolution, demonstrating exceptional stability without carbon deposition.

These representative studies demonstrate that exsolution-based fuel electrodes are highly compatible with practical SOFC operations and can directly address the intrinsic limitations of conventional metal/oxide anodes. In situ generated socketed metal nanoparticles provide robust, coke-resistant active sites that maintain nanoscale dispersion and electrochemical activity under severe redox and hydrocarbon fuel environments, whereas the perovskite host offers stable structural support and continuous pathways for charge and mass transport. By tuning the A-site deficiency, choosing suitable host lattices such as chromites and titanates, integrating conductive backbone phases, and using electrochemical switching to trigger or refresh exsolution, it is possible to realize fuel electrodes that combine high power density with long-term stability in both H_2 and carbon-containing fuels, as well as under electrolysis conditions.

3.4. Batteries

Secondary batteries have emerged as key candidates for next-generation energy storage. However, their practical performance remains limited by several intrinsic factors depending on the underlying electrochemical system. In metal-ion batteries, including Li-, Na-, and K-ion batteries, key challenges arise from the intrinsically low electronic conductivity of oxide electrodes, sluggish ion diffusion (particularly for Na^+ and K^+), and severe structural degradation associated with repeated ion insertion/extraction or conversion reactions [125,126]. In addition, insufficiently active electrode surfaces often restrict charge transfer kinetics, resulting in limited reversible capacity and poor rate capability. To overcome these limitations, exsolution has recently gained significant attention as an efficient strategy for engineering highly functional metal/oxide hybrid architecture [127,128]. Through electrochemical or thermal forces, exsolution generates strongly anchored metallic nanophases that establish conductive pathways, introduce defect-rich interfaces, and stabilize the host lattice during repeated cycles. These coupled effects enable faster charge transfer, improved ion transport, and enhanced structural robustness across diverse metal ion battery chemistries. Sharma *et al.* synthesized a series of Fe-doped NASICON-type $Na_3Fe_xV_{2-x}(PO_4)_3$ (x = 0.05, 0.1, 0.15, and 0.2) cathode materials (NFVP-x) for Na-ion batteries (SIBs) and systematically investigated the role of exsolved iron phosphide nanoparticles in enhancing their electrochemical performance [129]. Nanosized NFVP-x powders were synthesized via a hydrothermal method and subsequently calcined at 800 °C under a 10% H_2/N_2 atmosphere (Fig. 7a). In Fig. 7b, the diffraction patterns confirm that FeP peaks begin to appear at $x \geq 0.10$ and increase with higher Fe content, while the underlying NASICON structure remains preserved. NFVP-0.15 showed an optimal balance between the structural integrity and FeP formation, exhibiting the highest crystallinity without excessive impurity loading. This optimized structure is consistent with field emission-scanning electron microscopy (FE-SEM) and HR-TEM observations, which show markedly reduced primary particle size, finely dispersed FeP domains embedded within NFVP-0.15 agglomerates, and distinct lattice fringes assignable to both the NASICON host and the exsolved FeP phase. Such microstructural refinement directly contributes to the enhanced charge transfer characteristics. In EIS measurement, NFVP-0.15 exhibits the lowest charge transfer resistance ($R_{ct} \approx 16$ Ω) compared to $Na_3V_2(PO_4)_3$ (NVP) and other Fe-doped compositions (Fig. 7c). These conductivity improvements directly translate into superior electrochemical behavior as a SIB cathode, achieving an initial discharge capacity of 90 mAh g^{-1} at a 10C rate with only 0.01% capacity decay per cycle over 1000 galvanostatic charge−discharge (GCD) cycles. Moreover, symmetric cells employing NFVP-0.15 exhibited a capacity of 73 mAh g^{-1} at 1C and retained 85% of their capacity after 200 cycles, indicating the effectiveness of the FeP exsolution strategy in achieving superior rate capability and long-term cycling stability (Fig. 7d). Moreover, in situ exsolution of metal particles during electrochemical cycling can further enhance the characteristics of the electrode. Ren et al. demonstrated the critical role of in situ Ag exsolution from $AgBiS_2$ nanocrystal anodes in enhancing the K-ion battery (KIB) performance [130]. The Ag-exsolved electrode delivered a high reversible capacity of 420 mAh g^{-1} at 0.5 A g^{-1}, an excellent rate capability of 210 mAh g^{-1} at 5 A g^{-1}, and long-term cycling stability with 78% capacity retention at 2 A g^{-1} over 300 cycles, surpassing both Bi-based electrodes and previously reported state-of-the-art KIB anodes (Fig. 7e and 7f). Khan *et al.* prepared and investigated perovskite-type $AgNbO_3$ as a negative electrode for Li-ion battery (LIB), focusing on the influence of Ag exsolution on electrochemical behavior [131]. During the first lithiation, a distinct activation process occurs, in which Ag is exsolved from the A-site, inducing A/B non-stoichiometry and enabling partial charge compensation through Li^+ intercalation. Below 0.3 V (vs. Li^+/Li), the material undergoes a crystalline-to-amorphous transition, accompanied by Nb^{5+} reduction to an average oxidation state of Nb^{3+}. At deeper lithiation, reversible Li−Ag nano-(de)alloying further contributes to charge storage. As a result, $AgNbO_3$ delivers a specific capacity of 226 mAh g^{-1} over an extended potential window (0.01−3.0 V), which is approximately 13 times higher than the capacity obtained in its electrochemically stable window (1.2−3.0 V) and 4 times higher than the Nb-redox-active region (0.6−3.0 V) (Fig. 7g). Moreover, the electrode exhibited excellent high-power performance, retaining 72 mAh g^{-1} at 2 A g^{-1}, along with outstanding long-term cycling stability and efficiency, while maintaining stable operation for 2500 cycles at 1 A g^{-1}. In summary, these studies demonstrate that exsolution primarily improves electronic conductivity, facilitates charge transfer, and

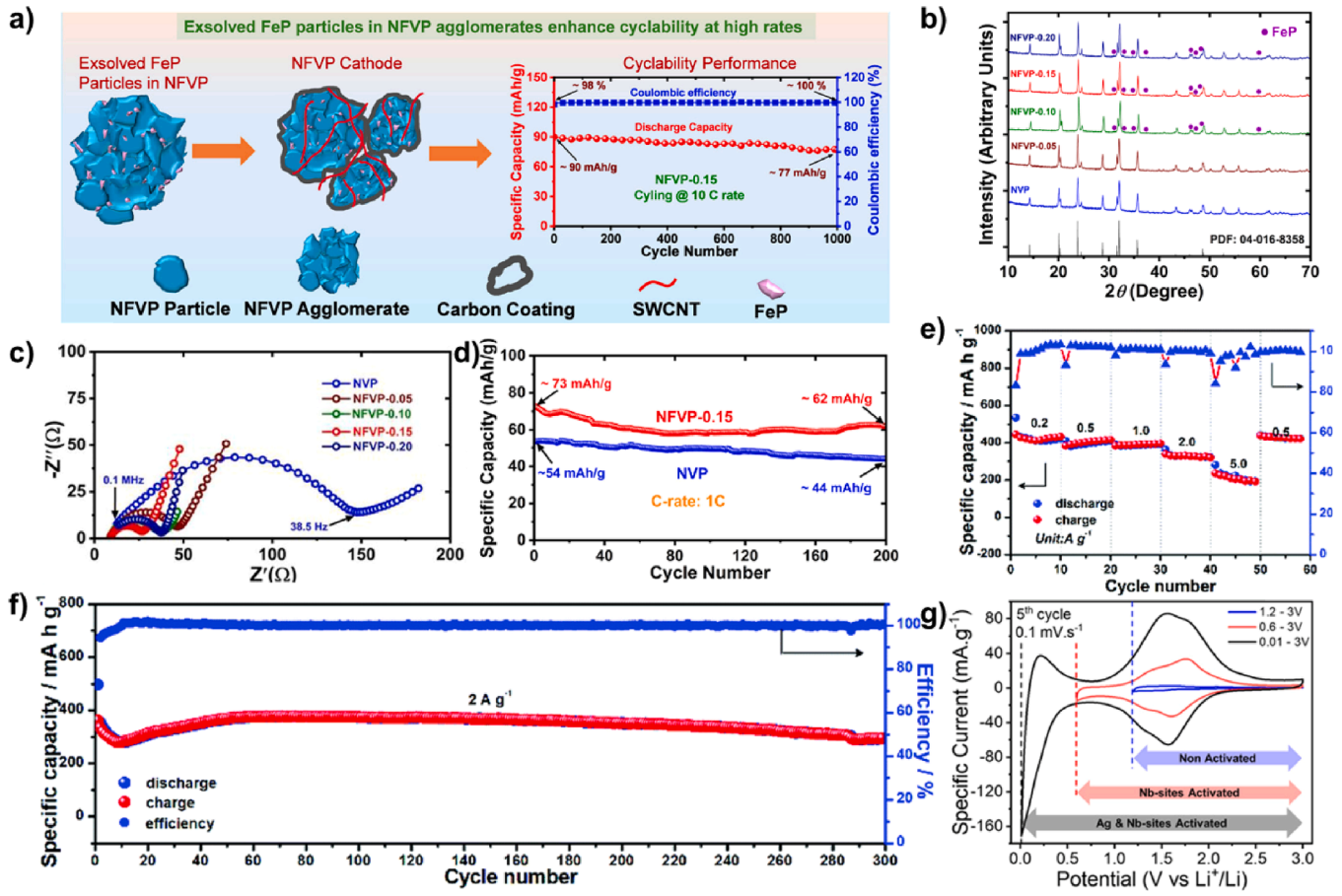

Fig. 7. a) Synthesis strategy of FeP exsolved NASICON-type $Na_3Fe_xV_{2-x}(PO_4)_3$ (NFVP-x) cathodes and cycle performance of NFVP-0.15 at 10C, showing high discharge capacity and nearly 100% coulombic efficiency over 1000 cycles, b) XRD patterns of NFVP-x powders exhibiting FeP-related diffractions, and c) Nyquist plot of half cells and d) cycling stability at 1C of pristine $Na_3V_2(PO_4)_3$ (NVP) and NFVP-0.15 symmetric cells, showing improved rate capability and long-term cycling stability. Reproduced with permission [129]. Copyright 2025, American Chemical Society. e) Rate capability of $AgBi_2$ nanocrystal anodes for K-ion batteries (KIBs) at various current densities and f) cycling performance at 2 A g^{-1}, revealing high reversible capacity, excellent rate performance, and capacity retention over 300 cycles. Reproduced with permission [130]. Copyright 2020, The Royal Society of Chemistry. g) 5th galvanostatic cycle of $AgNbO_3$ at different potential windows (1.2/0.6/0.01−3 V vs. Li^+/Li), showing activating Ag exsolution at low potential enables a wider operating voltage window and significantly higher specific capacity. Reproduced with permission [131]. Copyright 2024, Elsevier.

stabilizes electrode structures, thereby enabling enhanced rate capability and long-term cycling performance for metal-ion batteries.

In contrast, in Li−S batteries which operate via fundamentally different electrochemical mechanisms based on multi-step polysulfide conversion reactions, the key limitations arise from polysulfide dissolution and shuttling, sluggish redox kinetics, and structural degradation of sulfur host materials [53,132]. Despite their exceptionally high theoretical energy density, these issues significantly hinder their practical application. To address these challenges, Hou *et al.* synthesized a novel heterostructure of cobalt nanometals and strontium titanate perovskite by in situ exsolution [133]. The exsolved Co metal can generate abundant catalytically active sites with superior electrocatalytic activity and stability, while simultaneously enhancing the electronic conductivity. Because of the synergy between the adsorption properties and catalytic performance, the heterostructure exhibited remarkable electrochemical performance, delivering a high specific capacity of 793 mAh g^{-1} even at a high current density of 2C, together with an exceptionally low fading rate of 0.047% per cycle over 1000 cycles. These results demonstrate that exsolution effectively enhances electrochemical performance in Li−S battery systems by improving reaction kinetics and cycling stability.

Overall, these results highlight that exsolution serves as a universal design strategy for engineering advanced electrode materials, enabling the formation of strongly anchored metal−oxide interfaces that simultaneously optimize interfacial properties and reaction environments. Regardless of the specific battery chemistry, the introduction of exsolved metal nanophases effectively tailors charge transfer pathways, interfacial stability, and reaction kinetics, thereby addressing critical performance limitations inherent to each system. This versatility underscores the potential of exsolution as a broadly applicable approach for the rational design of next-generation energy storage materials.

3.5. *Others (sensor, etc.)*

In addition to the energy-related applications discussed above, exsolution-based materials have been increasingly employed in a broad range of functional domains. These emerging applications, including biosensing, chemical sensing, and photothermal catalysis, further demonstrate the versatility and broad technological relevance of this exsolution strategy [134–137]. Martin et al. employed the exsolution method to form Pt nanoparticles from undoped and Zr- and Gd-doped CeO_2 matrices to enhance the electrocatalytic performance of microbial fuel cell-based biosensors [138]. Among the evaluated systems, Gd-doped Pt-exsolved CeO_2 exhibited the most favorable nanoparticle characteristics, delivering superior sensitivity and operational stability compared to the other compositions. This integration of exsolution with dopant engineering not only reduces material costs but also improves catalytic durability, offering a promising route toward more sustainable

and high-performance biosensing platforms. For NH_3 sensing applications, Meng *et al.* employed Ag nanoparticle-decorated $NiFe_2O_4$ ($NiFe_2O_4$/Ag) prepared via electrochemical exsolution as a sensing electrode [139]. Upon applying a voltage of −2.0 V to $NiFe_2Ag_{0.05}O_{4.025}$ for 1000 s, a large number of Ag nanoparticles were exsolved onto the surface of $NiFe_2O_4$ and firmly attached to the oxide matrix, thereby forming a highly active second phase that significantly enhanced the sensing performance. The exsolution of Ag nanoparticles significantly enhanced the response and sensitivity of the sensor and reduced the limit of detection (LOD) from 50 to 10 ppm, demonstrating the effectiveness of the exsolution strategy for sensing target elements. Moreover, the $NiFe_2O_4$/Ag sensing electrode exhibited excellent anti-interference capability against CO_2, CH_4, H_2, O_2, and humidity, with a particularly strong selectivity toward NO_x. These results demonstrate that electrochemical exsolution is an effective strategy for producing high-performance sensing electrodes with enhanced sensitivity and selectivity.

In photothermal applications, the lattice strain in metal−oxide catalysts critically influences the catalytic activity of materials because the crystal orientation, exposed facets, and atomic rearrangement are tuned by the lattice strain [140]. However, the rational design of heterojunction catalysts that simultaneously incorporate controlled lattice strain and stable active sites remains a significant challenge. To address this issue, Li et al. synthesized a porous $Ba_{0.9}Ti_{0.9}Ni_{0.1}O_{3-\delta}$ (BTNO) catalyst via a sol−gel method and subsequently constructed a Ni-BTNO metal-semiconductor heterostructure through the in situ exsolution of Ni nanoparticles under photothermal reaction conditions. The Ni-BTNO exhibited high photothermal CO_2 conversion efficiency, achieving CO and CH_4 evolution rates of 40.50 mmol g_{cat}^{-1} $h^{-1}$and 19.62 mmol g_{cat}^{-1} h^{-1}, respectively [141]. This outstanding performance arises from the dual regulation of the lattice strain and Ni exsolution, which collectively modulate the band structure, enhance the photogenerated carrier mobility, and increase both the CO_2 adsorption and oxygen vacancy concentration. The exsolved Ni nanoparticles served as reaction sites and provided a thermodynamically favorable pathway for CH_4 formation, thereby playing a crucial role in boosting the overall catalytic efficiency.

The exsolution strategies have been successfully extended to high-temperature thermocatalytic processes for small-molecule activation, such as steam reforming and dry reforming of methane (DRM), where catalyst deactivation by carbon coking and sintering remains a major hurdle. In these systems, exsolution-derived catalysts create robust metal−oxide interfaces that effectively decouple the reaction pathways. For instance, Liao et al. demonstrated that quinary spinel-derived $NiFeMgAlZnO_x$ catalysts can generate a surface NiFeZn nanoalloy in situ, which facilitates C−C bond cleavage and intermediate oxidation to minimize carbon deposition during ethanol steam reforming [142]. Furthermore, Joo et al. reported that ternary Co−Ni−Fe alloy nanoparticles exsolved from perovskite hosts can tune the surface d-band center to reduce the CH_4 dissociation barrier, thereby enhancing the dry reforming performance while suppressing coke formation [143]. These examples highlight that exsolution provides a versatile design space for tailoring active sites in demanding thermocatalytic environments.

4. Phase tunability of exsolution strategy

4.1. Conventional methods

4.1.1. Fundamentals

Conventional exsolution typically refers to the thermally or electrochemically induced migration of reducible metal cations from the bulk lattice to the surface of a solid matrix. Under reducing or polarizing conditions, oxygen vacancy formation and cation reduction drive the segregation of metallic species that nucleate as anchored nanoparticles [54-56]. The host lattice usually preserves its crystallographic symmetry, and stoichiometric perturbations remain localized. The resulting metals form partially embedded nanostructures with strong metal−-oxide interfacial bonding, affording excellent mechanical and thermal stability [37]. This phase-retaining exsolution is governed mainly by redox thermodynamics and defect-mediated diffusion kinetics. The extent of exsolution depends on the reducibility of the host, the mobility of oxygen vacancies, and the oxygen partial pressure during treatment. As the lattice phase remains unchanged, such systems provide robust immobilization of metal nanoparticles while maintaining the structural integrity of the matrix.

4.1.2. Limitations

Despite its practicality, the conventional route offers limited control over the spatial distribution and size uniformity of exsolved nanoparticles. A globally applied redox environment promotes stochastic nucleation, yielding broad particle-size distributions. The lack of phase flexibility also constrains the defect chemistry, thereby limiting the tunability of the diffusion pathways and interfacial strain, both of which govern the nucleation kinetics.

4.1.3. Phase-retained exsolved materials

Phase-retained materials preserve their crystal structures even after exsolution of the metal component. Strong metal−substrate interactions and minimal morphological disruption ensure durability through repeated redox operations. However, in the absence of structural reconfiguration, the formation of new diffusion pathways and additional heterointerfaces is limited. Consequently, mass transport and nucleation sites remain largely confined to existing lattice routes and interfaces, limiting the ability to finely tune the exsolution kinetics (exsolution rate, nucleation density, and growth behavior). The resulting systems guarantee stability but sacrifice tunability, leaving the phase-mediated effect largely unexploited.

This trade-off motivates the development of phase-tunable exsolution strategies, in which controlled phase transformations are deliberately employed to generate new diffusion pathways, heterointerfaces, and defect environments, thereby enabling more precise control over exsolution kinetics and metal−matrix coupling compared to that in phase-retained oxide hosts.

4.2. Phase-tunable methods

4.2.1. Fundamentals

In phase-tunable exsolution, the crystalline phase of the host lattice is not merely a static framework, but an active variable that dictates how, when, and where exsolved species emerge. As illustrated in Fig. 8, unlike conventional exsolution process, in which the host structure (usually perovskite) remains largely invariant, phase-transformation-coupled exsolution deliberately employs structural and anionic phase transitions, such as the conversion between perovskite and RP structures, reconstruction from spinel to rock salt, and topotactic transformation from an oxide to a nitride or phosphide [144], to initiate and spatially guide the exsolution of reducible metal species. During these transitions, variations in oxygen stoichiometry, lattice strain, and anion chemistry create steep local gradients in the chemical potential [8,145,146]. These gradients act as dynamic nucleation fields, accelerating diffusion and lowering the reduction barrier for cation migration toward the surface. Simultaneously, new interphase boundaries formed between the emerging phases functioned as preferential anchoring sites, promoting the embedded exsolution of the nanosized metal species [147]. Hence, the exsolution process becomes intrinsically phase-selective and self-templated, coupled with the transformation of the host structure, rather than proceeding independently. This coupling can be categorized into two modes. In thermodynamic coupling, the stability field of the transformed phase changes the free energy of reduction, thereby determining the driving force and reducibility of the exsolvable metal species [144]. In kinetic coupling, enhanced defect mobility and boundary diffusion during transformation become

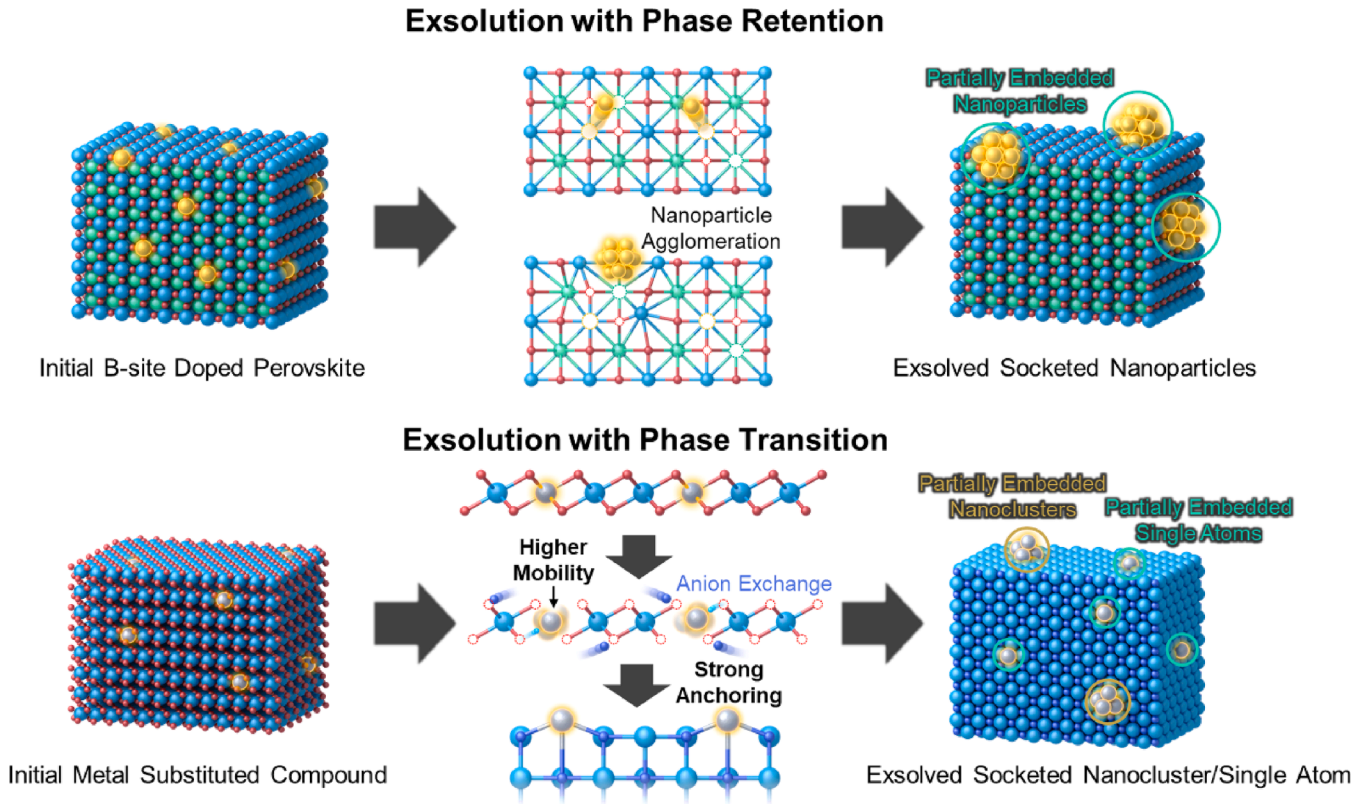

Fig. 8. Schematic illustration of conventional exsolution and phase-tunable exsolution process.

rate-determining, controlling the transport of metal species and the overall exsolution rate [148]. Accordingly, the nucleation, growth, and immobilization of metal species are inseparable from the host lattice reconfiguration, leading to a transformation governed by the exsolution process.

At the microscopic level, these phase transitions reshape cation diffusion pathways, nucleation sites, and lattice strain fields. Nitridation or phosphidation typically lowers the formation energy of anion vacancies and introduces heterogeneous strain around transforming domains, which enhances cation mobility along specific crystallographic directions and at interphase boundaries. As a result, reducible metal ions migrate preferentially toward strained defect-rich regions, where the local chemical potential and elastic energy landscape lower the nucleation barrier and stabilize ultrasmall clusters of single-atom-like configurations that are difficult to realize in typical oxide hosts.

4.2.2. Advantages

The cooperative nature of phase transformation-driven exsolution provides multiple functional benefits over conventional thermal and electrochemical methods, as described below.

1) Site-selective diffusion and nucleation

Phase coexistence generates spatial variations in the defect density and ionic diffusivity within the lattice. Cation migration and reduction occur preferentially at the phase boundaries and interfacial regions, where the strain and vacancy concentrations are maximized [147,148]. Consequently, exsolution is spatially confined to these interfacial regions, enabling nanoscale control over the distribution of catalytically active sites [149]. This defect- and strain-mediated selectivity enables the precise localization of exsolved species at phase boundaries and reconstructed regions, offering a powerful handle to engineer the exsolution rate, nucleation density, and spatial distribution of active sites.

2) Enhanced interfacial coupling and conductivity

Structural distortion and anion exchange (e.g., oxide → nitride or phosphide) increase lattice covalency, strengthen metal−matrix interaction, and improve electron transport across the interface. The formation of heteroanion bonds (such as M−N or M−P) introduces partially delocalized electronic states near the Fermi level, facilitating efficient charge transfer between the exsolved metals and the surrounding matrix [8,145]. Simultaneously, lattice strain and electronic coupling at these reconstructed interfaces reduce the Schottky barrier and enable Ohmic-like contact behavior, which is essential for minimizing interfacial resistance during catalytic or electrochemical reactions [150]. As a result, phase transformation-driven exsolution not only stabilizes nanoparticles mechanically but also electronically integrates them into a continuous conductive network, thereby maximizing both activity and durability. In addition to enhancing charge transport, these reconstructed interfaces accommodate strain and suppress interfacial delamination, thereby improving the mechanical robustness of phase-tunable exsolved nanoparticles under electrochemical cycling.

3) Compositional selectivity

Distinct crystalline phases exhibit different thermodynamic reduction potentials and cation solubilities, which determine the metallic species that are preferentially exsolved during transformation [66,79,144]. For example, during oxide-to-phosphide or oxide-to-nitride conversion, the altered local chemical environment selectively stabilizes specific transition metal cations in reduced states, whereas others remain lattice-bound [151]. This phase-dependent redox hierarchy enables the selective exsolution of the target metals or the formation of bimetallic nanoparticles with controlled stoichiometry. Moreover, the differences in ionic radii and electronegativities between the transformed phases modulate the local chemical potential, resulting in element-selective diffusion kinetics [145]. In systems such as phosphidated or nitridated oxides, these effects can be tuned to induce the emergence of a single component (e.g., Fe-rich vs. Co-rich domains), allowing the deliberate construction of compositionally asymmetric interfaces that enhance catalytic selectivity.

4) Functional versatility

Phase modulation simultaneously influences multiple physicochemical parameters, including electronic conductivity, band alignment, defect concentration, and surface energy. Structural and anionic transformations alter the density of states (DOS) near the Fermi level, shift the work function, and rearrange the local coordination environments, which collectively govern the catalytic activity and reaction selectivity [98,147]. In oxide-to-nitride or oxide-to-phosphide conversions, increased lattice covalency enhances carrier mobility, whereas partial reduction during transformation introduces conductive subbands that facilitate electron transfer across the entire hybrid framework. Moreover, the coexistence of distinct crystalline phases can induce microstructural features, such as grain boundaries, dislocations, and local lattice disorder, which may serve as additional diffusion channels and active nucleation sites. These interfacial imperfections also facilitate mass and charge transport and can contribute to the improved strain tolerance of the matrix, mitigating stress accumulation during redox cycling [152]. Consequently, phase-tunable exsolutions offer a versatile platform for optimizing the functional performance across diverse energy applications, from electrocatalysis to photochemical conversion and ion storage.

4.2.3. *Phase-tuned exsolved materials*

Phase-tuned systems operate as multiphase hybrids, where modification of the host and exsolution of metal species occur cooperatively. Designed phase heterogeneity, achieved through structural reconstruction (perovskite ↔ RP, spinel ↔ rocksalt), serves as an internal interface that dictates the diffusion pathway and final exsolution of nanoparticles. For instance, structural phase transitions within the perovskite or spinel lattices generate interphase boundaries that act as nucleation centers, leading to embedded nanoclusters stabilized by the surrounding lattice strain field [147]. These phase-engineered hybrids exhibit improved activity, conductivity, and durability. The phase boundaries provided efficient electron highways, whereas the embedded configuration suppressed agglomeration under harsh electrochemical conditions. Fine-tuning the transformation sequence further allows the integration of charge transport, active sites, and stability functions within a single architecture. Therefore, phase transformation-coupled exsolution represents a paradigm shift from considering exsolution as a static reduction phenomenon to designing it as a systematic, multistage synthesis strategy governed by the dynamics of the phase evolution itself.

4.3. *Phase-transformation-coupled exsolution*

Phase-transformation-coupled exsolutions have recently emerged as an effective route for integrating lattice restructuring, anion exchange, and metal emergence within a single synthetic framework [42,43,57] In contrast to phase-retained oxide hosts, in which exsolution proceeds in a crystallographically rigid environment, these systems deliberately exploit structural rearrangements and anion substitution to create defect-rich conductive matrices that actively guide the outward migration and anchoring of metal species. In many cases, oxide or hydroxide precursors are converted into nitrides, phosphides, or sulfides, whereas the doped metal species migrate outward and form strongly bound clusters, nanoparticles, or even single-atom sites within the transforming matrix. This cooperative evolution of the host and metal produces hybrid architectures that are difficult to access using conventional loading or simple thermal reduction alone.

For oxide systems, a recent study on a medium-entropy Sr−Fe−Co−Ni−Cu−Mo perovskite fuel electrode showed that in situ exsolution of Fe−Co−Ni−Cu quaternary alloy nanoparticles is tightly coupled to a double-to-layered perovskite phase transformation, generating oxygen-vacancy-rich alloy–oxide interfaces that markedly enhance CO_2−CO mutual conversion kinetics and long-term reversible solid oxide cell durability [153].

A representative example of nitridation-driven exsolution was reported by Yun et al., who designed Ru−TiN nanotubes via the ammonolysis of Ru-substituted TiO_2 nanowires, as illustrated in Fig. 9a [43]. During high-temperature NH_3 treatment, the TiO_2 lattice was converted into conductive TiN, while Ru ions within the oxide framework migrated outward and were reduced to metallic Ru nanostructures embedded in the nitride matrix. The substitution of oxygen with nitrogen generated abundant anion vacancies and local strain, which facilitated Ru diffusion toward the surface and created favorable interfacial sites for anchoring. Consequently, the exsolved Ru−TiN nanotubes exhibited much lower overpotentials and smaller Tafel slopes for the HER than both Ru-free TiN and Ru-deposited homologues, together with markedly reduced charge-transfer resistance and negligible nanoparticle agglomeration during long-term electrolysis (Fig. 9b). This study illustrates how nitridation and exsolution can be combined to produce a highly conductive host with strongly coupled metal sites. A related but more compositionally versatile concept was introduced by Sun et al., who explored the pnictogenation-driven exsolution of multimetallic layered double hydroxide (LDH) precursors. Conductive nitride and phosphide matrices containing size-tunable Ru species were obtained by treating Ru-substituted Ni−Fe hydroxides under nitriding and phosphide atmospheres, respectively [57]. In the nitrogen-substituted products, Ru was mainly present as ultrasmall nanoclusters embedded within a metal nitride framework, whereas phosphidation yielded Ru species that were atomically stabilized at the metal phosphide interfaces with distinct local coordination and electronic structures. A systematic comparison of the HER activity revealed that both nitridation- and phosphidation-driven exsolutions significantly outperformed their conventional Ru-deposited counterparts, owing to the combination of highly conductive pnictogenide hosts, strong metal−matrix electronic coupling, and tailored Ru coordination environments. These results demonstrate that the choice of pnictogen not only determines the phase and conductivity of the matrix but also influences the size and chemical state of the exsolved Ru species, offering an additional handle for tuning the catalytic properties. Li et al. further refined this concept by constructing a Ru-doped Ni_2P/Fe_3P heterostructure through the phosphidation of Ni−Fe hydroxide precursors (Fig. 9c) [44]. In this system, the Ni_2P−Fe_3P heterointerface was preserved after phosphidation, whereas the Ru atoms were stabilized at the interfacial positions without forming separate Ru nanoparticles. High-resolution electron microscopy and elemental mapping confirmed homogeneous dispersion of Ru at the heterostructure surface, and DFT calculations identified specific Ru sites at the interface as the most active centers for hydrogen adsorption, with nearly thermoneutral ΔG_{H^*} values. The resulting Ru−Ni_2P/Fe_3P catalyst showed low overpotentials and small Tafel slopes in the alkaline HER, together with excellent durability over extended operations (Fig. 9d). This study highlights that the phosphidation-driven exsolution or redistribution of Ru can be exploited not only to form metallic clusters but also to stabilize single-atom-like configurations at conductive phosphide interfaces. Synergistic exsolution and phosphidation have also been applied to oxide frameworks in addition to LDH-derived systems. Kim et al. devised a one-pot process in which multimetallic tungstate precursors were treated with a solid phosphorus source to produce P-rich tungsten oxide matrices decorated with amorphous (Ir, Ru) phosphide nanoparticles [154]. Under phosphidation conditions, the partial reduction and restructuring of the WO_3 lattice occurred concurrently with P incorporation and outward migration of Ir and Ru, leading to exsolved (Ir, Ru)P_x domains that remained strongly coupled to the conductive W−O−P framework. Operando characterization and theoretical analysis indicated that the modified bonding environment and increased covalency of M−P linkages lowered the energy barrier for water dissociation and optimized hydrogen adsorption at the metal−phosphide−oxide junctions, resulting in higher mass activity and improved stability compared with conventional Ir- or Ru-based catalysts.

Phase-transformation-coupled exsolution is not limited to electrocatalysts for the HER; sulfidation-based routes provide additional examples in which anion exchange and metal emergence proceed together

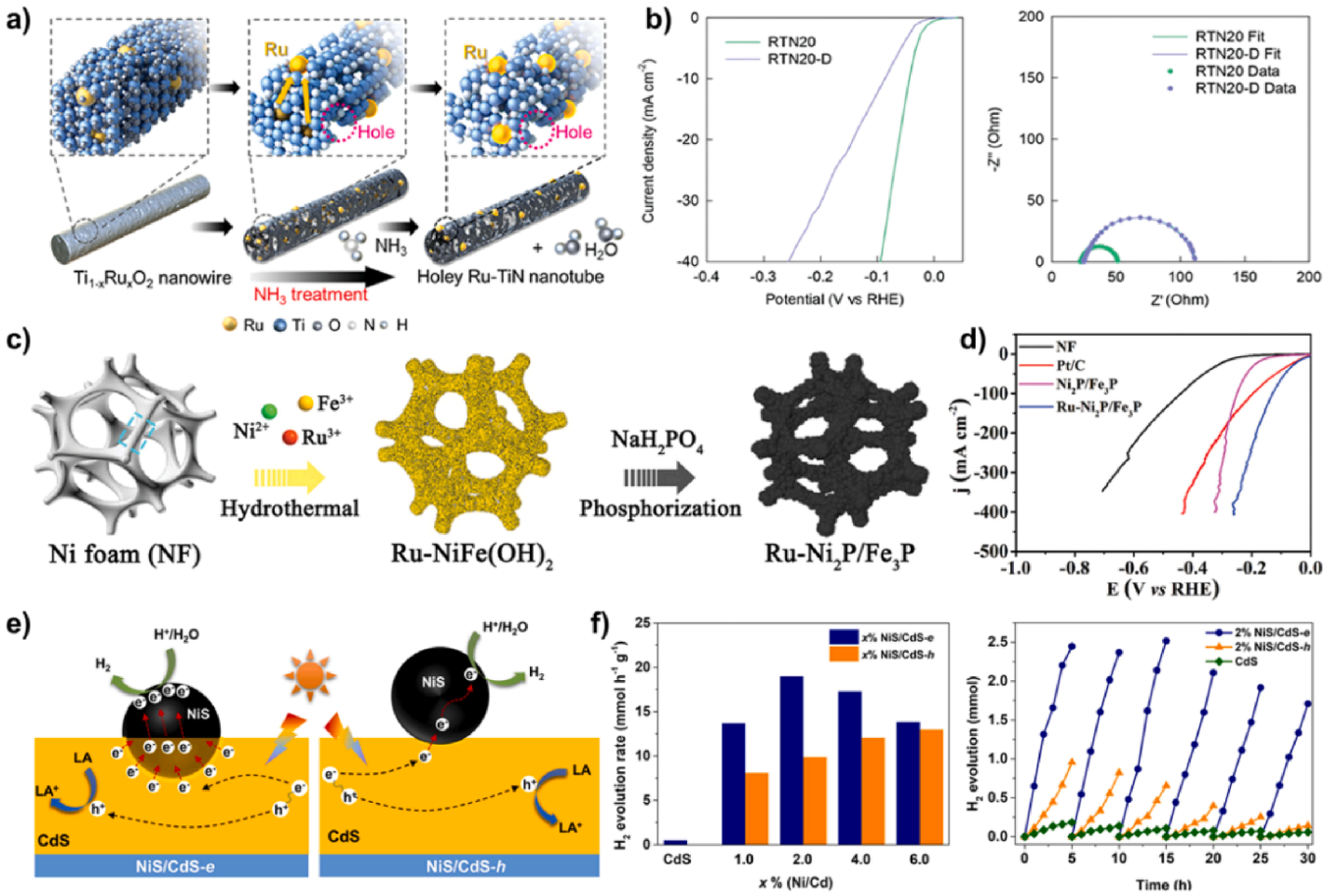

Fig. 9. a) Schematic illustration of nitridation-driven exsolution of Ru nanostructures to form holey Ru−TiN nanotubes from Ru-substituted TiO_2 nanowires, b) LSV and EIS results of Ru−TiN catalyst for HER in acidic electrolyte. Reproduced with permission [43]. Copyright 2024, Wiley-VCH. c) Synthetic route for preparing Ru-doped Ni_2P/Fe_3P heterostructures via phosphidation of Ru−NiFe(OH)$_2$, d) HER polarization curves of Ni foam, Pt/C, Ni_2P/Fe_3P, and Ru−Ni_2P/Fe_3P catalysts in alkaline media. Reproduced with permission [44]. Copyright 2024, Wiley-VCH. e) Comparative diagram of NiS-exsolved CdS (NiS/CdS-e) NiS-deposited CdS (NiS/CdS-h) photocatalysts obtained by hydrothermal sulfidation of Ni-doped Cd(OH)$_2$, and f) photocatalytic H_2 evolution rates and time-dependent profiles under visible light for CdS, NiS/CdS-h, and NiS/CdS-e. Reproduced with permission [155]. Copyright 2023, Elsevier.

to create strongly bound cocatalysts for photocatalysis. Li et al. prepared Ni-doped Cd(OH)$_2$ and subjected it to hydrothermal sulfidation to obtain CdS decorated with partially embedded NiS nanoparticles [155]. During this process, the hydroxide-to-sulfide transformation created sulfur-rich domains that promoted the nucleation and anchoring of NiS at the CdS surface, forming a "socketed" configuration (Fig. 9e). The exsolved NiS/CdS-e photocatalyst delivered a hydrogen evolution rate far exceeding those of both pristine CdS and the samples prepared by simple NiS impregnation (NiS/CdS-h), with a significantly higher apparent quantum efficiency under visible light (Fig. 9f). A detailed analysis attributed this enhancement to the intimate NiS−CdS interface generated during sulfidation, which promoted charge separation, suppressed charge recombination, and provided abundant surface sites for proton reduction. More broadly, anion-exchange-driven transformations, including nitridation, phosphidation, and sulfidation, indicate that similar mechanisms may be transferred to a wider range of oxide and hydroxide hosts. Because these reactions often generate vacancy-rich domains and mixed-anion interfaces, they can, in principle, provide additional pathways for controlled exsolution in systems beyond those reported to date. Beyond anion-exchange-driven conversions, several studies have demonstrated that the chemically induced restructuring of oxide hosts can also be coupled with exsolution to generate strongly anchored metal species. For instance, high-valence cation doping in perovskite oxides triggers surface rearrangement and oxygen vacancy enrichment, thereby creating a chemically softened surface layer that promotes outward cation migration and the formation of embedded metal nanoparticles during reduction [156].

As presented in Fig. 10a, a complementary mechanism was observed in Ru-doped MnO_2 nanowires, where C_2H_2-driven reduction converted MnO_2 to MnO while simultaneously producing an in situ carbon overlayer. This reductive phase conversion created locally reduced domains that facilitated Ru exsolution and stabilized the resulting metal−matrix interfaces [42]. The Ru-exsolved MnO@C catalysts showed superior HER activity and charge transfer kinetics in acidic electrolyte over Ru-free MnO@C, as shown in Fig. 10b. These examples highlight the fact that structural or chemical reconstruction, distinct from anion exchange, can also provide energetically favorable pathways for controlled metal emergence during transformation, broadening the design landscape of transformation-coupled exsolution. Structural phase reconstruction coupled with exsolution has also been explored for oxide frameworks without anion substitution.

For example, Ir-doped $Y_2Ru_2O_7$ pyrochlore catalysts (YRIO) generate RuIr nanoparticles under reducing conditions, accompanied by partial reconstruction of the pyrochlore lattice toward Y-oxide-rich domains [157]. XRD patterns in Fig. 10c demonstrated exsolution of metallic RuIr and partial formation of Y_2O_3 host lattice. The exsolved catalysts showed excellent HER activity (higher than commercial Pt/C catalyst) and electrochemical stability over 120 h (Fig. 10d). In this system, the formation of oxygen vacancies and the local rearrangement of the Ru−O network create pathways for Ir and Ru migration, whereas the emerging heterointerfaces between metallic RuIr and the reconstructed oxide provide robust anchoring sites. The resulting materials exhibited high

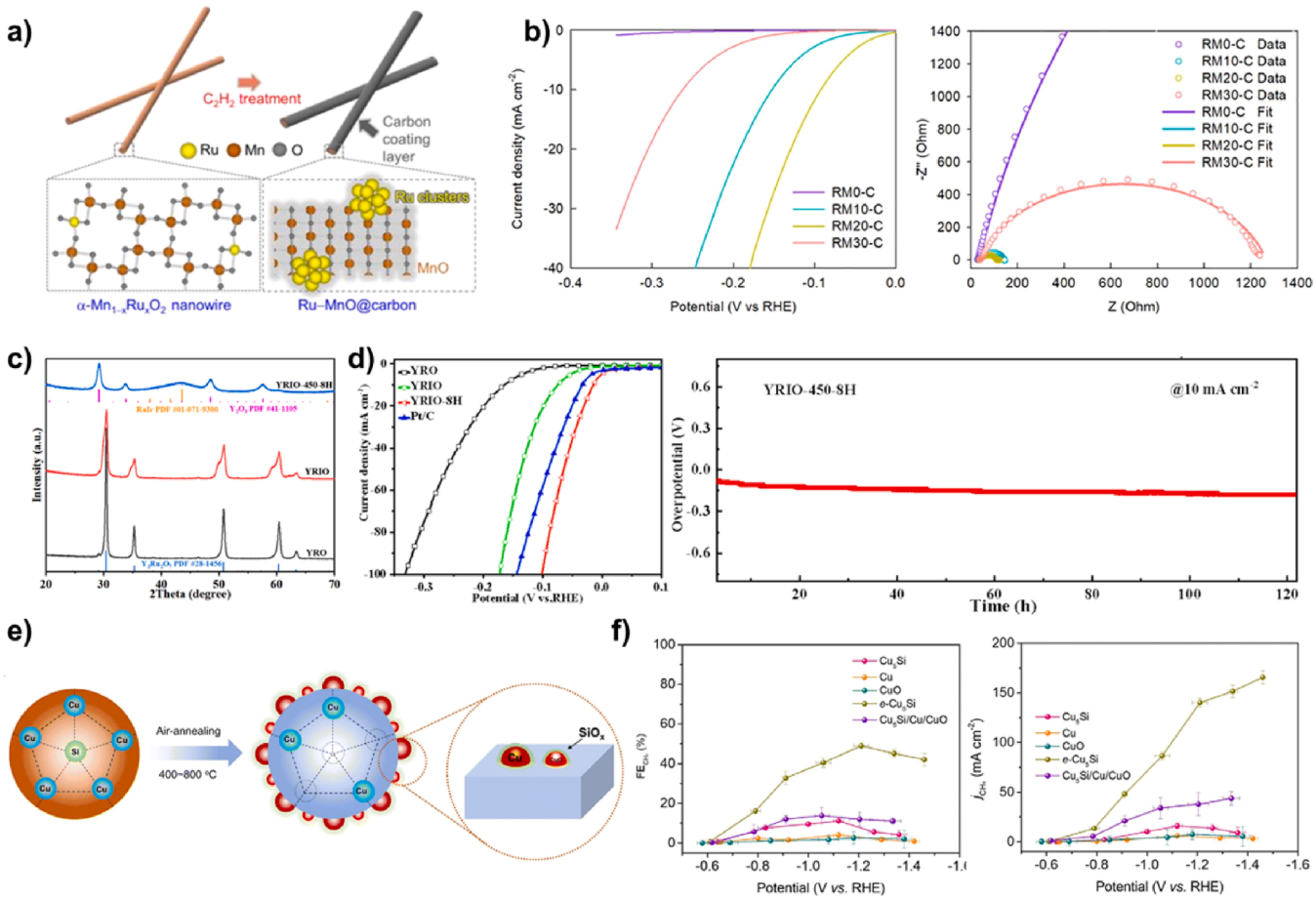

Fig. 10. a) Synthetic routes for preparing Ru−MnO@C nanowire by C_2H_2 treatment of Ru-doped MnO_2. b) Electrochemical measurement results of Ru−MnO@C catalysts in acidic media. Reproduced with permission [42]. Copyright 2022, Elsevier. c) XRD patterns of Ir-doped $Y_2Ru_2O_7$ (YRIO) before and after reduction. d) Electrochemical HER performance and long-term stability of RuIr/Y_2O_3 catalysts. Reproduced with permission [157]. Copyright 2025, Elsevier. e) Schematic illustration of air-annealing-induced exsolution process of Cu−Si intermetallic compound to form Cu/CuO−SiO_x surface. f) Electrochemical CO_2RR performance and Faradaic efficiencies of catalysts for CH_4 production. Reproduced with permission [158]. Copyright 2024, The Royal Society of Chemistry.

HER activity and favorable charge-transfer characteristics, illustrating that even pure structural transformations within oxide lattices can create conditions conducive to controlled exsolution and stable metal−oxide junctions. Different types of transformation-assisted exsolutions have been reported for intermetallic- and carbonate-based systems relevant to CO_2 electroreduction. Zhang et al. demonstrated that air annealing of Cu_5Si leads to its partial conversion into $Cu_{6.69}Si$ and concurrent exsolution of the Cu/CuO species together with amorphous SiO_x at the surface, as illustrated in Fig. 10e [158]. In situ high-temperature XRD showed a progressive rearrangement of the Cu−Si lattice and the appearance of metallic Cu and CuO reflections as the annealing temperature increased, indicating that lattice decomposition and metal emergence were tightly coupled. The exsolved Cu/CuO nanoparticles, stabilized by an amorphous SiO_x layer and multiphase interfacial interactions, provided highly active and selective sites for CO_2 reduction to CH_4, with suppressed hydrogen evolution and enhanced methane Faradaic efficiency compared with unsupported Cu or CuO (Fig. 10f). The interfacial environment stabilized Cu^* species and increased *CO coverage, underlining the critical role of exsolution-generated multiphase boundaries in steering product selectivity. Dynamic exsolution behavior was also observed in carbonate-based $CaCO_3$ systems, in which Cu nanoclusters were generated and rearranged under the reaction conditions. In a recent study, in situ-formed Cu^0/Cu^+ pair sites on $CaCO_3$ were identified as highly active centers for CO_2 reduction, with exsolved Cu nanoclusters evolving from the bulk during thermal or electrochemical treatments [91]. The carbonate host undergoes partial decomposition and reconstruction, creating local environments that stabilize specific Cu oxidation states and pair configurations. This example highlights that phase-transformation-coupled exsolution is not confined to oxide-to-pnictogenide or oxide-to-sulfide conversions; it can also occur in carbonate and intermetallic systems, where decomposition and recrystallization generate new metal−support interfaces with tailored electronic structures.

Taken together, these nitridation-, phosphidation-, sulfidation-, and reconstruction-based studies revealed several common design principles for phase-transformation-coupled exsolution. First, the transformation step, driven by nitridation, phosphidation, sulfidation, or structural rearrangement, creates defect-rich regions such as anion vacancies, dislocation networks, and interphase boundaries, which facilitate metal ion migration and serve as preferred nucleation zones for emerging metal species [147]. Second, the resulting nitride, phosphide, or sulfide matrices generally exhibit higher electronic conductivity and stronger metal−matrix covalency than their oxide precursors, leading to improved charge transport and more stable metal anchoring during operation [42,43,57]. Third, phase-transformation-coupled exsolution often enables finer control over the size, dispersion, and coordination of the active metal species, from deeply embedded nanoclusters to interfacial single-atom sites, thereby allowing the catalytic activity and selectivity to be adjusted by tuning the transformation conditions [42,43,57]. Finally, these systems consistently exhibit enhanced functional robustness, maintaining their structural integrity and performance over

extended electrocatalytic or photocatalytic operations because of the strong chemical and electronic coupling at the metal−matrix interfaces created during the transformation.

Overall, phase transformation-coupled exsolution transforms exsolution from a simple reduction-driven surface migration process into a broader synthetic strategy, in which host conversion, defect generation, and metal emergence are tightly interconnected. By tailoring the precursor composition and transformation atmosphere, it is possible to design conductive nitrides, phosphides, sulfides, or reconstructed oxide matrices that not only host exsolved metals but also actively shape their electronic structure and catalytic behavior. Unlike many phase-retained oxide systems, where exsolution can be repeatedly switched on and off through redox cycling to exploit self-regeneration, phase-transform-coupled architectures are typically established during an initial transformation step and then operated within a structurally fixed state. Their stability is therefore attributed mainly to robust socketed metal sites and mechanically and electronically resilient matrices rather than to fully reversible phase switching, although partial reversibility can arise in structurally flexible hosts. Across nitridation-, phosphidation-, sulfidation-, and reconstruction-based systems, numerous studies have already demonstrated that such exsolution-derived architectures exhibit markedly higher operational stability than their conventionally deposited counterparts, maintaining nanoscale dispersion and activity under harsh reaction environments, including photochemical, electrochemical, and thermal conditions.

Nevertheless, a more quantitative understanding of how these structures slowly evolve under extended cycling, including the extent of particle coarsening, local amorphization, or relaxation of engineered strain field, would be valuable for establishing design rules and defining realistic durability and partial reversibility limits under device-relevant conditions.

5. Specialized characterization techniques for exsolve materials

5.1. Electron microscopic analyses

To elucidate the morphological and structural signatures that arise during metal exsolution, it is essential to directly visualize the formation of surface nanoparticles and the accompanying reconstruction of the host lattice. In phase-tunable exsolution systems, such as those undergoing nitridation, phosphidation, or sulfidation, electron microscopy is particularly powerful because it can simultaneously resolve the nucleation of metal species and the phase transformation of the surrounding matrix. Electron microscopy provides an effective analytical tool by offering nanoscale spatial resolution that cannot be achieved by bulk-averaged techniques. In this context, SEM and TEM have been widely employed to examine particle emergence, dispersion, and overall morphological evolution. SEM provided images of exsolved materials, demonstrating partially embedded particles and the host lattice. HR-TEM enables the atomically resolved imaging of lattice fringes, strain fields, and interfacial coherency, providing critical insights into the epitaxial relationships and defect-driven mechanisms that govern nanoparticle nucleation and anchoring. Complementarily, EDS of SEM/TEM offers precise elemental mapping and compositional profiling at the particle−substrate interfaces, revealing the migration pathways and local chemical heterogeneities associated with exsolution. These electron microscopy techniques therefore provide a comprehensive framework for understanding how exsolved nanoparticles form, evolve, and interact with their supporting matrices in both conventional oxide hosts and phase-transformation-coupled systems. Several studies have employed electron microscopy to elucidate the morphology and lattice coupling of exsolved nanoparticles, such as Ru nanocatalysts exsolution via pnictogenation of Ru-substituted $Ni_2Fe_{1-x}Ru_x$-LDH [57], La−Sr−Ni−$TiO_{3-\delta}$ with nanoparticle exsolution [147], Pd nanoparticles socketed on $La_xAl_{0.9}Pd_{0.1}O_{3-\delta}$ perovskite supports [159], Ni nanoparticles exsolved from A-site-deficient layered double perovskites [160], Ce and Ni co-doped double $PrBaMn_2O_5$ perovskite, and Cu nanoparticles exsolved on $La_{1.568}Sr_{0.392}Ce_{0.04}NiCu_xO_{4-\delta}$ [161].

For example, Sun et al. used HR-TEM and scanning transmission electron microscopy (STEM) imaging (Fig. 11a) to compare the phosphidation-driven and nitridation-driven exsolution of Ru atoms from the Ni−Fe-LDH host, showing that pnictogenation yields highly dispersed, size-tunable Ru species ranging from isolated single atoms to nanoclusters uniformly anchored on conductive metal pnictogenide matrices (Fig. 11b) [57]. Electron microscopic observations of the particle size, dispersion, and anchoring geometry complemented in situ X-ray absorption spectroscopy (XAS) results, demonstrating that single-atom-dominated exsolved structures provide more efficient interfacial electronic coupling and superior HER performance than their nanocluster-rich counterparts. This case shows that, even with the same Ru-substituted Ni−Fe-LDH precursor, inducing exsolution via phosphidation or nitridation produces markedly different Ru dispersions and interfacial geometries, directly visualizing how phase-tunable exsolution modulates the metal−support interface. Yu et al. also used HR-TEM (Fig. 11c−f) and STEM imaging to investigate the exsolution of socketed Pd nanoparticles from $La_xAl_{0.9}Pd_{0.1}O_{3-\delta}$ (L_xAPO) perovskites, revealing that controlled thermal treatment produces uniformly distributed Pd nanoparticles tightly anchored within semi-embedded interfacial geometries [159]. These electron microscopy observations of the particle shape, depth of socketing, and interfacial coherence directly support the enhanced thermal stability and catalytic durability of the exsolved Pd species, complementing the structural and surface analyses that highlight the superiority of socketed Pd nanoparticles over their surface-deposited counterparts.

5.2. Spectroscopic analyses

Understanding exsolution requires detailed knowledge of the evolution of lattice vibrations, surface chemical states, oxidation-state transitions, and defect populations as cations migrate and nucleate into metallic species. This is especially true for phase-tunable exsolution, where nitridation, phosphidation, or sulfidation simultaneously alter the anion framework and drive metal emergence. To capture these electronic and chemical signatures that define the progression of exsolution, spectroscopic techniques such as XAS, Raman spectroscopy, X-ray photoelectron spectroscopy (XPS), and electron paramagnetic resonance (EPR) are indispensable. By probing the vibrational modes, surface bonding environments, local coordination structures, and paramagnetic defect centers, these methods collectively reveal how lattice distortion, oxygen vacancy formation, and redox processes occur during exsolution and ultimately shape the functional properties of the resulting materials. Exsolution reshapes the local electronic structure and coordination environment of both the migrating cations and the host lattice. XAS captures these changes with element-specific sensitivity, allowing oxidation-state variations, white-line intensity shifts, and alterations in nearest-neighbor bonding to be monitored during exsolution [162]. XAS is typically divided into X-ray absorption near-edge structure (XANES), which probes the oxidation states and unoccupied electronic configurations, and extended X-ray absorption fine structure (EXAFS), which resolves the local coordination geometry and bond distances. Together, these complementary regimes offer essential insight into how electronic redistribution and short-range structural evolution govern the emergence and catalytic activity of exsolved metal species. These capabilities have enabled the wide application across exsolution systems, including Ru-embedded TiN derived from the ammonolysis of Ru-substituted TiO_2 nanowires [43], Ru−MnO@C nanowires [42], Ru-exsolved $Ni_2Fe_{1-x}Ru_x$ pnictogenides [57], Ru-exsolved fluorite-type $Sm_2Ru_xCe_{2-x}O_7$ solid solutions [13], and Ni-exsolved YSZ composites [163].

Yun et al. employed XANES and EXAFS to investigate the electronic restructuring that accompanies Ru exsolution into a TiN matrix (RTN) derived from Ru-substituted TiO_2 (RTO) nanowires [43]. The Ru K-edge

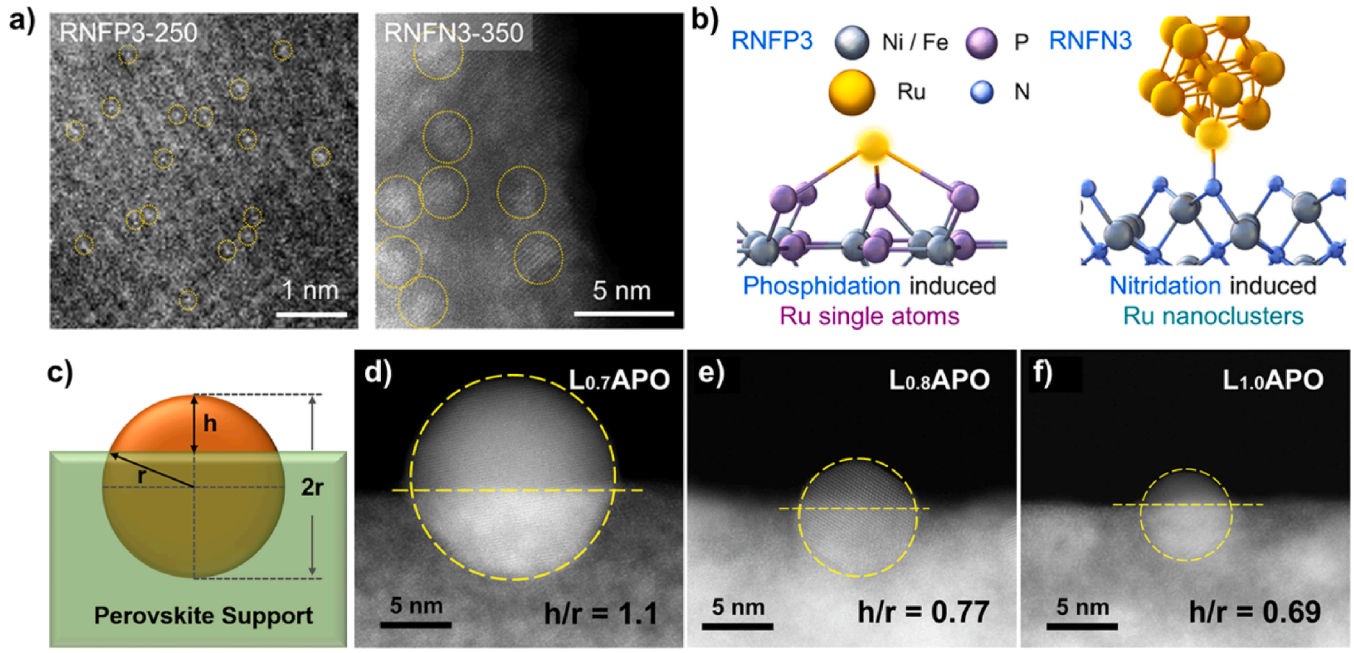

Fig. 11. a) STEM images of Ru single atom exsolved Ni_2P/Fe_2P (RNFP) and Ru nanocluster exsolved Ni_3N/Fe_3N (RNFN), showing the contrast between atomically dispersed Ru sites and nanoscale Ru aggregates, b) schematic illustration of single atom RNFP and nanocluster RNFN. Reproduced with permission [57]. Copyright 2025, Wiley-VCH. c) Geometric model of the socketed configuration of Pd nanoparticles in $La_xAl_{0.9}Pd_{0.1}O_{3-\delta}$ (L_xAPO) perovskites, and d–f) TEM images of L_xAPO after air calcination at 1000 °C for 120 min, highlighting the composition-dependent variation in Pd socketing depth (h/r). Reproduced with permission [159]. Copyright 2024, Springer Nature.

exhibited a distinct shift toward lower energies relative to the Ru^{4+} standards, indicating the partial reduction of Ru during nanoparticle formation (Fig. 12a). EXAFS analysis further revealed the loss of Ru–O coordination from the parent oxide framework and the emergence of Ru–Ru scattering at ~2.4 Å, together with strengthened Ru–N coordination characteristic of the TiN host (Fig. 12b). These spectroscopic signatures confirmed the formation of metallic Ru nanoparticles embedded within the nitride lattice and clarified how the reorganized local bonding environment contributed to the enhanced catalytic performance of the exsolved Ru–TiN system. These XANES/EXAFS features demonstrate that nitridation-induced transformation from TiO_2 to TiN is directly coupled to Ru exsolution, highlighting the suitability of XAS for probing phase-tunable exsolution in oxide-to-nitride systems. In addition, Yun et al. employed Ru K-edge XANES to analyze the Ru–MnO@C system, revealing a clear shift of the Ru K-edge toward a lower energy relative to the Ru^{4+} reference, indicative of the partial reduction of Ru during nanoparticle formation [42]. EXAFS fitting further showed a decrease in Ru–O coordination and the development of Ru–Ru coordination at ~2.2 Å, confirming the formation of metallic Ru clusters and the associated adjustment of local bonding environments within the MnO–carbon framework.

Additionally, exsolution involves changes in lattice vibrations and local symmetry as cations migrate and new surface species are formed. Raman spectroscopy is well-suited for capturing these variations, providing direct signatures of octahedral distortion, oxygen vacancy formation, and the appearance of intermediates [164]. Through these vibrational fingerprints, Raman spectroscopy enables rapid assessment of how the host lattice and surface chemistry evolve during exsolution, both under static conditions and in real-time environments. These advantages have led to their use in a wide range of exsolution systems, including $Gd_{0.2-x}Ni_xCe_{0.8}O_{2-\delta}$ [165], Ni–Sr_2Fe/Mo oxides [166], $PrBaMn_2O_{5+\delta}$ [167], and $FeNi_3$–$CaTiO_3$ [168], demonstrating their broad applicability in tracking exsolution-driven structural evolution. For example, Tan et al. applied Raman spectroscopy to Ni:Gd co-doped CeO_2 ($Gd_{0.195}Ni_{0.05}Ce_{0.8}O_{2-\delta}$, GNDC5) (Fig. 12c) to monitor the vibrational evolution during thermal treatment associated with Ni exsolution [165]. Pristine GNDC5 exhibited a strong F_{2g} mode at ~460 cm^{-1}, characteristic of the cubic fluorite CeO_2 lattice, along with broad defect-related bands in the 550–600 cm^{-1} region arising from oxygen vacancies. Upon increasing the air-annealing temperature, the F_{2g} mode gradually blue-shifted, whereas the vacancy-related sub-bands at ~560 cm^{-1} (extrinsic vacancies) and ~610 cm^{-1} (intrinsic vacancies) were significantly attenuated. Quantitative analysis using normalized peak-area ratios confirmed that both extrinsic and intrinsic oxygen vacancy concentrations decreased with increasing annealing temperature. By contrast, Gd co-doped CeO_2 without Ni doping showed no variation in the F_{2g} or extrinsic vacancy bands, demonstrating that these changes originated from the substitutional Ni doping and its subsequent dissolution at elevated temperatures. As another widely adopted technique for characterizing exsolution-driven materials, XPS offers unique advantages for probing the oxidation states, cation reduction pathways, oxygen vacancy formation, and surface reconstruction occurring during nanoparticle emergence. Guo et al. analyzed the surface chemical evolution of FeNi/$NiFe_2O_4$ (FeNi/NFO) composites during reduction using XPS (Fig. 12d–f), revealing the emergence of metallic Fe^0 (Fe $2p_{3/2}$ at ~707.3 eV), an increased Fe^{2+}/Fe^{3+} ratio, and the appearance of metallic Ni^0 at ~852.7 eV, together with a systematic increase in the defect oxygen component (O 1s at ~531.5 eV), confirming reduction-driven metal exsolution and oxygen vacancy formation [169]. Han et al. examined B-site metal exsolution in $La_{0.6}Sr_{0.4}Fe_{0.8}Ni_{0.2}O_{3-\delta}$ (LSFN) perovskite oxides and observed a pronounced change in the O 1s XPS spectra (Fig. 12g and 12h), where the surface oxygen component (531.8 eV) increased relative to the lattice oxygen peak (529.8 eV). The fraction of surface oxygen species increased from 57% to 74% after H_2/Ar treatment, indicating that B-site metal exsolution generated additional surface oxygen vacancies, which promoted lattice oxygen participation in the alkaline OER [170]. Similarly, Wang et al. utilized XPS to verify the formation of in situ exsolved CoFe alloy nanoparticles, detecting the appearance of metallic Co^0 (778.1 eV) and Fe^0 (706.7 eV) together with a pronounced increase in oxygen-vacancy-related O 1s components at ~530.7 eV, which collectively confirmed the reductive exsolution pathway during anodic operation [171]. Several other XPS

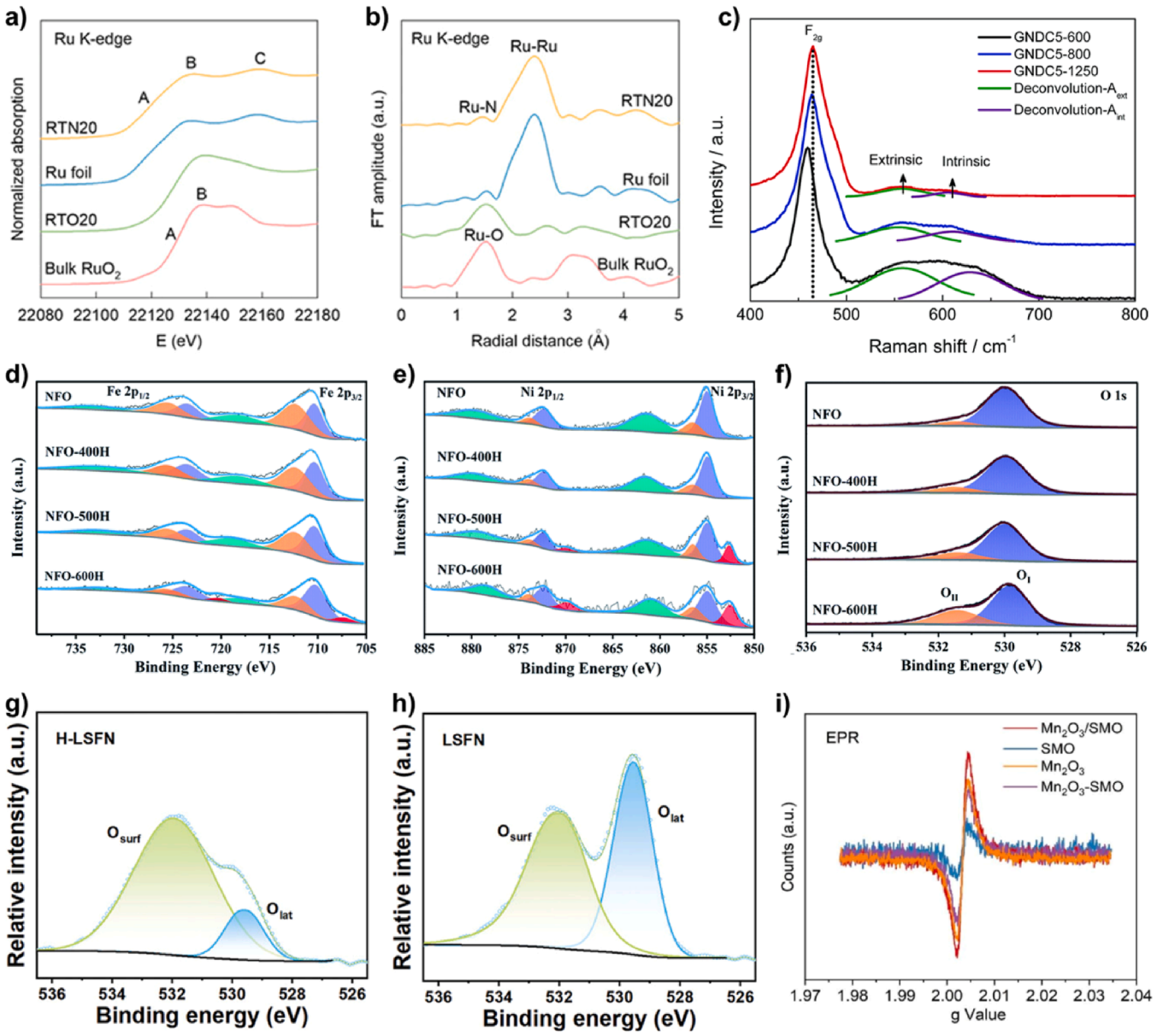

Fig. 12. a) Ru K-edge X-ray absorption near edge structure (XANES), b) Ru K-edge extended X-ray absorption fine structure (EXAFS) spectra of RTO nanowires and RTN nanotubes showing changes in Ru valence and local coordination upon nitridation and exsolution. Reproduced with permission [43]. Copyright 2024, Wiley-VCH. c) Raman spectra of $Gd_{0.2-x}Ni_xCe_{0.8}O_{2-\delta}$ (GNDC) powders annealed at 600, 800, and 1250 °C, highlighting the evolution of fluorite lattice modes and vacancy-related bands. Reproduced with permission [165]. Copyright 2018, The Royal Society of Chemistry. XPS spectra of d) Fe 2p, e) Ni 2p, and f) O 1s for $NiFe_2O_4$ (NFO) and H_2-treated NFO samples (NFO-400H, NFO-500H, and NFO-600H), tracking cation reduction and oxygen vacancy formation during metal exsolution. Reproduced with permission [169]. Copyright 2022, The Royal Society of Chemistry. O 1s XPS spectra of g) H_2/Ar-treated $La_{0.6}Sr_{0.4}Fe_{0.8}Ni_{0.2}O_{3-\delta}$ (H-LSFN) and h) pristine LSFN showing surface and lattice oxygen components. Reproduced with permission [170]. Copyright 2023, Wiley-VCH. i) EPR spectra of the $SmMn_2O_5$, Mn_2O_3–$SmMn_2O_5$, Mn_2O_3/$SmMn_2O_5$, and Mn_2O_3 catalysts probing oxygen-vacancy-related paramagnetic centers. Reproduced with permission [174]. Copyright 2024, Springer Nature.

studies have examined the surface chemical reconstruction accompanying metal exsolution, including Ni-exsolved YSZ fluorite oxides [163] and PdPt alloy–perovskite catalysts for lean methane oxidation [172].

EPR spectroscopy, which detects the spin of unpaired electrons, has been widely employed to quantify oxygen vacancy-related defect centers and paramagnetic cations generated during exsolution in host materials [173]. For example, Wang et al. applied EPR (Fig. 12i) to exsolved Mn_2O_3/$SmMn_2O_5$ systems and showed that Mn_2O_3-decorated perovskites exhibited the strongest vacancy-related resonance among the tested samples, indicating that the highest oxygen vacancy density arises from strong metal–oxide interfacial interactions [174].

These spectroscopic results demonstrate that the chemical and electronic transformations accompanying exsolution, particularly in phase-tunable systems, where metal emergence is intertwined with nitridation, phosphidation, or sulfidation, cannot be fully understood using a single technique. As each method highlights a different aspect of the process, from bulk electronic restructuring to surface chemical evolution and defect formation, their combined interpretation enables a far more coherent and mechanistic understanding than any individual dataset can offer. Therefore, integrating information from XAS, Raman, XPS, and EPR provides a holistic view of how cation migration, vacancy generation, and nanoparticle nucleation collectively unfold during exsolution, ultimately revealing the electronic and structural origins of the material properties that emerge. As exsolution systems continue to

diversify, such multimodal spectroscopic analyses will remain essential for establishing precise structure–function relationships.

5.3. *In situ analyses*

Real-time spectroscopic monitoring is crucial for capturing the transient electronic and structural states experienced by exsolution-driven materials during operation. Because the active phases in these systems often emerge, evolve, and disappear in reaction environments, post-reaction characterization can easily misrepresent their true functional states or conflate reaction-induced changes with alterations caused by atmospheric exposure. This limitation is particularly severe in phase-tunable exsolution, where metal emergence is tightly coupled to host reconstruction and anion exchange, and multiple phases can coexist only transiently. This consideration underscores the necessity of performing in situ spectroscopy under working conditions, where the dynamic evolution of oxidation states, coordination environments, and interfacial bonding can be directly observed. By providing immediate evidence of these transformation pathways, in situ techniques enable a more accurate mechanistic understanding of exsolved metal systems and establish a reliable foundation for correlating structural and phase dynamics with performance trends. Building on this need for real-time

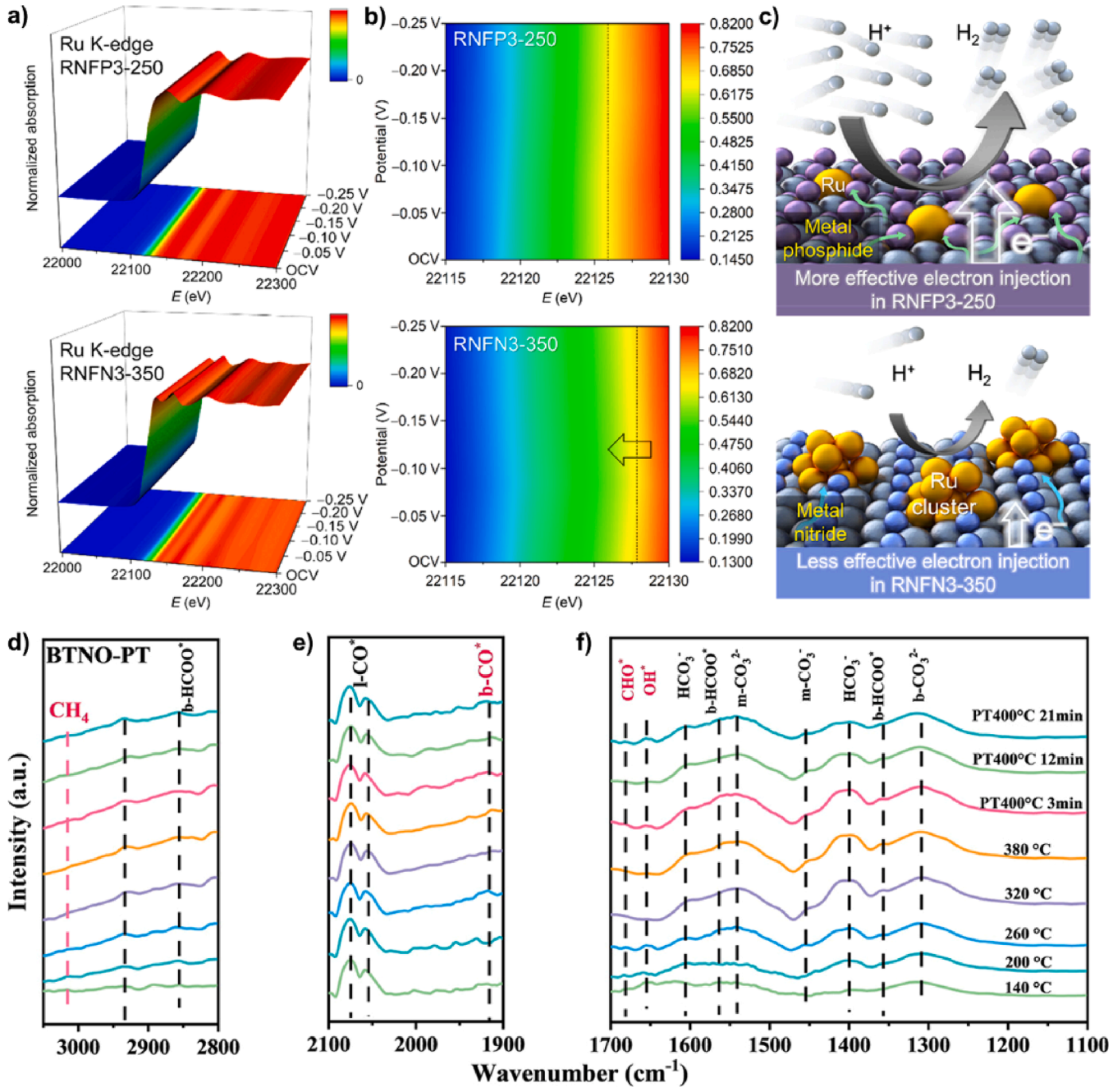

Fig. 13. a) In situ Ru K-edge XANES spectra, b) contour plots of the rising edge for Ru single atom-exsolved RNFP and Ru nanocluster-exsolved RNFN nanocomposites during HER measurement, highlighting the different potential-dependent evolution of Ru valence and charge accumulation, and c) Schematic illustration of the impact of exsolution atmosphere (P vs N) on interfacial electron transfer at Ru–pnictogenide interfaces during HER. Reproduced with permission [57]. Copyright 2025, Wiley-VCH. d–f) In situ diffuse reflectance infrared Fourier transform spectroscopy (DRIFTS) spectra of Ni-anchored $Ba_{0.9}Ti_{0.9}Ni_{0.1}O_{3-\delta}$ (BTNO) under dark and light irradiation during temperature-programmed CO_2 reduction, showing the formation of CO_2-derived surface intermediates and adsorbed CO species along the reaction pathway. Reproduced with permission [141]. Copyright 2025, Wiley-VCH.

structural insights, in situ XAS has emerged as one of the most powerful tools for probing exsolution-induced transformations at the atomic scale [175]. Owing to its sensitivity to oxidation state variations and local coordination environments, in situ XAS enables the direct tracking of how metal species nucleate, migrate, and restructure within their host lattices during the reaction. Such measurements reveal the evolution of exsolved nanoparticles, the dynamics of metal−support interactions, and the formation of transient active phases that govern catalytic and electrochemical performance features that cannot be fully captured through ex situ characterization. Sun et al. elucidated the origin of the relative efficacy of different exsolution pathways in optimizing the HER activity of Ru nanocatalysts by conducting *in situ* XANES measurements [57]. They synthesized Ru-substituted $Ni_2Fe_{1-x}Ru_x$-LDH precursors for exsolution via a coprecipitation method. And they induced exsolution through two routes: phosphidation using $NaH_2PO_2{\cdot}H_2O$ under H_2/Ar flow to obtain the phosphide nanocomposite (Ru single atom exsolved Ni_2P/Fe_2P, RNFP), and nitridation using NH_3 vapor to produce the nitride nanocomposite (Ru nanocluster exsolved Ni_3N/Fe_3N, RNFN). RNFP displayed an almost unchanged Ru K-edge position during the HER (Fig. 13a and b), with only a slight blue shift, even under applied reduction potentials. This spectral stability indicates that the exsolved Ru single atoms injected electrons into the reactants, preventing charge accumulation on the catalyst surface. By contrast, RNFN exhibits a pronounced decrease in the Ru K-edge energy upon the application of reductive potentials. This edge shift reflects significant charge buildup on the Ru nanoclusters, which is a clear indication of inefficient electron transfer to the reactants. Collectively, these *in situ* XANES observations demonstrate that single Ru atoms formed via phosphidation offer a markedly superior interfacial electron transfer capability compared to Ru nanoclusters produced through nitridation, thereby explaining the higher HER performance of RNFP relative to RNFN (Fig. 13c). They also establish a direct link between the anion identity (P vs N), the Ru speciation (single atom vs nanoclusters), and the operando charge-transfer behavior, which is central to the rational design of phase-tunable exsolution systems.

In addition, *in situ* Raman spectroscopy is indispensable for capturing the real-time evolution of surface bonding, lattice distortions, and metal−oxide interactions that inevitably arise during exsolution-driven structural transformations [176]. Yun et al. investigated the origin of the improved electrocatalytic performance of Ru−MnO@C nanowires by monitoring the evolution of their chemical bonding characteristics during the HER using *in situ* surface-enhanced Raman scattering (SERS) technique [42]. For both the Ru-free RM0-C and Ru-containing RM20-C samples, strong Raman features associated with carbon species were consistently observed in the 1200−1600 cm^{-1} region across all applied potentials. When the reductive potential was increased to −0.25 to −0.30 V, RM20-C exhibited a pronounced suppression of these carbon-related Raman peaks, whereas RM0-C showed no significant spectral change. This attenuation in RM20-C was attributed to enhanced H_2 bubble evolution induced by the exsolved Ru nanoclusters, reflecting increased HER activity. Additionally, Raman bands corresponding to SO_4^{2-} (~980 cm^{-1}) and HSO_4^- (~1050 cm^{-1}) were observed for both samples. With further increases in the reductive potential, RM20-C displayed a substantial decrease in the HSO^{4-} peak intensity, in contrast to the negligible variation in RM0-C, indicating more effective interfacial charge transfer facilitated by anchored Ru nanoclusters and the associated deprotonation of adsorbed HSO_4^- species.

Beyond *in situ* XAS and Raman techniques, *in situ* diffuse reflectance infrared Fourier transform spectroscopy (DRIFTS) provides powerful means to directly track the surface adsorption dynamics and vibration signatures of reaction intermediates under operating conditions. In situ DRIFTS enables precise identification of catalytic intermediates and surface-bound transition states. Li et al. investigated the reaction intermediates and mechanistic pathways in Ni-anchored $Ba_{0.9}Ti_{0.9}Ni_{0.1}O_{3-\delta}$ (BTNO) using *in situ* DRIFTS [141]. *In situ* DRIFTS revealed that BTNO formed a broader range of CO_2-derived intermediates, including HCO^{3-}/m-CO_3^{2-} (1526 and 1400 cm^{-1}), bidentate carbonate (1309, 2857, and 2935 cm^{-1}), and bidentate formate-HCOO* (1357 cm^{-1}), indicating stronger CO_2 adsorption and a higher oxygen vacancy concentration (Fig. 13d−f). BTNO also exhibited both linear CO* (2075 and 2055 cm^{-1}) and bridge CO* (1915 cm^{-1}) (Fig. 13e), supporting a more favorable formate-mediated reverse water gas shift (RWGS) pathway that ultimately forms CH_4.

Complementing the information obtained from *in situ* spectroscopy, *in situ* microscopy provides a powerful means to directly visualize the dynamic evolution of exsolution at atomic to nanoscale resolutions. Real-time imaging enables the observation of metal nucleation, migration pathways, lattice defect evolution, and reversible particle dissolution−exsolution events, which fundamentally govern the kinetics and stability of exsolved nanoparticles. By capturing these transient structural transformations under operational conditions, *in situ* microscopy revealed the critical interplay between the host lattice dynamics, emerging metal species, and the surrounding chemical environment.

In one instance, Lv et al. used in situ secondary electron-scanning transmission electron microscopy (SE-STEM) (Fig. 14a−d) and environmental scanning electron microscopy (ESEM) to directly monitor the exsolution of CoFe alloy nanoparticles from $Sr_2Fe_{1.35}Mo_{0.45}Co_{0.2}O_{6-\delta}$ (SFMC) perovskite under reducing atmospheres, showing that nanoparticles begin to emerge at 600 °C and significantly increase in both size and density upon further reduction at 700 °C, providing direct real-time evidence of thermally driven CoFe exsolution [177]. In situ observations revealed the sequential exsolution of Co followed by Fe, leading to the formation of CoFe alloy nanoparticles under a reducing atmosphere. Additionally, Lv et al. also employed in situ STEM to directly visualize the exsolution behavior of CoFe alloy nanoparticles from the $La_{0.4}Sr_{0.6}Co_{0.2}Fe_{0.7}Mo_{0.1}O_{3-\delta}$ (LSCFM) perovskite under a H_2 atmosphere [94]. In situ observations revealed that sub-nanometer metal species initially nucleate within or near the surface of the parent lattice and subsequently migrate to the surface, where they grow and coarsen into CoFe alloy nanoparticles during reduction (Fig. 14e).

In situ XRD further complements the electronic and structural insights obtained from spectroscopy and microscopy by capturing the real-time phase evolution and lattice-level transformations during exsolution. Through the diffraction-based monitoring of crystallographic changes, in situ XRD provides a bulk structural context that bridges local bonding information with nanoscale morphological dynamics, offering a more complete picture of the exsolution mechanisms. Ren et al. employed in situ XRD to monitor the phase evolution of $AgBiS_2$ during K^+ insertion, revealing a cascade of structural transformations, including $AgBiS_2$ displacement, BiS_2 conversion, and Bi alloying, which were directly correlated with the electrochemically driven Ag exsolution process [130]. This study exemplifies phase-transformation-coupled exsolution in a conversion-type electrode, where the cascade of host phase transitions and Ag emergence can be followed operando by in situ XRD. In another study, Cao et al. used in situ synchrotron XRD to unravel the structural evolution of $LaNiO_3$ during Ni exsolution, revealing a sequential decomposition pathway in which $LaNiO_3$ was first transformed into La_2NiO_4 and subsequently converted to La_2O_3 as the exsolution progressed [178]. When combined with in situ HR-TEM and electron energy loss spectroscopy (EELS), these diffraction results further demonstrate that the Ni exsolution process proceeds through distinct stages: atomic exsolution, nucleation, embedding, half-embedding, and final detachment of metallic Ni nanoparticles, accompanied by the formation of oxygen vacancies and lattice oxygen release under reducing conditions. The emergence of NiO was also attributed to the reaction between exsolved Ni and the spillover oxygen released from the perovskite lattice during decomposition. Together, these observations highlight how in situ XRD provides a bulk phase transition framework that complements the electronic and nanoscale structural insights obtained from in situ spectroscopy and microscopy, enabling a coherent mechanistic understanding of Ni exsolution that is inseparable from the perovskite-to-RP-to-La_2O_3 phase transformation.

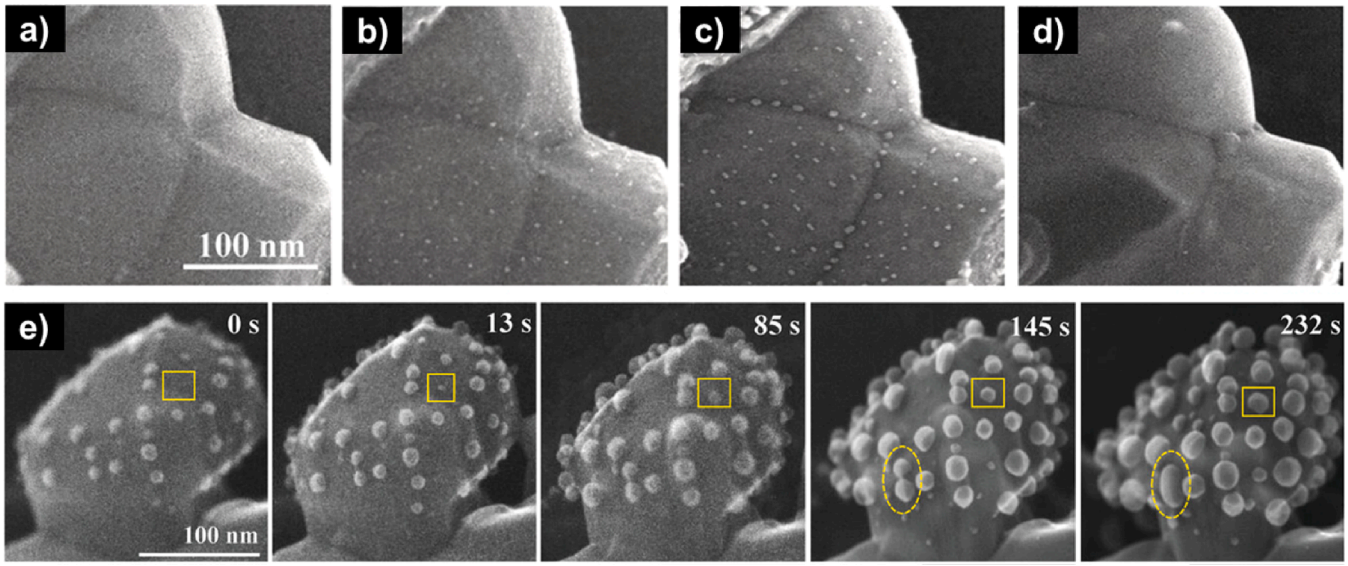

Fig. 14. In situ SE-STEM images of $La_{0.4}Sr_{0.6}Co_{0.2}Fe_{0.7}Mo_{0.1}O_{3-\delta}$ (LSCFM) recorded a) before reduction, b) after treatment in 10 Pa of H_2 at 600 °C, c) after further reduction in 10 Pa H_2 at 700 °C, and d) after re-oxidation in 10 Pa O_2 at 700 °C, showing the reversible emergence and disappearance of CoFe nanoparticles under redox cycling. Reproduced with permission [177]. Copyright 2020, Wiley-VCH. In situ STEM images of $Sr_2Fe_{1.35}Mo_{0.45}Co_{0.2}O_{6-\delta}$ (SFMC) under 10 Pa H_2 at 800 °C, capturing the time-dependent nucleation and growth of CoFe alloy nanoparticles on the perovskite surface. Reproduced with permission [94]. Copyright 2020, Wiley-VCH.

Sun et al. further demonstrated through in situ XRD that crystal reconstruction in Co-doped $Pr_{0.5}Ba_{0.5}MnO_x$ triggers ordered oxygen deficient layering and drives the rapid exsolution of Co nanoparticles under reducing conditions [179]. López-García et al. demonstrated that synchrotron-based in situ XRD combined with near-ambient pressure XPS (NAP-XPS) can be used to follow the reversible exsolution of ternary FeCoNi alloy nanoparticles from $Sr_2FeCo_{0.2}Ni_{0.2}Mn_{0.1}Mo_{0.5}O_{6-\delta}$ under redox cycling [180]. In situ XRD identified the onset temperature of alloy formation and the emergence of a minor RP phase, while temperature-resolved NAP-XPS and ex situ STEM-EDS revealed composition shifts and morphological changes of the regenerated alloy nanoparticles during repeated redox treatments. This study highlights how advanced in situ methods can resolve reversible multicomponent exsolution mechanisms and alloy evolution that are inaccessible to ex situ characterization alone.

5.4. Theoretical analyses

5.4.1. Defect thermodynamics and charge states

From a theoretical perspective, exsolution is most consistently described within the framework of defect thermodynamics and redox controlled charge states rather than as a simple surface reduction process. In perovskite oxides, the driving force for metal emergence is governed by the formation energies of the cation and anion defects, the position of the Fermi level under reducing conditions, and the relative stability of the different charge states of the dopant cation in the host lattice. A-site deficiency and oxygen non-stoichiometry modify the defect equilibria and can create regions where B-site cations are present in locally higher concentrations than in the nominal composition. In such environments, the partial release of these cations toward the surface can restore a more stable bulk composition and relieve the local strain.

Bonkowski et al. constructed a unified thermodynamic–kinetic model for Ni exsolution from A-site-deficient $SrTiO_3$ by combining hybrid DFT calculations with defect thermodynamics to describe defect formation and metal migration under a reducing atmosphere [66]. They showed that as the oxygen chemical potential decreased, the Fermi level shifted upward in the band gap and enabled the stepwise reduction of Ni^{2+} to Ni^{+} and finally to neutral Ni^0 at the defect-associated lattice sites. Neutral Ni^0 species are energetically disfavored in the perovskite framework and exhibit higher mobility than their charged counterparts; therefore, they tend to move toward the surface, where they form embedded metallic nanophases, as shown in Fig. 15a. This model provides a thermodynamic and kinetic basis for understanding how changes in the oxygen chemical potential and charge state transitions of Ni control the onset of exsolution in A-site-deficient $SrTiO_3$. Previously, Neagu et al. introduced a defect chemistry picture for A-site-deficient perovskites, in which non-stoichiometry was deliberately used to create conditions that favor the in situ growth of metal nanoparticles [70]. They showed that under reducing conditions, a combination of A-site deficiency and oxygen vacancy formation can allow the bulk lattice to lower its free energy when some of the B-site cations leave the perovskite framework and appear at the surface as metallic or oxide nanostructures, while the remaining matrix approaches a more favorable composition and bonding environment. This concept provides a thermodynamic basis for understanding how redox treatments can generate strongly anchored nanoparticles without severely degrading the oxide host. Alternatively, Yang et al. applied a combined defect thermodynamics and transport framework to a hybrid perovskite $CH_3NH_3PbI_3$ using DFT to calculate the formation energies and migration barriers of native defects and Au impurities [181]. They showed how the relative stability and mobility of different charged defects determine which species dominate ionic transport, and how these defect populations can lead to pronounced ionic conductivity and current–voltage hysteresis. Although their work does not address exsolution directly, the same type of analysis linking defect formation energies with migration barriers and charge states can be transferred to oxide and nitride hosts, where the balance between vacancy formation and dopant redox states governs the onset of metal emergence and the transport properties of the exsolved system. In summary, these studies provide a consistent thermodynamic framework in which exsolution is viewed as a defect-driven redistribution of cations controlled by the redox chemistry and nonstoichiometry of the host lattice rather than as a purely surface limited reaction. Although these analyses have so far been developed mainly for oxide hosts, the same defect-thermodynamic framework can be naturally extended to phase-tunable exsolution systems, where nitridation- or phosphidation-induced phase transitions are expected to modify defect formation energies, Fermi-level, and dopant charge-state distributions

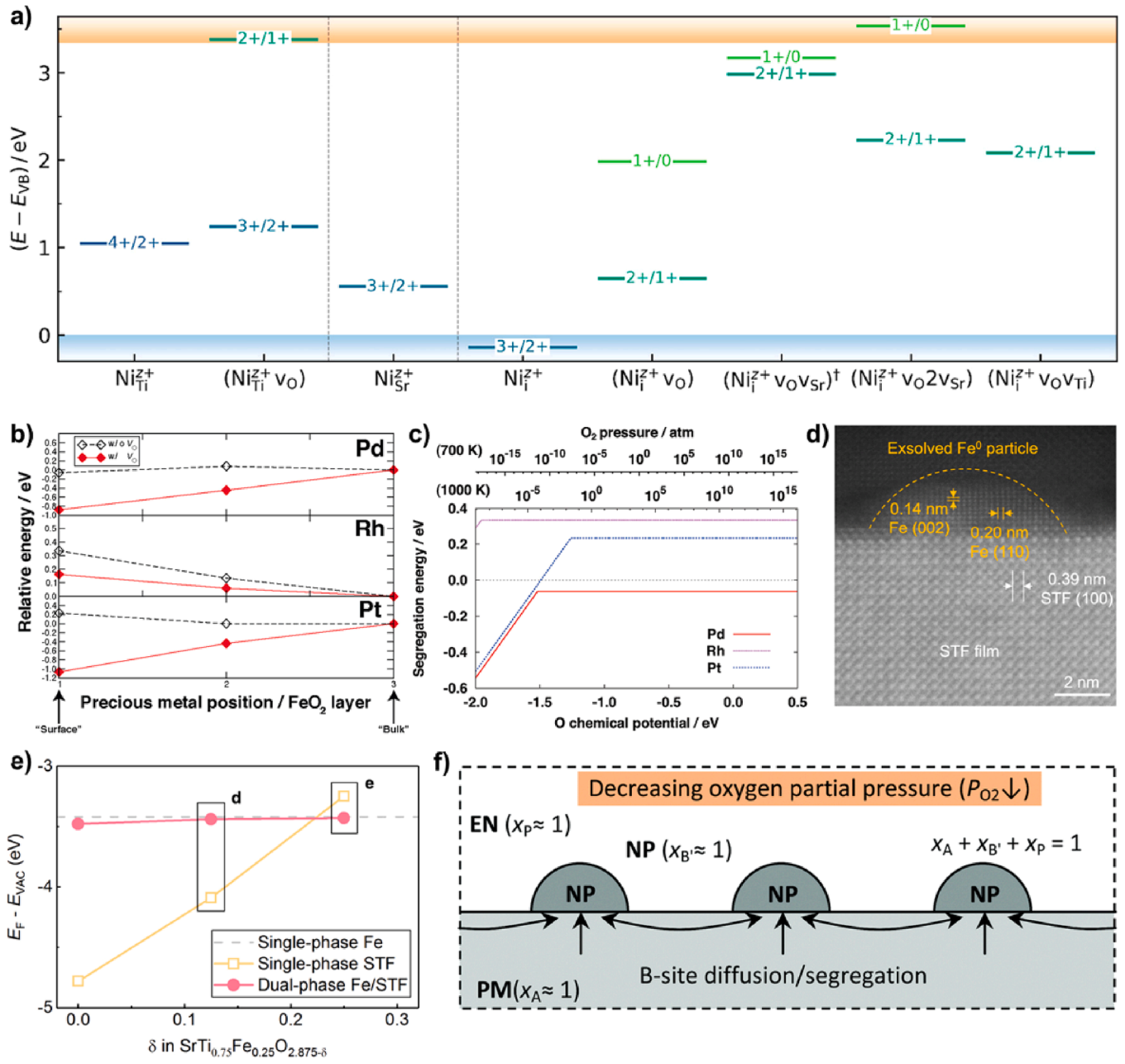

Fig. 15. a) Thermodynamic charge transition levels of Ni-related defects in $SrTiO_3$ based on hybrid DFT calculations. Reproduced with permission [66]. Copyright 2024, American Chemical Society. b) Relative energy diagram of the $LaFe_{1-x}M_xO_3$ as a function of precious metal position (solid line: with oxygen vacancy, dashed line: without oxygen vacancy) and c) surface segregation energy with oxygen chemical potential for precious metal species (Pd, Pt, and Rh). Reproduced with permission [182]. Copyright 2011, American Chemical Society. d) Cross-sectional high-angle annular dark field-STEM (HAADF-STEM) image of Fe/S-$rTi_{0.65}Fe_{0.35}O_{3-\delta}$ (Fe/STF) and e) Fermi energy level (E_F) of single-phase and dual-phase STF as a function of oxygen deficiency (dashed line: E_F of isolated Fe layer). Reproduced with permission [184]. Copyright 2025, American Chemical Society. f) Physical model for the exsolution of B-site species from $A_{1-x}BO_3$ perovskite surface. Reproduced with permission [187]. Copyright 2019, The Royal Society of Chemistry.

in a way that directly impacts the onset and driving force of metal emergence.

5.4.2. *Dopant selection and vacancy-assisted cation migration*

Beyond the overall driving force, the exsolution behavior is highly element specific; only certain dopants emerge as metallic or oxide nanoparticles under the given redox conditions, whereas others remain dissolved in the lattice. From a theoretical viewpoint, this selectivity is governed by the relative stability of the dopants at the bulk and near-surface sites and by the energetics of the vacancy-assisted migration paths that connect these sites. Hamada et al. used DFT to investigate $LaFe_{1-x}M_xO_3$ (M = Pd, Rh, or Pt) and compared the energetics of the M cations located in the bulk and at the surface in the presence of oxygen vacancies [182]. They found that Pd and Pt were significantly stabilized near the surface when oxygen vacancies were present, whereas Rh remained stable in the bulk lattice (Fig. 15b and 15c). These results indicate that oxygen vacancies preferentially stabilize Pd and Pt in the near-surface regions, whereas Rh tends to remain lattice bound, providing element specific insights into dopant site preferences in $LaFeO_3$-based perovskites. In another study, Kwon et al. carried out a compositionally broader analysis for layered $PrBaMn_2O_{5+\delta}$ oxides doped with transition metals such as Mn, Co, Ni, and Fe [39]. Using DFT,

they evaluated the tendency of each dopant to move together with the oxygen vacancies from the bulk to the surface and compared these trends with experimental observations of nanoparticle formation. The dopants that readily formed exsolved nanoparticles in the experiments (Mn, Co, and Ni) were predicted to have favorable energies for vacancy-assisted relocation toward the surface, whereas Fe did not, in agreement with the absence of Fe-rich particles. This study highlighted the central role of dopant-oxygen-vacancy co-segregation, showing that exsolution is promoted when reducible dopants and nearby vacancies can lower their energy by relocating toward the surface, whereas dopants that do not benefit from such co-segregation remain largely incorporated in the lattice. Neagu et al. later summarized these insights in a broader roadmap for exsolution, emphasizing that defect formation energies, dopant redox stability, and vacancy-assisted migration barriers should be considered when selecting host−dopant combinations for self-assembled nanocatalysts [183]. By combining defect chemical analysis with experimental trends across different perovskite systems, they outlined the design principles for choosing dopants that are prone to controlled exsolution under technologically relevant redox conditions while maintaining the structural robustness of the host matrix. These theoretical studies collectively show that dopant specific exsolution can be rationalized by comparing the stabilities of the bulk and near-surface configurations and by evaluating whether low barrier migration paths assisted by oxygen vacancies or other defects are available. These results offer a practical basis for selecting and prescreening compositions that are intrinsically favorable for controlled metal emergence. Consequently, dopant-vacancy co-segregation and vacancy-assisted migration provide a general microscopic picture not only for conventional oxide exsolution but also for phase-transformation-coupled cases, in which structural reconstruction and layered/RP formation are anticipated to further tune segregation energies, diffusion pathways, and preferred nucleation sites during phase-tunable exsolution.

5.4.3. Surface and interface electronic structure and reaction pathways

Although defect thermodynamics and migration energetics describe when and where metals emerge, the catalytic performance ultimately depends on the electronic structure at the metal/host interface and the reaction pathways that proceed there. Exsolution often produces partially embedded nanoparticles or clusters that are electronically coupled to the surrounding oxide, nitride, phosphide, or sulfide matrix. Local density of states (LDOS), band bending, and charge transfer at these junctions are crucial for understanding their activity and stability. Typically, Wang et al. examined exsolved Fe nanoparticles on $SrTi_{0.65}Fe_{0.35}O_{3-\delta}$ (STF) and combined experimental analyses with DFT to analyze Fermi level alignment and charge transfer at the metal−oxide interface [184]. Their DFT calculations and high-angle annular dark field scanning transmission electron microscopy (HAADF-STEM) measurements showed that upon exsolution, the Fermi levels of the metal and the host approach equilibrium, leading to characteristic band bending and charge redistribution at the interface (Fig. 15d and 15e). They further correlated the changes in the projected density of states (PDOS) of the interfacial atoms and real space charge density maps with the formation of either ohmic-like contacts or more resistive junctions. This work demonstrated that exsolution can improve the interfacial conductivity not only by creating metallic pathways but also by adjusting the electronic structure at the junction in a way that favors efficient charge transport during electrocatalytic operation.

The reaction energies and free energy profiles of the exsolved sites were analyzed in detail for several electrochemical and thermochemical reactions. Lv et al. studied RuFe alloy nanoparticles exsolved on $Sr_2Fe_{1.4}Ru_{0.1}Mo_{0.5}O_{6-\delta}$ for high temperature CO_2 electrolysis [185]. Using DFT, they compared the adsorption energies and free energy diagrams of CO_2 reduction intermediates on a RuFe alloy, bare perovskite, and at the RuFe−perovskite interface. They found that the interfacial sites stabilized $*CO_2$ and *CO intermediates more effectively than either phase alone, leading to a lower overall barrier for CO_2 electroreduction, which was consistent with the experimentally observed enhancement in activity and durability under repeated redox cycling. Kumar et al. performed a complementary first-principles study on exsolved Ni/La_2O_3 catalysts and analyzed the CO_2 activation and dissociation at different Ni/oxide interfacial motifs [186]. They calculated the adsorption geometries, adsorption energies, transition states, and free energy profiles for CO_2 splitting and showed that the $Ni-La_2O_3$ interface lowered the barriers for CO_2 dissociation relative to extended Ni surfaces. The calculations further indicated that the carbonate-like intermediates at the interface were stabilized by the combined electronic structures of Ni and La_2O_3, providing a clear microscopic rationale for the experimentally observed improvement in CO_2 conversion over the exsolved Ni/La_2O_3 catalysts. Such studies illustrate how electronic structure calculations on exsolved metal sites and metal/host interfaces can yield quantitative descriptors such as ΔG_{H^*} for hydrogen adsorption or free energy landscapes for CO_2 activation that directly correlate with measured reaction rates and selectivity. When combined with phase-transformation-coupled exsolution systems based on nitrides, phosphides, or sulfides, the same interface-resolved electronic-structure methodology can be applied to quantify how anion-exchange-induced changes in lattice covalency, band positions, and coordination environments reshape interfacial charge transfer, strain accommodation, and adsorption energetics at exsolved metal sites. Thereby, this links phase-tunable exsolution directly to microscopic catalytic descriptors such as hydrogen adsorption free energy or CO_2 activation barriers [43, 57,154].

5.4.4. Microstructure evolution and multi-scale modelling

Finally, the spatial and temporal evolution of exsolved nanostructures has been increasingly studied using mesoscopic and multiscale models linking atomistic energetics to microstructural changes. Although DFT provides local information on defect formation and interface energetics, exsolution in practical materials involves the nucleation, growth, and coarsening of many nanoparticles across grains and phase domains, which is often coupled with host reconstruction and phase transformation. Jiang et al. developed a phase field model for B-site nanoparticle exsolution from A-site-deficient perovskite surfaces (Fig. 15f) [187]. In their framework, the free energy includes contributions from the chemical composition, elastic strain, and interfacial energy, and is parameterized using defect and interface energetics obtained from atomistic calculations. Simulations of time-dependent evolution showed how nanoscale nuclei first form in defect-rich regions near the surface and then grow and coarsen under continued reduction, reproducing key experimental features such as preferred surface orientations, particle size distributions, and the persistence of partially embedded morphologies. Similarly, Xu et al. applied related concepts to electrochemically driven exsolution in perovskite fibers used as SOFC electrodes [122]. By combining electrochemical switching experiments with continuum level models, they followed how the local oxygen chemical potential, strain, and defect concentrations varied under an applied bias, and how these variations controlled the onset and spatial distribution of exsolved nanoparticles. Their analysis highlighted that the electrochemical control of the driving force can be used to confine exsolution to selected regions of the electrode, offering a way to engineer graded or patterned nanostructures for improved performance. In another study, Neagu et al. summarized these developments in their recent roadmap, emphasizing the need to integrate defect thermodynamics, atomistic energetics, and phase field or continuum modeling into a coherent multiscale description of exsolution [183]. They pointed out that such an approach can explain not only the steady-state distribution of nanoparticles, but also dynamic phenomena such as redox-induced reshaping, coarsening, and partial re-incorporation under cycling. The roadmap also highlights emerging opportunities to couple these models with data-driven and machine learning strategies, using high throughput calculations and experimental datasets to identify composition−structure−activity correlations and screen host

compositions that are predisposed to form highly dispersed, strongly anchored exsolved species. In combination with the defect thermodynamics and electronic structure studies discussed above, these microstructure-focused models provide a multi-scale perspective in which the thermodynamics, kinetics, and morphology are treated consistently. This perspective is particularly valuable for phase-tunable exsolution systems, where host reconstruction, anion exchange, and metal emergence proceed on comparable time scales. These processes must be considered simultaneously when describing nanoparticle nucleation, growth, coarsening, and partial re-incorporation during reduction conditions. In such cases, combining defect thermodynamics with phase-field and continuum-scale models offers a natural route to predict how nitridation-, phosphidation-, or sulfidation-induced phase transitions reorganize cation diffusion pathways, nucleation landscapes, and lattice-strain fields in a unified multiscale framework.

Overall, the theoretical studies summarized in Section 5.4 demonstrate that exsolution can be consistently interpreted in terms of defect thermodynamics, vacancy-assisted cation migration, interfacial electronic structure, and multiscale microstructure evolution. At present, however, truly dedicated computational investigations that explicitly treat phase-tunable exsolution, such as nitridation or sulfidation, remain scarce in the literature. Nevertheless, the existing models for conventional oxide exsolution systems provide a clear conceptual basis for extending defect-chemistry and multiscale simulations to phase-tunable exsolution, and future work along these lines will be crucial for quantitatively rationalizing how phase transitions control cation diffusion, nucleation, lattice strain, and ultimately catalytic performance.

6. Conclusions and perspectives

As an emerging synthetic route to nanostructured metal−inorganic nanohybrids, the exsolution method has garnered intense research interest because of its high efficacy in improving the diverse functionalities and durability of metal nanostructures [188–191]. Considering that nanostructured metal species suffer from agglomeration under extended operating conditions, such as catalysts, electrodes, and sensors, exsolution-assisted embedding of metal nanostructures can provide a powerful means to enhance their durability. In this review, we have summarized recent progress in exsolution-based synthesis, phase-tunable exsolved hybrid materials, advanced characterization methodologies, and energy-related applications of exsolved metals, with particular emphasis on how exsolution can simultaneously enhance performance and stability.

The formation of robust interfacial bonds between metal nanostructures and inorganic matrices is very effective in improving the stability of immobilized metal species and optimizing their versatile functionalities for applications such as energy conversion, energy storage, and photonics [191–195]. Beyond the classical picture of exsolution in phase-retaining oxide hosts, recent developments have extended the concept to phase-transformation-coupled exsolution, in which the host lattice is deliberately converted into conductive nitrides, phosphides, sulfides, or reconstructed oxides while metal species emerge from the bulk. This phase-tunable exsolution framework enables simultaneous control over metal speciation and host electronic/structural properties, opening new avenues for designing highly integrated hybrid catalysts and electrodes. In this review, we present a systematic and comprehensive survey of recent studies on the exsolution-based synthesis routes, phase-tunable exsolved hybrid materials, advanced characterization methodologies, and energy-related applications, with particular emphasis on how phase-tunable exsolution can be harnessed to enhance both performance and stability.

Depending on the experimental conditions used to induce the exsolution process, diverse types of metal nanostructures, such as metal nanoparticles, nanoclusters, and single atoms, can be immobilized in various inorganic matrices, such as metal oxides, metal chalcogenides, and metal pnictogenides [42,43,57,196]. Importantly, the exsolution-driven phase tuning of solid matrices can offer useful opportunities to further optimize the performance of embedded metal nanostructures via enhanced interfacial interactions with solid matrices.

(1) Synthetic routes to exsolved materials

The significant advantages of the exsolution approach have sparked research efforts to develop diverse exsolution-based synthesis routes such as reductive thermal annealing, electrochemical reduction, plasma treatment, selective removal of component ions, CO_2-assisted reduction, water-assisted reduction, and photoreduction. Depending on the activation mode and atmosphere, these methods can immobilize metal nanoparticles, nanoclusters, or single atoms in a wide range of inorganic matrices, such as oxides, chalcogenides, and pnictogenides [42,43,57,191]. Considering that particle size, spatial distribution, and metal−support interactions strongly affect the physicochemical properties of metal nanospecies, fine control of the exsolution conditions is crucial for optimizing their performance as catalysts, electrodes, and photonics [192–196].

(2) Phase-tunable exsolved materials

The choice of exsolution protocol and conditions can induce phase transitions of the host matrix into alternative crystal structures, giving rise to phase-transformation-coupled exsolution systems in which host conversion and metal emergence proceed cooperatively. For example, transforming oxide substrates into more conductive pnictogenides or chalcogenides enables simultaneous tuning of the host's electronic structure and the speciation of exsolved metals, from isolated single atoms to embedded nanoclusters, thereby strengthening interfacial electronic coupling and enhancing catalytic performance. In such phase-tunable architectures, reconstructed lattices, mixed-anion frameworks, and intentionally introduced defects act as internal templates that guide site-selective nucleation, control diffusion pathways, and modulate strain and band alignment at the metal−support interface. At the same time, the added structural complexity can introduce new degradation pathways under extended operation, including phase segregation, anion leaching, and slow microstructural relaxation, whose impact on long-term stability and partial reversibility is only beginning to be explored. Because systematic studies on phase-tunable exsolution remain relatively scarce compared to conventional phase-retaining systems, there is substantial scope for discovering new families of conductive hybrid matrices and for establishing quantitative design rules that link transformation pathways, microstructure evolution, and durability in device-relevant environments.

(3) Analytic techniques for investigating exsolved materials

For the rational design of exsolved functional materials, it is essential to clarify how exsolution processes influence their catalytic and electrochemical behavior under operational conditions. To this end, diverse in situ and operando characterization techniques, including XAS, Raman spectroscopy, DRIFTS, and XRD, have been employed to probe the evolution of metal species and host matrices. These methods provide critical insights into oxidation states, coordination environments, and structural dynamics that underpin the excellent functionalities of these materials. This is particularly vital for phase-transformation-coupled exsolution, where simple ex situ snapshots are insufficient to resolve the complex, often transient, interplay between host reconstruction, anion chemistry, and metal emergence. Operando spectroscopic, microscopic, and diffraction techniques are therefore required to track these coupled dynamics, allowing for the real-time visualization of host lattice phase evolution, the transformation of metal speciation, and the subsequent interfacial restructuring. By establishing such experimental links between operando phase/structural dynamics and device-level performance, these advanced analytical frameworks provide the mechanistic clarity necessary to bridge the gap between static design rules and real-world durability requirements.

(4) Promising performance of exsolved materials in various energy applications

Exsolved metal nanospecies embedded in solid matrices have been widely employed across diverse energy-related fields, including

electrocatalysis, photocatalysis, SOFC electrodes, and secondary batteries. Beyond the conventional benefits of size-tunable active sites, exsolution-derived architectures offer a unique structural advantage: the robust and socketed interface between the exsolved metal and the host matrix provides a powerful barrier against particle agglomeration and surface leaching, which are the primary degradation modes in conventional metal-supported catalysts. Crucially, this durability extends to phase-tunable systems, where mixed-anion or multiphase frameworks provide enhanced chemical stability and electronic synergy that further stabilize the active metal species under harsh redox and catalytic conditions. While the added complexity of host reconstruction in these tunable systems requires careful management, the resulting robust metal−matrix interfaces demonstrate significant potential in achieving the high catalytic activity and long-term stability required for next-generation energy conversion and storage technologies.

A key challenge that remains in exsolution-based materials, including both phase-retaining and phase-transformation-coupled systems, is to achieve a rational balance between performance and long-term durability under realistic operating conditions. In general, enhancing performance often requires increasing the density of exposed active sites, reducing particle size, and strengthening interactions with reaction intermediates; however, these same strategies may also cause particle agglomeration, surface or phase reconstruction, anion loss, or even partial dissolution of active species during extended operation. Exsolution offers a promising route to mitigate this trade-off because strongly anchored nanoparticles, socketed architectures, and extended metal−matrix interfaces can help preserve nanoscale active sites while facilitating charge transfer. Nevertheless, further efforts are needed to elucidate how exsolved nanostructures and their surrounding microstructures evolve under prolonged electrochemical, catalytic, or thermal stress, particularly under industrially relevant current densities, temperatures, and electrolyte environments. It is also necessary to establish design rules that simultaneously maximize activity, lifetime, and partial reversibility under repeated redox. In this context, developing strategies that simultaneously maximize catalytic performance and lifespan in exsolved and phase-tunable hybrids will be a central research hotspot in the coming years.

On this basis, several key challenges still need to be addressed for the practical implementation of exsolution-derived hybrid materials, as illustrated in Fig. 16. First, the development of efficient synthetic methods that allow precise control over crystal size, exposed facet, cation composition, and defect structure of exsolved metal nanospecies is required, because these parameters exert a profound influence on both their activity and stability. For phase-transformation-coupled exsolution, advanced material design strategies that deliberately couple exsolution with controlled host phase transitions, such as nitridation, phosphidation, sulfidation, or lattice reconstruction, are needed to define the target crystal structures, mixed-anion or multiphase frameworks, and metal speciation (from single atoms to nanoclusters) in a programmable manner. Such design-centric approaches should aim to engineer site-selective nucleation sites, diffusion pathways, and interfacial strain fields that stabilize the desired nanoscale architecture under operation conditions, while remaining compatible with earth-abundant compositions and scalable processing routes.

Second, a more comprehensive and site-selective characterization framework is needed to unravel the complex electrochemical and catalytic processes in exsolved systems, particularly those involving phase-transformation-coupled exsolution under realistic operating conditions. Combinatorial use of in situ/operando spectroscopic and microscopic tools, ideally correlated with ex situ analysis, should provide spatially and temporally resolved information on the surfaces of exsolved metals, metal–matrix interfaces, and defect sites within the host matrices, thereby clarifying degradation pathways, phase evolution, and structure–performance relationships over extended cycling. For phase-tunable architectures, it will be especially important to develop phase-resolved operando probes that can follow coupled host reconstruction, changes in metal speciation, and partial reversibility during repeated redox operation

Third, advanced multiscale theoretical calculations and machine-learning-assisted design strategies are expected to play a crucial role in guiding the rational discovery and optimization of exsolved materials, particularly for phase-transformation-coupled systems. By integrating DFT-level insights into exsolution thermodynamics, interfacial energetics, and diffusion kinetics with data-driven models trained on growing experimental and computational databases, it should be possible to establish quantitative composition–structure–property–operando response relationships, to map out optimal exsolution windows, and to inversely design host compositions and redox protocols for targeted energy applications.

Finally, although current research on exsolved hybrid materials has mainly focused on electrochemistry fields such as electrolysis, fuel cells, and secondary battery, the dynamic and self-regenerable nature of phase-transformation-coupled exsolution is expected to offer distinct advantages in a broader range of emerging technologies. Extending phase-tunable exsolution concepts from these core areas to additional domains such as thermoelectrics, photoelectrochemical devices, solar

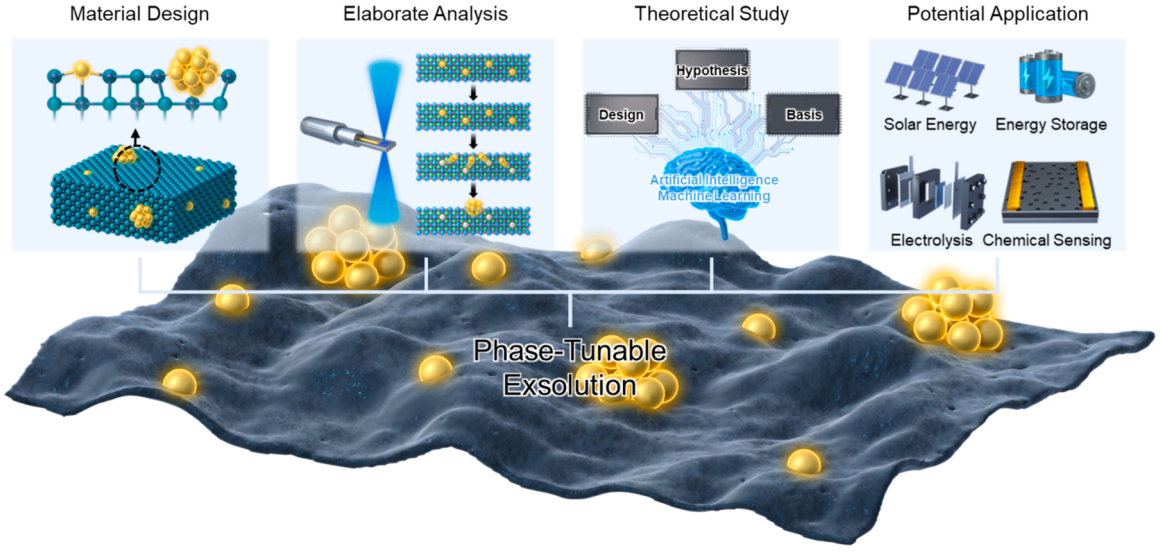

Fig. 16. Schematic diagram of future research direction for phase-tuning-assisted exsolution strategy.

conversion, chemical sensing, energy storage, and environmental catalysis could not only expand the application landscape of exsolved materials but also provide powerful feedback for refining material design strategies, elaborated analytical methodologies, and theory- and data-driven models tailored to complex operating environments.

Overall, these perspectives illustrate that phase-transformation-coupled exsolution is not only a versatile platform for designing robust hybrid catalysts, but also a fertile playground for integrating advanced material design, in-depth analysis, and theory- and data-driven strategies toward next-generation energy and environmental technologies.

CRediT authorship contribution statement

Taehoon Kim: Writing – original draft, Investigation. **Yeon Hu Park:** Writing – original draft, Investigation. **Jinyoung Lee:** Writing – original draft. **Ajayan Vinu:** Writing – review & editing, Writing – original draft, Supervision, Conceptualization. **Seong-Ju Hwang:** Writing – review & editing, Writing – original draft, Supervision, Project administration, Funding acquisition, Conceptualization.

Declaration of competing interest

The authors declare that they have no known competing financial interests or personal relationships that could have appeared to influence the work reported in this paper.

Acknowledgment

This work was supported by the National Research Foundation of Korea (NRF) grant funded by the Korea government (MSIT) (RS-2024-00411134 and RS-2024-00439825).

Data availability

No data was used for the research described in the article.

References

[1] Q. Sun, N. Wang, J. Yu, Advances in catalytic applications of zeolite-supported metal catalysts, Adv. Mater. 33 (2021) 2104442, https://doi.org/10.1002/adma.202104442.

[2] J.-J. Xu, W.-C. Zhang, Y.-W. Guo, X.-Y. Chen, Y.-N. Zhang, Metal nanoparticles as a promising technology in targeted cancer treatment, Drug Deliv. 29 (2022) 664–678, https://doi.org/10.1080/10717544.2022.2039804.

[3] H. Lin, X. Song, O.J.H. Chai, Q. Yao, H. Yang, J. Xie, Photoluminescent characterization of metal nanoclusters: Basic parameters, methods, and applications, Adv. Mater. 36 (2024) 2401002, https://doi.org/10.1002/adma.202401002.

[4] H. Liang, B.-J. Liu, B. Tang, S.-C. Zhu, S. Li, X.-Z. Ge, J.-L Li, J.-R. Zhu, F.-X. Xiao, Atomically precise metal nanocluster-mediated photocatalysis, ACS. Catal. 12 (2022) 4216–4226, https://doi.org/10.1021/acscatal.2c00841.

[5] X. Liang, N. Fu, S. Yao, Z. Li, Y. Li, The progress and outlook of metal single-atom-site catalysis, J. Am. Chem. Soc. 144 (2022) 18155–18174, https://doi.org/10.1021/jacs.1c12642.

[6] P. Wang, D. Zhao, L. Yin, Two-dimensional matrices confining metal single atoms with enhanced electrochemical reaction kinetics for energy storage applications, Energy Environ. Sci. 14 (2021) 1794–1834, https://doi.org/10.1039/d0ee02651d.

[7] J.H. Kim, J.K. Kim, J. Liu, A. Curcio, J.-S. Jang, I.-D. Kim, F. Ciucci, W.C. Jung, Nanoparticle ex-solution for supported catalysts: Materials design, mechanism and future perspectives, ACS. Nano 15 (2021) 81–110, https://doi.org/10.1021/acsnano.0c07105.

[8] Y.H. Kim, H. Jeong, B.-R. Won, H. Jeon, C.-h. Park, D. Park, Y. Kim, S. Lee, J.-h Myung, Nanoparticle exsolution on perovskite oxides: Insights into mechanism, characteristics and novel strategies, Nano-Micro Lett. 16 (2024) 33, https://doi.org/10.1007/s40820-023-01258-4. **Provide extensive fundamental mechanisms from the perspective of driving force and process of exsolution, materials design, and characteristics, suggesting direction for optimizing nanomaterials in various applications.**

[9] E. Calì, M.P. Thomas, R. Vasudevan, J. Wu, O. Gavalda-Diaz, K. Marquardt, E. Saiz, D. Neagu, R.R. Unocic, S.C. Parker, B.S. Guiton, D.J. Payne, Real-time insight into the multistage mechanism of nanoparticle exsolution from a perovskite host surface, Nat. Commun. 14 (2023) 1754, https://doi.org/10.1038/s41467-023-37212-6.

[10] Y.H. Kim, H. Jeong, B.-R. Won, J.-h. Myung, Exsolution modeling and control to improve the catalytic activity of nanostructured electrodes, Adv. Mater. 35 (2023) 2208984, https://doi.org/10.1002/adma.202208984.

[11] H. Han, J. Park, S.Y. Nam, K.J. Kim, G.M. Choi, S.S.P. Parkin, H.M. Jang, J.T. S. Irvine, Lattice strain-enhanced exsolution of nanoparticles in thin films, Nat. Commun. 10 (2019) 1471, https://doi.org/10.1038/s41467-019-09395-4.

[12] B. Rudolph, A.I. Tsiotsias, B. Ehrhardt, P. Dolcet, S. Gross, S. Haas, N.D. Charisou, M.A. Goula, S. Mascotto, Nanoparticle exsolution from nanoporous perovskites for highly active and stable catalysts, Adv. Sci. 10 (2023) 2205890, https://doi.org/10.1002/advs.202205890.

[13] M.A. Naeem, P.M. Abdala, A. Armutlulu, S.M. Kim, A. Fedorov, C.R. Müller, Exsolution of metallic Ru nanoparticles from defective, fluorite-type solid solutions $Sm_2Ru_xCe_{2-x}O_7$ to impart stability on dry reforming catalysts, ACS. Catal. 10 (2020) 1923–1937, https://doi.org/10.1021/acscatal.9b04555.

[14] S. Park, D. Oh, J. Ahn, J.K. Kim, D.-H. Kim, S. Kim, C. Park, W. Jung, I.-D. Kim, Promoting ex-solution from metal−organic-framework-mediated oxide scaffolds for highly active and robust catalysts, Adv. Mater. 34 (2022) 2201109, https://doi.org/10.1002/adma.202201109.

[15] S.A. Horlick, Y.-L. Huang, I.A. Robinson, E.D. Wachsman, Controlling exsolution with a charge-balanced doping approach, Nano Energy 87 (2021) 106193, https://doi.org/10.1016/j.nanoen.2021.106193.

[16] Y.H. Park, Y. Sun, D.W. Lee, I.Y. Kim, X. Jin, S.-J. Hwang, Recent trends in combinative defect engineering and hybridization approach to develop efficient energy-functional layered double hydroxide-based materials, Nano Res. Energy 4 (2025) e9120163, https://doi.org/10.26599/NRE.2025.9120163.

[17] G. Ji, L. Ji, S. Wu, L. Meng, Y. Jia, Z. Liu, S. Dong, J. Tian, Y. Li, In-situ exsolved ultrafine Ni nanoparticles from $CeZrNiO_2$ solid solution for efficient photothermal catalytic CO_2 reduction by CH_4, Adv. Powder Mater. 3 (2024) 100188, https://doi.org/10.1016/j.apmate.2024.100188.

[18] Y. Cong, Z. Geng, Q. Zhu, H. Hou, X. Wu, X. Wang, K. Huang, S. Feng, Cation-exchange-induced metal and alloy dual-exsolution in perovskite ferrite oxides boosting the performance of Li−O_2 battery, Angew. Chem., Int. Ed. 60 (2021) 23380–23387, https://doi.org/10.1002/anie.202110116.

[19] Y.-F. Sun, Y.-L. Yang, J. Chen, M. Li, Y.-Q. Zhang, J.-H. Li, B. Hua, J.-L. Luo, Toward a rational photocatalyst design: A new formation strategy of co-catalyst/semiconductor heterostructures: Via in situ exsolution, Chem. Commun. 54 (2018) 1505–1508, https://doi.org/10.1039/c7cc08797g.

[20] H.M. Ansari, A.S. Bass, N. Ahmad, V.I. Birss, Unraveling the evolution of exsolved Fe-Ni alloy nanoparticles in Ni-doped $La_{0.3}Ca_{0.7}Fe_{0.7}Cr_{0.3}O_{3-\delta}$ and their role in enhancing CO_2−CO electrocatalysis, J. Mater. Chem. A 10 (2022) 2280–2294, https://doi.org/10.1039/d1ta07552g.

[21] S. Liu, K.T. Chuang, J.-L. Luo, Double-layered perovskite anode with in situ exsolution of a Co−Fe alloy to cogenerate ethylene and electricity in a proton-conducting ethane fuel cell, ACS. Catal. 6 (2016) 760–768, https://doi.org/10.1021/acscatal.5b02296.

[22] J. Lee, Y.J. Kwon, H. Choi, S.Y. Kim, J.-H. Lee, Y.K. Jeong, Ultra-selective and stable ethylene detection via exsolution of catalytic Ni nanoparticles in chemiresistive gas sensors, J. Mater. Chem. A 13 (2024) 4851–4860, https://doi.org/10.1039/d4ta06829g.

[23] H. Kim, A. Jan, D.-H. Kwon, H.-I Ji, K.J. Yoon, J.-H. Lee, Y. Jun, J.-W. Son, S. Yang, Exsolution of Ru nanoparticles on $BaCe_{0.9}Y_{0.1}O_{3-\delta}$ modifying geometry and electronic structure of Ru for ammonia synthesis reaction under mild conditions, Small. 19 (2023) 2205424, https://doi.org/10.1002/smll.202205424.

[24] H. Ren, G. Zhi, C. Chen, H. Fang, Z. Lin, L. Lin, Y. Luo, C. Au, L. Jiang, In situ exsolution of Ni−Co alloys from A-site-deficient perovskite for efficient ammonia decomposition, Int. J. Hydrogen. Energy 96 (2024) 385–395, https://doi.org/10.1016/j.ijhydene.2024.11.315.

[25] D. Tao, Y. Qi, S. Fu, N. Yang, K. Liu, Z. Chen, L. Li, Plasma driven exsolution of Ca as the adjacent dechlorinated site in $La_{0.8}Ca_{0.2}MnO_3$ perovskite: A highly mineralization chlorobenzene oxidation catalyst, Appl. Catal. A Gen. 681 (2024) 119784, https://doi.org/10.1016/j.apcata.2024.119784.

[26] Z. Du, H. Zhao, S. Yi, Q. Xia, Y. Gong, Y. Zhang, X. Cheng, Y. Li, L. Gu, K. Świerczek, High-performance anode material $Sr_2FeMo_{0.65}Ni_{0.35}O_{6-\delta}$ with in situ exsolved nanoparticle catalyst, ACS. Nano 10 (2016) 8660–8669, https://doi.org/10.1021/acsnano.6b03979.

[27] J. Lv, W. Sun, C. Xu, X. Yang, M. Ma, L. Zhang, S. Zhang, J. Qiao, S. Zhen, K. Sun, Enhancing the catalytic activity and CO_2 chemisorption ability of the perovskite cathode for solid oxide electrolysis cell through in situ Fe−Sn alloy nanoparticles, Sep. Purif. Technol. 294 (2022) 121127, https://doi.org/10.1016/j.seppur.2022.121127.

[28] Y. Yang, M. Luo, W. Zhang, Y. Sun, X. Chen, S. Guo, Metal surface and interface energy electrocatalysis: Fundamentals, performance engineering, and opportunities, Chem. 4 (2018) 2054–2083, https://doi.org/10.1016/j.chempr.2018.05.019.

[29] H. Sun, C.-W. Tung, Y. Qiu, W. Zhang, Q. Wang, Z. Li, J. Tang, H.-C. Chen, C. Wang, H.M. Chen, Atomic metal−support interaction enables reconstruction-free dual-site electrocatalyst, J. Am. Chem. Soc. 144 (2022) 1174–1186, https://doi.org/10.1021/jacs.1c08890.

[30] J. Xu, W. Tang, C. Yang, I. Manke, N. Chen, F. Lai, T. Xu, S. An, H. Liu, Z. Zhang, Y. Cao, N. Wang, S. Zhao, D. Niu, R. Chen, A highly conductive COF@CNT electrocatalyst boosting polysulfide conversion for Li−S chemistry, ACS. Energy Lett. 6 (2021) 3053–3062, https://doi.org/10.1021/acsenergylett.1c00943.

[31] J. Liu, Q. Ma, Z. Huang, G. Liu, H. Zhang, Recent progress in graphene-based noble-metal nanocomposites for electrocatalytic applications, Adv. Mater. 31 (2019) 1800696, https://doi.org/10.1002/adma.201800696.

[32] J. Lee, T. Kim, D.H. Sun, X. Jin, S.-J. Hwang, Recent advances in two-dimensional metal pnictogenide nanosheets and their nanohybrids with diverse energy applications, EnergyChem 7 (2025) 100139, https://doi.org/10.1016/j.enchem.2024.100139.

[33] Y. Nishihata, J. Mizuki, T. Akao, H. Tanaka, M. Uenishi, M. Kimura, T. Okamoto, N. Hamada, Self-regeneration of a Pd−perovskite catalyst for automotive emissions control, Nature 418 (2002) 164–167, https://doi.org/10.1038/nature00893. **Discover reversible behavior of Pd ions substituted in perovskite matrix during redox cycle for the first time**.

[34] B.D. Madsen, W. Kobsiriphat, Y. Wang, L.D. Marks, S.A. Barnett, Nucleation of nanometer-scale electrocatalyst particles in solid oxide fuel cell anodes, J. Power. Sources. 166 (2007) 64–67, https://doi.org/10.1016/j.jpowsour.2006.12.080.

[35] D. Neagu, J.T.S. Irvine, Structure and properties of $La_{0.4}Sr_{0.4}TiO_3$ ceramics for use as anode materials in solid oxide fuel cells, Chem. Mater. 22 (2010) 5042–5053, https://doi.org/10.1021/cm101508w.

[36] G. Tsekouras, D. Neagu, J.T.S. Irvine, Step-change in high temperature steam electrolysis performance of perovskite oxide cathodes with exsolution of B-site dopants, Energy Environ. Sci. 6 (2013) 256–266, https://doi.org/10.1039/c2ee22547f. **Conceptualize diffusion of B-site dopants to the surface and formation of nanoparticles as exsolution**.

[37] D. Neagu, T.-S. Oh, D.N. Miller, H. Ménard, S.M. Bukhari, S.R. Gamble, R. J. Gorte, J.M. Vohs, J.T.S. Irvine, Nano-socketed nickel particles with enhanced coking resistance grown in situ by redox exsolution, Nat. Commun. 6 (2015) 8120, https://doi.org/10.1038/ncomms9120. **Provide structural and morphological analysis of the exsolved materials, revealing a unique structure which metal nanoparticles are partially embedded in surface of the host oxide matrix**.

[38] J.-h. Myung, D. Neagu, D.N. Miller, J.T.S. Irvine, Switching on electrocatalytic activity in solid oxide cells, Nature 537 (2016) 528–531, https://doi.org/10.1038/nature19090.

[39] O. Kwon, S. Sengodan, K. Kim, G. Kim, H.Y. Jeong, J. Shin, Y.-W. Ju, J.W. Han, G. Kim, Exsolution trends and co-segregation aspects of self-grown catalyst nanoparticles in perovskites, Nat. Commun. 8 (2017) 15967, https://doi.org/10.1038/ncomms15967.

[40] V. Kyriakou, R.K. Sharma, D. Neagu, F. Peeters, O.D. Luca, P. Rudolf, A. Pandiyan, W. Yu, S.W. Cha, S. Welzel, M.C.M.V.D. Sanden, M.N. Tsampas, Plasma driven exsolution for nanoscale functionalization of perovskite oxides, Small. Methods 5 (2021) 2100868, https://doi.org/10.1002/smtd.202100868.

[41] H. Khalid, A. ul Haq, B. Alessi, J. Wu, C.D. Savaniu, K. Kousi, I.S. Metcalfe, S. C. Parker, J.T.S. Irvine, P. Maguire, E.I. Papaioannou, D. Mariotti, Rapid plasma exsolution from an A-site deficient perovskite oxide at room temperature, Adv. Energy Mater. 12 (2022) 2201131, https://doi.org/10.1002/aenm.202201131.

[42] S.Y. Yun, X. Jin, S.-J. Hwang, A one-pot carbon-coating-ex-solution route to efficient Ru−MnO@C nanowire electrocatalysts with enhanced interfacial interactions, Chem. Eng. J. 446 (2022) 136816, https://doi.org/10.1016/j.cej.2022.136816.

[43] S.Y. Yun, S. Lee, X. Jin, A. Soon, S.-J. Hwang, Ammonolysis-driven exsolution of Ru nanoparticle embedded in conductive metal nitride matrix to boost electrocatalyst activity, Adv. Sci. 11 (2024) 2309819, https://doi.org/10.1002/advs.202309819. **Combine anion substitution and exsolution, inducing phase transformation of TiO_2 matrix to TiN and exsolution of Ru ions to nanocluster**.

[44] X. Li, Z.Y. Niu, M. Niu, J.X. Wang, D. Cao, X. Zeng, Single atom Ru doped Ni_2P/Fe_3P heterostructure for boosting hydrogen evolution for water splitting, Small. 20 (2024) 2311335, https://doi.org/10.1002/smll.202311335.

[45] P. Hu, X. Zhang, M. Xu, Y. Lv, H. Guo, J.S. Chen, X. Ye, H. Xian, X. Sun, T. Li, In-situ exsolution of FeCo nanoparticles over perovskite oxides for efficient electrocatalytic nitrate reduction to ammonia via localized electrons, Appl. Catal. B-Environ. 357 (2024) 124267, https://doi.org/10.1016/j.apcatb.2024.124267.

[46] F. Hu, Y. Ling, S. Fang, L. Sui, H. Xiao, Y. Huang, S. Wang, B. He, L. Zhao, Engineering dual-exsolution on self-assembled cathode to achieve efficient electrocatalytic CO_2 reduction, Appl. Catal. B-Environ. 337 (2023) 122968, https://doi.org/10.1016/j.apcatb.2023.122968.

[47] X. Zhang, X. Xiao, Q. Zhang, Z. Chen, C. Jiang, M. Chen, N. Yan, S. Mo, M. Wu, J. Li, J. Huang, A.N. Alodhayb, X. Fu, M. Chen, X. Lv, Y. Sun, Quantitative unraveling of exsolved heteroboundaries for high-temperature electrocatalysis, J. Am. Chem. Soc. 147 (2024) 462–472, https://doi.org/10.1021/jacs.4c11274.

[48] L. Wang, B. Li, M. Li, Y. Zhang, T. Yuan, Y. Ding, T. Li, C. Peng, S. Jiang, X. Xiong, L. Zhang, E. Liu, M. Liu, B. Zhao, Rational design and dynamic Ru exsolution enables active heterostructures surpassing Pt for alkaline hydrogen evolution, J. Am. Chem. Soc. (2025), https://doi.org/10.1021/jacs.5c16183 in press.

[49] L. Fu, J. Zhou, L. Zhou, J. Yang, Z. Liu, K. Wu, H. Zhao, J. Wang, K. Wu, Facile fabrication of exsolved nanoparticle-decorated hollow ferrite fibers as active electrocatalyst for oxygen evolution reaction, Chem. Eng. J. 418 (2021) 129422, https://doi.org/10.1016/j.cej.2021.129422.

[50] Y. Li, S. Li, X. Li, W. Meng, L. Dai, L. Wang, Electrochemical exsolution of Ag nanoparticles from $AgNbO_3$ sensing electrode for enhancing the performance of mixed potential type NH_3 sensors, Sens. Actuators B-Chem. 344 (2021) 130296, https://doi.org/10.1016/j.snb.2021.130296.

[51] C. Xin, L. Zhao, Y. Xing, H. Zhang, C. Yu, Z. Wei, T. Fei, S. Liu, H. Zhang, T. Zhang, An in situ exsolution strategy to prepare metallic Sn modified SnO_2 with oxygen vacancies for ppb-level NO_2 detection, Sens. Actuators B-Chem. 419 (2024) 136232, https://doi.org/10.1016/j.snb.2024.136232.

[52] Y. Cai, H. Jia, C. Li, X. Si, J. Cao, W. Fei, J. Qi, In situ exsolution of metallic Cu in mixed oxides as battery-type electrode for energy storage devices, Chem. Eng. J. 418 (2021) 129495, https://doi.org/10.1016/j.cej.2021.129495.

[53] H. Zhou, W. Han, H. Chai, H. Huang, J. Zheng, H. Zhang, L. Li, W. Zhou, B. An, C. Sun, Metal-ion exsolution effect to accelerate the reaction kinetics in Li−S batteries, J. Mater. Chem. A 12 (2024) 20238–20246, https://doi.org/10.1039/d4ta03248a.

[54] Z. Sun, C. Hao, S. Toan, R. Zhang, H. Li, Y. Wu, H. Liu, Z. Sun, Recent advances in exsolved perovskite oxide construction: Exsolution theory, modulation, challenges, and prospects, J. Mater. Chem. A 11 (2023) 17961–17976, https://doi.org/10.1039/d3ta03292b.

[55] H. Jeong, Y.H. Kim, B.-R. Won, H. Jeon, C.-h. Park, J.-h. Myung, Emerging exsolution materials for diverse energy applications: Design, mechanism, and future prospects, Chem. Mater. 35 (2023) 3745–3764, https://doi.org/10.1021/acs.chemmater.3c00004.

[56] K. Kousi, C. Tang, I.S. Metcalfe, D. Neagu, Emergence and future of exsolved materials, Small. 17 (2021) 2006479, https://doi.org/10.1002/smll.202006479.

[57] D.H. Sun, S.Y. Yun, X. Jin, S.-J. Hwang, Pnictogenation-driven exsolution of size-tunable Ru electrocatalysts in conductive matrices to reinforce inner-sphere-mechanism-assisted electronic coupling, Carbon Energy 7 (2025) e70013, https://doi.org/10.1002/cey2.70013. **Investigate anion effect to exsolution process by comparing nitridation and phosphidation of Ru-substituted Ni−Fe-LDH, which revealed size of the exsolved Ru ions is controllable (nanoclusters for nitridation and single atoms for phosphidation)**.

[58] Y. Tian, C. Yang, Y. Wang, M. Xu, Y. Ling, J. Pu, F. Ciucci, J.T.S. Irvine, B. Chi, Phase transition with in situ exsolution nanoparticles in the reduced $Pr_{0.5}Ba_{0.5}Fe_{0.8}Ni_{0.2}O_{3-\delta}$ electrode for symmetric solid oxide cells, J. Mater. Chem. A 10 (2022) 16490–16496, https://doi.org/10.1039/d2ta03395j.

[59] B.-W. Zhang, M.-N. Zhu, M.-R. Gao, X. Xi, N. Duan, Z. Chen, R.-F. Feng, H. Zeng, J.-L. Luo, Boosting the stability of perovskites with exsolved nanoparticles by B-site supplement mechanism, Nat. Commun. 13 (2022) 4618, https://doi.org/10.1038/s41467-022-32393-y.

[60] A.J. Carrillo, A. Lopez-Garcia, B. Delgado-Galicia, J.M. Serra, New trends in nanoparticle exsolution, Chem. Commun. 60 (2024) 7987–8007, https://doi.org/10.1039/d4cc01983k.

[61] W. O'Leary, L. Giordano, J.L.M. Rupp, Tuning reduction conditions to understand and control Ni exsolution from $Sr_{0.8}La_{0.1}Ca_{0.1}Ti_{0.94}Ni_{0.06}O_{3-\delta}$, J. Mater. Chem. A 11 (2023) 21429–21442, https://doi.org/10.1039/d3ta04817a.

[62] F. Hu, B. Wei, B. He, X. Yu, S. Zhao, Y. Chen, W. Wang, L. Zhao, Q. Chen, Recent advances and future prospects in exsolution technology for solid oxide cells, Energy Rev 4 (2025) 100141, https://doi.org/10.1016/j.enrev.2025.100141.

[63] P.G. Sundell, M.E. Björketun, G. Wahnström, Thermodynamics of doping and vacancy formation in $BaZrO_3$ perovskite oxide from density functional calculations, Phys. Rev. B 73 (2006) 104112, https://doi.org/10.1103/PhysRevB.73.104112.

[64] W. O'Leary, L. Giordano, J. Park, S.S. Nonnenmann, Y. Shao-Horn, J.L.M. Rupp, Influence of Sr-site deficiency, Ca/Ba/La doping on the exsolution of Ni from $SrTiO_3$, J. Am. Chem. Soc. 145 (2023) 13768–13779, https://doi.org/10.1021/jacs.2c12011.

[65] K. Kim, B. Koo, Y.-R. Jo, S. Lee, J.K. Kim, B.-J. Kim, W. Jung, J.W. Han, Control of transition metal−oxygen bond strength boosts the redox ex-solution in a perovskite oxide surface, Energy Environ. Sci. 13 (2020) 3404–3411, https://doi.org/10.1039/d0ee01308k.

[66] A. Bonkowski, M.J. Wolf, J. Wu, S.C. Parker, A. Klein, R.A.D. Souza, A single model for the thermodynamics and kinetics of metal exsolution from perovskite oxides, J. Am. Chem. Soc. 146 (2024) 23012–23021, https://doi.org/10.1021/jacs.4c03412. **Provide comprehensive explanation of exsolution process in terms of thermodynamics and kinetics supported by DFT calculations**.

[67] M.L. Weber, B. Šmíd, U. Breuer, M.-A. Rose, N.H. Menzler, R. Dittmann, R. Waser, O. Guillon, F. Gunkel, C. Lenser, Space charge governs the kinetics of metal exsolution, Nat. Mater. 23 (2024) 406–413, https://doi.org/10.1038/s41563-023-01743-6.

[68] D. Neagu, E.I. Papaioannou, W.K.W. Ramli, D.N. Miller, B.J. Murdoch, H. Ménard, A. Umar, A.J. Barlow, P.J. Cumpson, J.T.S. Irvine, I.S. Metcalfe, Demonstration of chemistry at a point through restructuring and catalytic activation at anchored nanoparticles, Nat. Commun. 8 (2017) 1855, https://doi.org/10.1038/s41467-017-01880-y.

[69] J. Wang, D. Kalaev, J. Yang, I. Waluyo, A. Hunt, J.T. Sadowski, H.L. Tuller, B. Yildiz, Fast surface oxygen release kinetics accelerate nanoparticle exsolution in perovskite oxides, J. Am. Chem. Soc. 145 (2023) 1714–1727, https://doi.org/10.1021/jacs.2c10256.

[70] D. Neagu, G. Tsekouras, D.N. Miller, H. Ménard, J.T.S. Irvine, In situ growth of nanoparticles through control of non-stoichiometry, Nat. Chem. 5 (2013) 916–923, https://doi.org/10.1038/nchem.1773.

[71] J. Wang, J. Yang, A.K. Opitz, W. Bowman, R. Bliem, G. Dimitrakopoulos, A. Nenning, I. Waluyo, A. Hunt, J.-J. Gallet, B. Yildiz, Tuning point defects by elastic strain modulates nanoparticle exsolution on perovskite oxides, Chem. Mater. 33 (2021) 5021–5034, https://doi.org/10.1021/acs.chemmater.1c00821.

[72] Y. Luo, J. Wang, Q. Wang, K. Ma, Y. Wang, T. Liu, M. Ding, Unraveling the evolution and regulation mechanisms of reversible exsolution in perovskite-based nanoparticles, Adv. Funct. Mater. (2025) e17547, https://doi.org/10.1002/adfm.202517547.

[73] X. Yao, Q. Cheng, Y. Attada, S. Ould-Chikh, A. Ramírez, X. Bai, H.O. Mohamed, G. Li, G. Shterk, L. Zheng, J. Gascon, Y. Han, O.M. Bakr, P. Castaño, Atypical stability of exsolved Ni−Fe alloy nanoparticles on double layered perovskite for

CO_2 dry reforming of methane, Appl. Catal. B-Environ. 328 (2023) 122479, https://doi.org/10.1016/j.apcatb.2023.122479.
[74] S. Ding, M. Li, W. Pang, B. Hua, N. Duan, Y.-Q. Zhang, S.-N. Zhang, Z. Jin, J.-L. Luo, A-site deficient perovskite with nano-socketed Ni−Fe alloy particles as highly active and durable catalyst for high-temperature CO_2 electrolysis, Electrochim. Acta 335 (2020) 135683, https://doi.org/10.1016/j.electacta.2020.135683.
[75] C. Hao, Z. Qu, L.R. Smith, N.F. Dummer, H. Qi, T.J.A. Slater, Z. Zhu, R. Zhang, Z. Sun, Z. Sun, G.J. Hutchings, Ce-induced synergistic effect in exsolved perovskite catalyst for highly efficient and robust methane dry reforming, Nat. Commun. 16 (2025) 10630, https://doi.org/10.1038/s41467-025-65619-w.
[76] A. Kumar, R. Srivastava, Metal exsolution catalysts: A conceptual framework for stable catalytic systems for biomass valorization, Chem. - Eur. J. 31 (2025) e02569, https://doi.org/10.1002/chem.202502569.
[77] C. Melcher, A. Nenning, F. Schrenk, K. Rath, C. Rameshan, A.K. Opitz, The dark side of metal exsolution: A combined in situ surface spectroscopic and electrochemical study on perovskite-type cathodes for high-temperature CO_2 electrolysis, EES Catal 3 (2025) 550–565, https://doi.org/10.1039/d5ey00013k.
[78] A.K. Opitz, A. Nenning, V. Vonk, S. Volkov, F. Bertram, H. Summerer, S. Schwarz, A. Steiger-Thirsfeld, J. Bernardi, A. Stierle, J. Fleig, Understanding electrochemical switchability of perovskite-type exsolution catalysts, Nat. Commun. 11 (2020) 4801, https://doi.org/10.1038/s41467-020-18563-w.
[79] A. Schwiers, D. Röhrer, C. Lenser, B. Steinrücken, D. Sebold, H. Spliethoff, O. Guillon, N.H. Menzler, Phase stability, redox-behavior and carbon-tolerance of $Sr_{1-x}(Ti_{0.3}Fe_{0.7-y}Ni_y)O_{3-\delta}$ with exsolved nanoparticles, J. Mater. Chem. A 12 (2024) 9132–9146, https://doi.org/10.1039/d3ta05813a.
[80] A. López-García, A. Domínguez-Saldaña, A.J. Carrillo, L. Navarrete, M.I. Valls, B. García-Baños, P.J. Plaza-Gonzalez, J.M. Catala-Civera, J.M. Serra, Microwave-driven exsolution of Ni nanoparticles in A-site deficient perovskites, ACS. Nano 17 (2023) 23955–23964, https://doi.org/10.1021/acsnano.3c08534.
[81] D. Delgado, G. Koch, S. Jiang, J. Dong, J. Kröhnert, F.P. Schmidt, T. Lunkenbein, C.G. Ruano, J. Gaona-Miguélez, D. Troya, P. Oña-Burgos, A. Trunschke, Low-temperature exsolution of Rh from mixed ZnFeRh oxides toward stable and selective catalysts in liquid-phase hydroformylation, J. Am. Chem. Soc. 147 (2025) 5887–5903, https://doi.org/10.1021/jacs.4c14839.
[82] Y. Sun, J. Zhou, J. Yang, D. Neagu, Z. Liu, C. Yin, Z. Xue, Z. Zhou, J. Cui, K. Wu, Nanosurface-reconstructed fuel electrode by selective etching for highly efficient and stable solid oxide cells, Adv. Sci. 12 (2025) 2409272, https://doi.org/10.1002/advs.202409272.
[83] W. Fan, Z. Sun, Y. Bai, Manipulating electrocatalytic activity of perovskite oxide through electrochemical treatment, Small. 18 (2022) 2107131, https://doi.org/10.1002/smll.202107131.
[84] D. Jennings, M.L. Weber, A. Meise, T. Binninger, C.J. Price, M. Kindelmann, I. Reimanis, H. Matsumoto, P. Cao, R. Dittmann, P.M. Kowalski, M. Heggen, O. Guillon, J. Mayer, F. Gunkel, W. Rheinheimer, Direct atomic-scale investigation of the coarsening mechanisms of exsolved catalytic Ni nanoparticles, Nat. Commun. 16 (2025) 6830, https://doi.org/10.1038/s41467-025-61971-z.
[85] K.G. Both, D. Neagu, Ø. Prytz, T. Norby, A. Chatzitakis, Exsolution of Ni nanoparticles in A-site excess STO films, Nanoscale Adv. 6 (2024) 6336–6343, https://doi.org/10.1039/d4na00213j.
[86] A.U. Haq, F. Fanelli, L. Bekris, A.M. Martin, S. Lee, H. Khalid, C.D. Savaniu, K. Kousi, I.S. Metcalfe, J.T.S. Irvine, P. Maguire, E.I. Papaioannou, D. Mariotti, Dielectric barrier plasma discharge exsolution of nanoparticles at room temperature and atmospheric pressure, Adv. Sci. 11 (2024) 2402235, https://doi.org/10.1002/advs.202402235.
[87] A. López-García, S. Remiro-Buenamañana, D. Neagu, A.J. Carrillo, J.M. Serra, Squeezing out nanoparticles from perovskites: Controlling exsolution with pressure, Small. 20 (2024) 2403544, https://doi.org/10.1002/smll.202403544.
[88] Z. Xie, Q. Yang, X. Xu, D. He, Y. Yi, H. Qiu, H. Shi, Y. Pang, W. Wang, C. Su, In situ exsolution-induced formation of amorphous/crystalline heterointerfaces in $Ba_{0.6}Sr_{0.4}Co_{0.8}Fe_{0.2}O_{3-\delta}$ for enhanced oxygen electrocatalysis in zinc−air batteries, Int. J. Hydrogen. Energy 127 (2025) 530–540, https://doi.org/10.1016/j.ijhydene.2025.04.049.
[89] K. Park, M. Saqib, H. Lee, D. Shin, M. Jo, K.M. Park, M. Hamayun, S.H. Kim, S. Kim, K.-S. Lee, R. O'Hayre, M. Choi, S.-J. Song, J.-Y. Park, Water-mediated exsolution of nanoparticles in alkali metal-doped perovskite structured triple-conducting oxygen electrocatalysts for reversible cells, Energy Environ. Sci. 17 (2024) 1175–1188, https://doi.org/10.1039/d3ee03510g.
[90] S. Chattopadhyay, A.B. Naden, W.S.J. Skinner, G. Kerherve, D.J. Payne, J.T. S. Irvine, Room temperature exsolution of CdS nanodots on A-site deficient cotton-ball like titanate perovskite nanoparticles for H_2 production under visible light, Adv. Energy Mater. 13 (2023) 2301381, https://doi.org/10.1002/aenm.202301381.
[91] R. Zhang, H. Ma, S. Han, Z. Wu, X. Zhou, Z. Chen, J. Liu, Y. Xiao, W. Chen, K. P. Loh, Dynamically stable $Cu^0Cu^{\delta+}$ pair sites based on in situ-exsolved Cu nanoclusters on $CaCO_3$ for efficient CO_2 electroreduction, Angew. Chem., Int. Ed. 64 (2025) e202421860, https://doi.org/10.1002/anie.202421860.
[92] M. Wang, B. Zhang, J. Ding, F. Zhang, R. Tu, M.T. Bernards, Y. He, P. Xie, Y. Shi, A robust approach to in situ exsolve highly dispersed and stable electrocatalysts, Small. 18 (2022) 2105741, https://doi.org/10.1002/smll.202105741.
[93] J. Kim, S. Gunduz, A.C. Co, U.S. Ozkan, Electrochemical exsolution of metal nanoparticles from perovskite oxide upon electrolysis, Appl. Catal. B-Environ. 344 (2024) 123603, https://doi.org/10.1016/j.apcatb.2023.123603.
[94] H. Lv, L. Lin, X. Zhang, Y. Song, H. Matsumoto, C. Zeng, N. Ta, W. Liu, D. Gao, G. Wang, X. Bao, In situ investigation of reversible exsolution/dissolution of CoFe alloy nanoparticles in a Co-doped $Sr_2Fe_{1.5}Mo_{0.5}O_{6-\delta}$ cathode for CO_2 electrolysis, Adv. Mater. 32 (2020) 1906193, https://doi.org/10.1002/adma.201906193.
[95] W. Fan, B. Wang, R. Gao, G. Dimitrakopoulos, J. Wang, X. Xiao, L. Ma, K. Wu, B. Yildiz, J. Li, Anodic shock-triggered exsolution of metal nanoparticles from perovskite oxide, J. Am. Chem. Soc. 144 (2022) 7657–7666, https://doi.org/10.1021/jacs.1c12970.
[96] D. Zhang, Y. Luo, T. Liu, N. Yu, Y. Wang, M. Ding, Potential reduction-induced fast exsolution of hyperfine nanoparticles afford highly active CO_2 reduction reaction, Appl. Catal. B-Environ. 382 (2026) 125937, https://doi.org/10.1016/j.apcatb.2025.125937.
[97] S.-M. Jung, Y. Kim, D.-H. Yang, Y. Kim, K.-S. Kim, G. Choe, J. Lee, K. Ihm, S.-Y. Choi, J. Son, Y.-T. Kim, Low-temperature exsolution of cobalt from perovskite nanoparticles via bead milling for enhanced electrocatalytic oxygen evolution reaction, Adv. Funct. Mater. 35 (2025) 2506227, https://doi.org/10.1002/adfm.202506227.
[98] M.L. Weber, D. Jennings, S. Fearn, A. Cavallaro, M. Prochazka, A. Gutsche, L. Heymann, J. Guo, L. Yasin, S.J. Cooper, J. Mayer, W. Rheinheimer, R. Dittmann, R. Waser, O. Guillon, C. Lenser, S.J. Skinner, A. Aguadero, S. Nemšák, F. Gunkel, Thermal stability and coalescence dynamics of exsolved metal nanoparticles at charged perovskite surfaces, Nat. Commun. 15 (2024) 9724, https://doi.org/10.1038/s41467-024-54008-4.
[99] D. Neagu, V. Kyriakou, I.-L. Roiban, M. Aouine, C. Tang, A. Caravaca, K. Kousi, I. Schreur-Piet, I.S. Metcalfe, P. Vernoux, M.C.M.V.D. Sanden, M.N. Tsampas, In situ observation of nanoparticle exsolution from perovskite oxides: From atomic scale mechanistic insight to nanostructure tailoring, ACS. Nano 13 (2019) 12996–13005, https://doi.org/10.1021/acsnano.9b05652.
[100] J.T. Mefford, X. Rong, A.M. Abakumov, W.G. Hardin, S. Dai, A.M. Kolpak, K. P. Johnston, K.J. Stevenson, Water electrolysis on $La_{1-x}Sr_xCoO_{3-\delta}$ perovskite electrocatalysts, Nat. Commun. 7 (2016) 11053, https://doi.org/10.1038/ncomms11053.
[101] M.A. Qadeer, X. Zhang, M.A. Farid, M. Tanveer, Y. Yan, S. Du, Z.-F. Huang, M. Tahir, J.-J. Zou, A review on fundamentals for designing hydrogen evolution electrocatalyst, J. Power. Sources. 613 (2024) 234856, https://doi.org/10.1016/j.jpowsour.2024.234856.
[102] R.-J. Li, W.-J. Niu, W.-W. Zhao, B.-X. Yu, C.-Y. Cai, L.-Y. Xu, F.-M. Wang, Achievements and challenges in surfactants-assisted synthesis of MOFs-derived transition metal−nitrogen−carbon as a highly efficient electrocatalyst for ORR, OER, and HER, Small. 21 (2025) 2408227, https://doi.org/10.1002/smll.202408227.
[103] Y. Zhu, J. Dai, W. Zhou, Y. Zhong, H. Wang, Z. Shao, Synergistically enhanced hydrogen evolution electrocatalysis by in situ exsolution of metallic nanoparticles on perovskites, J. Mater. Chem. A 6 (2018) 13582–13587, https://doi.org/10.1039/c8ta02347f.
[104] K. Huang, An emerging platform for electrocatalysis: Perovskite exsolution, Sci. Bull. 61 (2016) 1783–1784, https://doi.org/10.1007/s11434-016-1194-8.
[105] J. Bai, J. Shang, J. Mei, D. Qi, T. Liao, Z. Sun, Triphenylphosphine-assisted exsolution engineering on Ruddlesden−Popper perovskites for promoting oxygen evolution, Energy Environ. Mater. 7 (2024) e12668, https://doi.org/10.1002/eem2.12668.
[106] S. Zuo, C. Wang, Z. Xia, J. Ding, A.B. Naden, J.T.S. Irvine, Combined exsolution and electrodeposition strategy for enhancing electrocatalytic activity of Ti-based perovskite oxides in oxygen and hydrogen evolution reactions, Adv. Sci. 12 (2025) 2410535, https://doi.org/10.1002/advs.202410535.
[107] F.L. Buchauer, S. Kim, S.B. Simonsen, R. Lee, W. Jung, C, Chatzichristodoulou, Stability and exsolution of $Sr_{0.98}Ti_{0.7}Fe_{0.25}Ni_{0.05}O_3$ for the oxygen evolution reaction in an alkaline environment, J. Am. Chem. Soc. 147 (2025) 26402–26413, https://doi.org/10.1021/jacs.5c05748.
[108] T. Chen, S. Sun, Y. He, H. Leng, C. Sun, C. Wu, In situ exsolution of ternary alloy nanoparticles from perovskite oxides to realize enhanced oxygen evolution reactivity, J. Alloys. Compd. 960 (2023) 170974, https://doi.org/10.1016/j.jallcom.2023.170974.
[109] J. Kim, H. Kim, J.-W. Son, Y.-B. Kim, S. Yang, H.-I. Ji, Strain-regulated exsolution of Ru on hydrogen-storing oxide for ambient ammonia catalysis, J. Mater. Chem. A 13 (2025) 41885–41895, https://doi.org/10.1039/d5ta06310h.
[110] J. Xia, W. Lin, W. Gong, C. Jian, K. Sasaki, Y. Choi, Y. Chen, Exsolution of NiCo alloys over Ruddlesden-Popper perovskite for mild electrochemical synthesis of ammonia on protonic ceramic electrochemical cells, Appl. Catal. B-Environ. 383 (2026) 126038, https://doi.org/10.1016/j.apcatb.2025.126038.
[111] Y. Xiong, Y. Wang, J. Zhou, F. Liu, F. Hao, Z. Fan, Electrochemical nitrate reduction: Ammonia synthesis and the beyond, Adv. Mater. 36 (2024) 2304021, https://doi.org/10.1002/adma.202304021.
[112] M. Zuo, Y. Kong, H. Zhou, Y. Chen, Y. Sun, S. Li, L. Han, In situ exsolution to form Cu nanoparticles on Cu-doped $LaFeO_3$ perovskite oxides for efficient electrocatalytic reduction of nitrate to ammonia, Adv. Funct. Mater. (2025) e13364, https://doi.org/10.1002/adfm.202513364.
[113] Y. Luo, X. Wang, F. Gao, L. Jiang, D. Wang, H. Pan, From single atom photocatalysts to synergistic photocatalysts: Design principles and applications, Adv. Funct. Mater. 35 (2025) 2418427, https://doi.org/10.1002/adfm.202418427.
[114] L. Zhang, Y. Yang, Z. Zhou, J. Li, G. Chen, L. Zhou, Y. Qiu, Y. Sun, Redispersion of exsolved Cu nanoparticles on $LaFeO_3$ photocatalyst for tunable photocatalytic CO_2 reduction, Chem. Eng. J. 452 (2023) 139273, https://doi.org/10.1016/j.cej.2022.139273.
[115] Q. Li, J. Zhou, L. Fu, C. Chen, S. Mao, Z. Pu, J. Yang, J.-W. Shi, K. Wu, Fabrication of heterostructural Ru−$SrTiO_3$ fibers through in-situ exsolution for visible-light-

induced photocatalysis, J. Alloys. Compd. 925 (2022) 166747, https://doi.org/10.1016/j.jallcom.2022.166747.
[116] Z. Wu, P. Zhu, Y. Huang, J. Yao, F. Yang, Z. Zhang, M. Ni, A Comprehensive review of modeling of solid oxide fuel cells: From large systems to fine electrodes, Chem. Rev. 125 (2025) 2184–2268, https://doi.org/10.1021/acs.chemrev.4c00614.
[117] R.M. Ormerod, Solid oxide fuel cells, Chem. Soc. Rev. 32 (2003) 17–28, https://doi.org/10.1039/b105764m.
[118] A.N. Zainon, M.R. Somalu, A.M.K. Bahrain, A. Muchtar, N.A. Baharuddin, M. A. Muhammed, N. Osman, A. Abdul Samat, A.K. Azad, N.P. Brandon, Challenges in using perovskite-based anode materials for solid oxide fuel cells with various fuels: A review, Int. J. Hydrogen. Energy 48 (2023) 20441–20464, https://doi.org/10.1016/j.ijhydene.2022.12.192.
[119] H. Hu, M. Li, H. Min, X. Zhou, J. Li, X. Wang, Y. Lu, X. Ding, Enhancing the catalytic activity and coking tolerance of the perovskite anode for solid oxide fuel cells through in situ exsolution of Co−Fe nanoparticles, ACS. Catal. 12 (2022) 828–836, https://doi.org/10.1021/acscatal.1c04807.
[120] B. Huang, S.R. Wang, R.Z. Liu, T.L. Wen, Preparation and performance characterization of the Fe−Ni/ScSZ cermet anode for oxidation of ethanol fuel in SOFCs, J. Power. Sources. 167 (2007) 288–294, https://doi.org/10.1016/j.jpowsour.2007.02.075.
[121] D.-M. Amaya-Dueñas, G. Chen, A. Weidenkaff, N. Sata, F. Han, I. Biswas, R. Costa, K.A. Friedrich, A-site deficient chromite with in situ Ni exsolution as a fuel electrode for solid oxide cells (SOCs), J. Mater. Chem. A 9 (2021) 5685–5701, https://doi.org/10.1039/d0ta07090d.
[122] M. Xu, R. Cao, S. Wu, J. Lee, D. Chen, J.T.S. Irvine, Nanoparticle exsolution via electrochemical switching in perovskite fibers for solid oxide fuel cell electrodes, J. Mater. Chem. A 11 (2023) 13007–13015, https://doi.org/10.1039/d3ta00535f.
[123] F.-Z. Han, Z.-X. Wang, S.-L. Zhang, C.-X. Li, S.A. Barnett, Highly efficient perovskite-based fuel electrodes for solid oxide electrochemical cells via in-situ nanoparticle exsolution and electron conduction enhancement, Appl. Catal. B-Environ. 361 (2025) 124676, https://doi.org/10.1016/j.apcatb.2024.124676.
[124] D. Zhang, Y. Wang, Y. Peng, Y. Luo, T. Liu, W. He, F. Chen, M. Ding, Novel high-entropy perovskite-type symmetrical electrode for efficient and durable carbon dioxide reduction reaction, Adv. Powder. Mater. 2 (2023) 100129, https://doi.org/10.1016/j.apmate.2023.100129.
[125] A. Kwade, W. Haselrieder, R. Leithoff, A. Modlinger, F. Dietrich, K. Droeder, Current status and challenges for automotive battery production technologies, Nat. Energy 3 (2018) 290–300, https://doi.org/10.1038/s41560-018-0130-3.
[126] P.K. Nayak, L. Yang, W. Brehm, P. Adelhelm, From lithium-ion to sodium-ion batteries: Advantages, challenges, and surprises, Angew. Chem., Int. Ed. 57 (2018) 102–120, https://doi.org/10.1002/anie.201703772.
[127] S.H. Choi, C.H. Baek, J. Oh, G.-J. Lee, M. Kim, H. Lee, D.-J. Yoo, Y.S. Jung, K. S. Kim, J.-S. Yu, W. Cho, H. Park, J.W. Choi, Silver exsolution from Li-argyrodite electrolytes for initially anode-free all-solid-state batteries, Nat. Commun. 16 (2025) 5871, https://doi.org/10.1038/s41467-025-61074-9.
[128] H. Hou, M. Han, B. Wang, Y. Cong, K. Huang, X. Hou, Y. Zhang, B. Zheng, S. Feng, A-site defect engineering regulates bimetallic exsolution in perovskite oxide boosting the performance of Li−O_2 batteries, Adv. Energy Mater. 15 (2025) 2402925, https://doi.org/10.1002/aenm.202402925.
[129] S. Sharma, S. Bhattacharyya, R. Thirupathi, R.P. Srivastava, S.K. Jha, S. Omar, Iron phosphide exsolution for enhanced electrochemical performance of Fe-doped $Na_3V_2(PO_4)_3$ cathodes in sodium-ion batteries, ACS. Appl. Energy Mater. 8 (2025) 10984–10998, https://doi.org/10.1021/acsaem.5c01091.
[130] X. Ren, D. Yu, L. Yuan, Y. Bai, K. Huang, J. Liu, S. Feng, In situ exsolution of Ag from $AgBiS_2$ nanocrystal anode boosting high-performance potassium-ion batteries, J. Mater. Chem. A 8 (2020) 15058–15065, https://doi.org/10.1039/d0ta03964k.
[131] A. Khan, M. Orbay, N. Dupré, E. Gautron, E.L Calvez, O. Crosnier, A. Balducci, T. Brousse, Lithium storage behaviour of $AgNbO_3$ perovskite: Understanding electrochemical activation and charge storage mechanisms, Energy Storage Mater. 70 (2024) 103431, https://doi.org/10.1016/j.ensm.2024.103431.
[132] D. Bresser, S. Passerini, B. Scrosati, Recent progress and remaining challenges in sulfur-based lithium secondary batteries - a review, Chem. Commun. 49 (2013) 10545–10562, https://doi.org/10.1039/c3cc46131a.
[133] W. Hou, Y. Yang, L. Fang, Y. Mao, W. Sun, Y. Bai, K. Sun, Z. Wang, Perovskite with in situ exsolved cobalt nanometal heterostructures for high rate and stable lithium−sulfur batteries, Chem. Eng. J. 409 (2021) 128079, https://doi.org/10.1016/j.cej.2020.128079.
[134] E. Shin, D.-H. Kim, J.-H. Cha, S. Yun, H. Shin, J. Ahn, J.-S. Jang, J.W. Baek, C. Park, J. Ko, S. Park, S.-Y. Choi, I.-D. Kim, Ultrafast ambient-air exsolution on metal oxide via momentary photothermal effect, ACS. Nano 16 (2022) 18133–18142, https://doi.org/10.1021/acsnano.2c05128.
[135] G.S. Kim, H. Kum, J.-W. An, H. Kwon, Y.-J. Ryu, H.W. Jang, K. Lee, J. Kim, J.-S. Jang, Ultrafast photothermal-shock-driven multimetallic exsolution for artificial olfaction of sulfur compounds detection, Small. Struct. 6 (2025) 2500292, https://doi.org/10.1002/sstr.202500292.
[136] S.H. Kim, H. Jeong, B. Sharma, J.-h. Myung, In situ exsolution catalyst: An innovative approach to develop highly selective and sensitive gas sensors, ACS. Appl. Mater. Interfaces. 14 (2022) 18275–18282, https://doi.org/10.1021/acsami.1c22701.
[137] Z. Zhu, J. Zhou, Q. Li, Z. Liu, Q. Deng, Z. Zhou, C. Li, L. Fu, J. Zhou, H. Li, Q. Zhang, K. Wu, Preparation of heterostructured Cu−CeO_2/$SrTiO_3$ catalysts by rapid plasma exsolution for photothermal reverse water gas shift reaction, J. CO2. Util. 80 (2024) 102665, https://doi.org/10.1016/j.jcou.2023.102665.
[138] A.M. Martin, S. Saini, A. Salvian, T. Miah, C.Y. Chan, C.A. Rossa, S. Gadkari, K. Kousi, Exsolution of Pt nanoparticles from mixed Zr/Gd−CeO_2 oxides for microbial fuel cell-based biosensors, Small. Sci. 5 (2025) 2400619, https://doi.org/10.1002/smsc.202400619.
[139] W. Meng, S. Wu, L. Dai, Y. Li, M. Wang, L. Wang, An impedancemetric NH_3 sensor based on Ag nanoparticle decorated $NiFe_2O_4$ sensing electrode prepared by electrochemical exsolution method, Sens. Actuators. B Chem. 414 (2024) 135933, https://doi.org/10.1016/j.snb.2024.135933.
[140] H. Ma, S. Wang, Q. Ye, X. Tao, C. Li, Enhancing photothermal conversion of spinel zinc cobalt oxide through lattice distortion regulation, J. Mater. Chem. A 13 (2025) 42187–42192, https://doi.org/10.1039/d5ta07675g.
[141] Q. Li, Q. Zhang, C. Zeng, K. Xing, J. Niu, H. Wang, Z. Xue, B. Xiao, K. Wu, J. Zhou, Unveiling the roles of lattice strain by Ni exsolution on photothermal reduction of CO_2 activity in $BaTiO_3$ catalyst, Small. 21 (2025) 2409441, https://doi.org/10.1002/smll.202409441.
[142] M. Liao, W. Liu, C. Li, S. Guo, Y. Chen, C. Wang, Y. Chen, C. Wang, Y. Chen, Y. Du, Understandings in surface metal exsolution of NiFeZn ternary alloy/spinel in ethanol steam reforming: The key to hydrogen production, Chem. Eng. J. 497 (2024) 154596, https://doi.org/10.1016/j.cej.2024.154596.
[143] S. Joo, K. Kim, O. Kwon, J. Oh, H.J. Kim, L. Zhang, J. Zhou, J.-Q. Wang, H. Y. Jeong, J.W. Han, G. Kim, Enhancing thermocatalytic activities by upshifting the d-band center of exsolved Co−Ni−Fe ternary alloy nanoparticles for the dry reforming of methane, Angew. Chem., Int. Ed. 133 (2021), https://doi.org/10.1002/ange.202101335, 16048-1605.
[144] H. Kim, C. Lim, O. Kwon, J. Oh, M.T. Curnan, H.Y. Jeong, S. Choi, J.W. Han, G. Kim, Unveiling the key factor for the phase reconstruction and exsolved metallic particle distribution in perovskites, Nat. Commun. 12 (2021) 6814, https://doi.org/10.1038/s41467-021-26739-1.
[145] H. Kageyama, K. Hayashi, K. Maeda, J.P. Attfield, Z. Hiroi, J.M. Rondinelli, K. R. Poeppelmeier, Expanding frontiers in materials chemistry, physics with multiple anions, Nat. Commun. 9 (2018) 772, https://doi.org/10.1038/s41467-018-02838-4. **Provide a broad overview of multiple anion materials, emphasizing that controlled synthesis routes determine anion incorporation and local coordination environments, thereby tuning electronic properties for functional applications.**
[146] Y. Niu, S. Lin, X. Dong, M. Wang, Y. Zhang, S. Ning, Z. Li, J. Wang, J. Yin, S. Chen, P. Zhu, J. Zhu, Homogenizing strain via reinforced lattice interaction enables efficient and stable 4T perovskite/silicon tandem solar cells, Joule 9 (2025) 102142, https://doi.org/10.1016/j.joule.2025.102142.
[147] H. Han, Y. Xing, B. Park, D.I. Bazhanov, Y. Jin, J.T.S. Irvine, J. Lee, S.H. Oh, Anti-phase boundary accelerated exsolution of nanoparticles in non-stoichiometric perovskite thin films, Nat. Commun. 13 (2022) 6682, https://doi.org/10.1038/s41467-022-34289-3.
[148] J. Zamudio-García, F. Chiabrera, A. Morin-Martínez, I.E. Castelli, E.R. Losilla, D. Marrero-López, V. Esposito, Hierarchical exsolution in vertically aligned heterostructures, Nat. Commun. 15 (2024) 8961, https://doi.org/10.1038/s41467-024-53252-y.
[149] J. Wang, K.B. Woller, A. Kumar, Z. Zhang, H. Zhou, I. Waluyo, A. Hunt, J. M. LeBeau, B. Yildiz, Ion irradiation to control size, composition and dispersion of metal nanoparticle exsolution, Energy Environ. Sci. 16 (2023) 5464–5478, https://doi.org/10.1039/d3ee02448b.
[150] L. Han, J. Zhang, M. Zou, J. Tong, Toward superb perovskite oxide electrocatalysts: Engineering of coupled nanocomposites, Small. 18 (2022) 2204784, https://doi.org/10.1002/smll.202204784.
[151] Z. Li, N. Chen, J. Wang, P. Li, M. Guo, Q. Wang, C. Li, C. Wang, T. Guo, S. Chen, Efficient reduction of nitric oxide using zirconium phosphide powders synthesized by elemental combination method, Sci. Rep. 7 (2017) 13044, https://doi.org/10.1038/s41598-017-13616-5.
[152] A. Bonkowski, J.A. Kilner, R.A.D. Souza, Oxygen grain-boundary diffusion in (La, Sr)$FeO_{3-\delta}$ perovskite-oxides probed by molecular-dynamics simulations, RSC Appl. Interfaces 1 (2024) 699–710, https://doi.org/10.1039/d3lf00263b.
[153] Y. Luo, D. Zhang, T. Liu, X. Chang, J. Wang, Y. Wang, X.-K. Gu, M. Ding, In situ exsolution of quaternary alloy nanoparticles for CO_2−CO mutual conversion using reversible solid oxide cells, Adv. Funct. Mater. 34 (2024) 2403922, https://doi.org/10.1002/adfm.202403922.
[154] J.K. Kim, S. Kim, Y.B. Kim, B. Koo, D. Oh, H. Kim, K. Kim, J.W. Han, W. Jung, Designing supported nanoparticles via synergistic ex-solution and phosphorization for tailored active site generation, Adv. Mater. 37 (2025) 2417576, https://doi.org/10.1002/adma.202417576.
[155] K. Li, H. Pan, F. Wang, Z. Zhang, S. Min, In-situ exsolved NiS nanoparticle-socketed CdS with strongly coupled interfaces as a superior visible-light-driven photocatalyst for hydrogen evolution, Appl. Catal. B-Environ. 321 (2023) 122028, https://doi.org/10.1016/j.apcatb.2022.122028.
[156] S. Song, J. Sun, J. Zhou, Z. Hu, H.-J. Lin, T.-S. Chan, C.-T. Chen, N. Zhang, C. Jing, J. Hu, L. Zhang, J.-Q. Wang, Unexpected increasing Co valence state of an exsolved catalyst by Mo doping for enhanced oxygen evolution reaction, Chem. Eng. J. 425 (2021) 130681, https://doi.org/10.1016/j.cej.2021.130681.
[157] Q. Feng, P. Zhu, D. Fan, M.C. Williams, G. Huang, J. Zhao, Engineering metal-oxide interfaces via controlled exsolution in Ir-doped $Y_2Ru_2O_7$ pyrochlore for superior hydrogen evolution reaction, J. Colloid. Interface Sci. 700 (2025) 138517, https://doi.org/10.1016/j.jcis.2025.138517.
[158] H. Tao, F. Wang, Z. Zhang, S. Min, An in situ exsolved Cu-based electrocatalyst from an intermetallic Cu_5Si compound for efficient CH_4 electrosynthesis, Nanoscale 16 (2024) 3430–3437, https://doi.org/10.1039/d3nr05847f.
[159] J. Yu, X. Yang, Y. Jia, Z.-Q. Wang, W. Li, Y. Jiang, S. Dai, W. Zhan, Regulating socketed geometry of nanoparticles on perovskite oxide supports for enhanced

stability in oxidation reactions, Nat. Commun. 15 (2024) 10229, https://doi.org/10.1038/s41467-024-54546-x.
[160] P.B. Managutti, S. Tymen, X. Liu, O. Hernandez, C. Prestipino, A.L.G.L. Salle, S. Paul, L. Jalowiecki-Duhamel, V. Dorcet, A. Billard, P. Briois, M. Bahout, Exsolution of Ni nanoparticles from A-site-deficient layered double perovskites for dry reforming of methane and as an anode material for a solid oxide fuel cell, ACS. Appl. Mater. Interfaces. 13 (2021) 35719–35728, https://doi.org/10.1021/acsami.1c08158.
[161] X. Ou, Q. Liu, F. Wei, C. Sun, Y. Liao, Y. Zhou, F. Yan, Ionic liquid-assisted exsolution of high-density Cu nanoparticles on $La_{1.568}Sr_{0.392}Ce_{0.04}NiCu_xO_{4-\delta}$ as cathode for Zn−air batteries, Chem. Eng. J. 451 (2023) 139037, https://doi.org/10.1016/j.cej.2022.139037.
[162] J. Lee, J. Lee, X. Jin, H. Kim, S.-J. Hwang, Atomically-thin holey 2D nanosheets of defect-engineered MoN−Mo_5N_6 composites as effective hybridization matrices, Small. 20 (2024) 2306781, https://doi.org/10.1002/smll.202306781.
[163] S. Joo, C. Lim, O. Kwon, L. Zhang, J. Zhou, J.-Q. Wang, H.Y. Jeong, Y.-w. Sin, S. Choi, G. Kim, The first observation of Ni nanoparticle exsolution from YSZ and its application for dry reforming of methane, Mater. Rep.-Energy 1 (2021) 100021, https://doi.org/10.1016/j.matre.2021.100021.
[164] Y.H. Park, X. Jin, S.-J. Hwang, Optimization of interfacial interaction and defect structure of holey metal nitride matrices to boost supercapacitor electrode activity of metal−organic frameworks, Small. 21 (2025) e06555, https://doi.org/10.1002/smll.202506555.
[165] J. Tan, D. Lee, J. Ahn, B. Kim, J. Kim, J. Moon, Thermally driven in situ exsolution of Ni nanoparticles from (Ni,Gd)CeO_2 for high-performance solid oxide fuel cells, J. Mater. Chem. A 6 (2018) 18133–18142, https://doi.org/10.1039/c8ta05978k.
[166] X. Meng, Y. Wang, Y. Zhao, T. Zhang, N. Yu, X. Chen, M. Miao, T. Liu, In-situ exsolution of nanoparticles from Ni substituted $Sr_2Fe_{1.5}Mo_{0.5}O_6$ perovskite oxides with different Ni doping contents, Electrochim. Acta 348 (2020) 136351, https://doi.org/10.1016/j.electacta.2020.136351.
[167] X. Cao, L. Ke, K. Zhao, X. Yan, X. Wu, N. Yan, Surface decomposition of doped $PrBaMn_2O_{5+\delta}$ induced by in situ nanoparticle exsolution: Quantitative characterization and catalytic effect in methane dry reforming reaction, Chem. Mater. 34 (2022) 10484–10494, https://doi.org/10.1021/acs.chemmater.2c02488.
[168] J. Zhou, Z. Zhu, Q. Li, Q. Zhang, Z. Liu, Q. Deng, Z. Zhou, C. Li, L. Fu, J. Zhou, H. Li, K. Wu, Fabrication of heterostructural $FeNi_3$-loaded perovskite catalysts by rapid plasma for highly efficient photothermal reverse water gas shift reaction, Small. 20 (2024) 2307302, https://doi.org/10.1002/smll.202307302.
[169] X. Guo, L. Yao, X. Hou, X. Wu, Y. Zhang, Q. Zhu, Z. Guo, S. Li, Y. Jiang, S. Feng, K. Huang, An exsolution constructed FeNi/$NiFe_2O_4$ composite: preferential breaking of octahedral metal-oxygen bonds in a spinel oxide, Chem. Sci. 13 (2022) 9440–9449, https://doi.org/10.1039/d2sc02149h.
[170] G. Han, M. Zhuansun, T. Wang, Y. Wang, B-site-metal exsolution on perovskite oxides activates alkaline water oxidation via the lattice oxygen mechanism, Adv. Mater. Interfaces. 11 (2024) 2300760, https://doi.org/10.1002/admi.202300760.
[171] Z. Wang, T. Tan, K. Du, Q. Zhang, M. Liu, C. Yang, A high-entropy layered perovskite coated with in situ exsolved core-shell CuFe@FeO_x nanoparticles for efficient CO_2 electrolysis, Adv. Mater. 36 (2024) 2312119, https://doi.org/10.1002/adma.202312119.
[172] Y. Yang, Z. Ding, H. Wang, J. Li, Y. Zheng, H. Guo, L. Zhang, B. Yang, Q. Gu, H. Xiong, Y. Sun, Dynamic tracking of exsolved PdPt alloy/perovskite catalyst for efficient lean methane oxidation, Chin. Chem. Lett. 35 (2024) 108585, https://doi.org/10.1016/j.cclet.2023.108585.
[173] T. Kim, M.J. Kang, N.H. Kwon, Y.C. Hong, X. Jin, M. Kim, S.-J. Hwang, Hybridization-driven introduction of anion vacancies to boost the photocatalytic nitrogen fixation functionality of low-lattice-energy nanosheets, ACS. Nano 19 (2025) 29798–29812, https://doi.org/10.1021/acsnano.5c11160.
[174] X. Wang, Q. Yang, X. Li, Z. Li, C. Gao, H. Zhang, X. Chu, C. Redshaw, S. Shi, Y. A. Wu, Y. Ma, Y. Peng, J. Li, S. Feng, Exploring the dynamic evolution of lattice oxygen on exsolved-Mn_2O_3@$SmMn_2O_5$ interfaces for NO Oxidation, Nat. Commun. 15 (2024) 7613, https://doi.org/10.1038/s41467-024-51473-9.
[175] H.K. Kim, H. Jang, X. Jin, M.G. Kim, S.-J. Hwang, A crucial role of enhanced Volmer−Tafel mechanism in improving the electrocatalytic activity via synergetic optimization of host, interlayer, and surface features of 2D nanosheets, Appl. Catal. B-Environ. 312 (2022) 121391, https://doi.org/10.1016/j.apcatb.2022.121391.
[176] Y. Sun, J. Lee, N.H. Kwon, J. Lim, X. Jin, Y. Gogotsi, S.-J. Hwang, Enhancing hydrogen evolution reaction activity of palladium catalyst by immobilization on MXene nanosheets, ACS. Nano 18 (2024) 6243–6255, https://doi.org/10.1021/acsnano.3c09640.
[177] H. Lv, T. Liu, X. Zhang, Y. Song, H. Matsumoto, N. Ta, C. Zeng, G. Wang, X. Bao, Atomic-scale insight into exsolution of CoFe alloy nanoparticles in $La_{0.4}Sr_{0.6}Co_{0.2}Fe_{0.7}Mo_{0.1}O_{3-\delta}$ with efficient CO_2 electrolysis, Angew. Chem., Int. Ed. 59 (2020) 15968–15973, https://doi.org/10.1002/anie.202006536.
[178] P. Cao, P. Tang, M.F. Bekheet, H. Du, L. Yang, L. Haug, A. Gili, B. Bischoff, A. Gurlo, M. Kunz, R.E. Dunin-Borkowski, S. Penner, M. Heggen, Atomic-scale insights into nickel exsolution on $LaNiO_3$ catalysts via in situ electron microscopy, J. Phys. Chem. C 126 (2022) 786–796, https://doi.org/10.1021/acs.jpcc.1c09257.
[179] Y.-F. Sun, Y.-Q. Zhang, J. Chen, J.-H. Li, Y.-T. Zhu, Y.-M. Zeng, B.S. Amirkhiz, J. Li, B. Hua, J.-L. Luo, New opportunity for in situ exsolution of metallic nanoparticles on perovskite parent, Nano Lett. 16 (2016) 5303–5309, https://doi.org/10.1021/acs.nanolett.6b02757.
[180] A. López-García, A.J. Carrillo, C.E. Jiménez, R.S. Anzorena, R. Garcia-Diez, V. Pérez-Dieste, I.J. Villar-Garcia, A.B. Hungría, M. Bär, J.M. Serra, Understanding the evolution of ternary alloyed nanoparticles during reversible exsolution from double perovskite oxides, J. Mater. Chem. A 12 (2024) 22609–22626, https://doi.org/10.1039/D4TA03146F.
[181] D. Yang, W. Ming, H. Shi, L. Zhang, M.-H. Du, Fast diffusion of native defects and impurities in perovskite solar cell material $CH_3NH_3PbI_3$, Chem. Mater. 28 (2016) 4349–4357, https://doi.org/10.1021/acs.chemmater.6b01348.
[182] I. Hamada, A. Uozumi, Y. Morikawa, A. Yanase, H. Katauama-Yoshida, A density functional theory study of self-regenerating catalysts $LaFe_{1-x}M_xO_{3-y}$ (M = Pd , Rh, Pt), J. Am. Chem. Soc. 133 (2011) 18506–18509, https://doi.org/10.1021/ja110302t.
[183] D. Neagu, J.T.S. Irvine, J. Wang, B. Yildiz, A.K. Opitz, J. Fleig, Y. Wang, J. Liu, L. Shen, F. Ciucci, B.A. Rosen, Y. Xiao, K. Xie, G. Yang, Z. Shao, Y. Zhang, J. Reinke, T.A. Schmauss, S.A. Barnett, R. Maring, V. Kyriakou, U. Mushtaq, M. N. Tsampas, Y. Kim, R. O'Hayre, A.J. Carrillo, T. Ruh, L. Lindenthal, F. Schrenk, C. Rameshan, E.I. Papaioannou, K. Kousi, I.S. Metcalfe, X. Xu, G. Liu, Roadmap on exsolution for energy applications, J. Phys-Energy 5 (2023) 031501, https://doi.org/10.1088/2515-7655/acd146.
[184] J. Wang, J. Yang, J.L. Wardini, I. Waluyo, A. Hunt, E.J. Crumlin, N. Fairley, W. J. Bowman, H.Y. Hwang, B. Yildiz, Fermi level equilibration and charge transfer at the exsolved metal-oxide interface, J. Am. Chem. Soc. 147 (2025) 2991–2997, https://doi.org/10.1021/jacs.4c14695.
[185] H. Lv, L. Lin, X. Zhang, R. Li, Y. Song, H. Matsumoto, N. Ta, C. Zeng, Q. Fu, G. Wang, X. Bao, Promoting exsolution of RuFe alloy nanoparticles on $Sr_2Fe_{1.4}Ru_{0.1}Mo_{0.5}O_{6-\delta}$ via repeated redox manipulations for CO_2 electrolysis, Nat. Commun. 12 (2021) 5665, https://doi.org/10.1038/s41467-021-26001-8.
[186] P. Kumar, D.S. Monder, CO_2 activation and dissociation on exsolved Ni/La_2O_3 catalysts: A first-principles study, J. Phys. Chem. C 128 (2024) 15451–15463, https://doi.org/10.1021/acs.jpcc.4c04270.
[187] G. Jiang, F. Yan, S. Wan, Y. Zhang, M. Yan, Microstructure evolution and kinetics of B-site nanoparticle exsolution from an A-site-deficient perovskite surface: A phase-field modeling and simulation study, Phys. Chem. Chem. Phys. 21 (2019) 10902–10907, https://doi.org/10.1039/c8cp07883a.
[188] Y. Yang, J. Li, Y. Sun, The metal/oxide heterointerface delivered by solid-based exsolution strategy: A review, Chem. Eng. J. 440 (2022) 135868, https://doi.org/10.1016/j.cej.2022.135868.
[189] M.-J. Kim, C. Lee, Y.-R. Jo, W.-G. Jung, J.-S. Ha, J.H. Shim, J.-H. Park, S.-W. Ryu, B.-J. Kim, Amorphous exsolution of Fe_3O_4 nanoparticles in $SrTiO_3$: A path to high activity and stability in photoelectrochemical water-splitting, Small. Struct. 6 (2025) 2400450, https://doi.org/10.1002/sstr.202400450.
[190] M.L. Weber, M. Wilhelm, L. Jin, U. Breuer, R. Dittmann, R. Waser, O. Guillon, C. Lenser, F. Gunkel, Exsolution of embedded nanoparticles in defect engineered perovskite layers, ACS. Nano 15 (2021) 4546–4560, https://doi.org/10.1021/acsnano.0c08657.
[191] X. Zeng, T. Nie, C. Zhao, Y. Gao, X. Liu, In situ exsolution-prepared solid-solution-type sulfides with intracrystal polarization for efficient and selective absorption of low-frequency electromagnetic wave, Adv. Sci. 11 (2024) 2403723, https://doi.org/10.1002/advs.202403723.
[192] Q.A. Islam, S. Paydar, N. Akbar, B. Zhu, Y. Wu, Nanoparticle exsolution in perovskite oxide and its sustainable electrochemical energy systems, J. Power. Sources. 492 (2021) 229626, https://doi.org/10.1016/j.jpowsour.2021.229626.
[193] K. Zhu, L. Zhang, N. Shi, B. Qiu, X. Hu, D. Huan, C. Xia, R. Peng, Y. Lu, A superior catalytic air electrode with temperature-induced exsolution toward protonic ceramic cells, ACS. Nano 18 (2024) 5141–5151, https://doi.org/10.1021/acsnano.3c12609.
[194] M. Xu, Y. Jeon, A. Naden, H. Kim, G. Kerherve, D.J. Payne, Y.-g. Shul, J.T. S. Irvine, Synergistic growth of nickel and platinum nanoparticles via exsolution and surface reaction, Nat. Commun. 15 (2024) 4007, https://doi.org/10.1038/s41467-024-48455-2.
[195] Y. Luo, X. Chang, J. Wang, D. Zhang, L. Fu, X.-K. Gu, Y. Wang, T. Liu, M. Ding, Precise regulation of in situ exsolution components of nanoparticles for constructing active interfaces toward carbon dioxide reduction, ACS. Nano 19 (2025) 1463–1477, https://doi.org/10.1021/acsnano.4c14279.
[196] M.-J. Kim, M.A. Hassan, C. Lee, W.-G. Jung, H. Bae, S. Jeon, W. Jung, J.-S. Ha, J. H. Shim, J.-H. Park, S.-W. Ryu, B.-J. Kim, Maximizing photoelectrochemical performance in metal-oxide hybrid composites via amorphous exsolution - A new exsolution mechanism for heterogeneous catalysis, Small. 20 (2024) 2308934, https://doi.org/10.1002/smll.202308934.



Taehoon Kim is currently a Ph.D. student in the Department of Materials Science and Engineering at Yonsei University (Republic of Korea), under the supervision of Prof. Seong-Ju Hwang. He received his B.S. degree in Materials Science and Engineering from Yonsei University in 2021. His research focuses on the synthesis and characterization of low-dimensional materials and their nanohybrids, as well as their applications in electrocatalysis and photocatalysis.



Yeon Hu Park is currently a Ph.D. student in the Department of Materials Science and Engineering at Yonsei University (Republic of Korea), under the supervision of Prof. Seong-Ju Hwang. He received a B.S. degree in Plant & Environmental New Resources from Kyunghee University (2021). His research focuses on synthesis and characterization of low-dimensional materials and their application in electrocatalysis and energy storage.



Jinyoung Lee is currently a Ph.D. student in the Department of Materials Science and Engineering at Yonsei University (Republic of Korea), under the supervision of Prof. Seong-Ju Hwang. He received his B.S. degree in Materials Science and Engineering from Yonsei University in 2024. His research focuses on the synthesis and characterization of low-dimensional materials and their nanohybrids, as well as their applications in lithium-ion battery electrodes.



Ajayan Vinu is currently a Laureate Professor and Director of Global Innovative Center for Advanced Nanomaterials at the University of Newcastle. He worked as a Full Professor of Nanomaterials in University of South Australia (2015-2017) and a Full Professor and ARC Future Fellow at the University of Queensland (2011-2015). He has made a significant contribution in the field of nanoporous materials with different functional elements and their application in sensing, energy storage, fuel cells, adsorption and separation, and catalysis.



Seong-Ju Hwang is currently a Underwood distinguished professor in the Department of Materials Science and Engineering at Yonsei University (Republic of Korea). He received a B.S. degree in chemistry (1992) and a M.S. degree in inorganic chemistry (1994) from Seoul National University (Republic of Korea), a Ph.D. degree in inorganic chemistry from Université Bordeaux I (France) in 2001. He worked as a full professor in the Department of Chemistry and Nanoscience at Ewha Womans University from 2005 to 2019. His research focuses on the synthesis and characterization of low-dimensional nanostructured transition metal compounds applicable for energy production, energy storage, and environmental purification.